# Electronic correlations in crystalline materials: itinerant metals and localized magnets

Leonid Pourovskii

**UNIVERSITÉ PARIS SUD, ORSAY**

# ELECTRONIC CORRELATIONS IN CRYSTALLINE MATERIALS: ITINERANT METALS AND LOCALIZED MAGNETS

Manuscrit présenté pour obtenir le diplôme de

# HABILITATION A DIRIGER LES RECHERCHES

DE L'UNIVERSITÉ PARIS-SUD

**SPÉCIALITÉ: PHYSIQUE**

par

Leonid Pourovskii

Ingénieur de recherche à l'Ecole Polytechnique

**Soutenue le 16 novembre 2018 devant le jury composé de :**

M. Dominique Givord, Institut Néel Grenoble, Rapporteur
M. Jan Kuneš, Technische Universität Wien, Rapporteur
M. Giorgio Sangiovanni, Universität Würzburg, Rapporteur
Mme. Silke Biermann, Ecole Polytechnique Palaiseau, Examinateur
M. Marc Gabay, Université Paris-Sud, Examinateur
M. Marcelo Rozenberg, Université Paris-Sud, Examinateur
M. Mark van Schilfgaarde, King's College London, Examinateur

# Contents

Chapter 1

# Overview

The Coulomb interaction between electrons in conjunction with the quantum-mechanical nature of these elementary particles gives rise to fascinating phenomena observed in crystalline materials, such as the unconventional high-$T_c$ superconductivity, Mott metal-insulator transition, heavy-fermion behavior, and colossal magnetoresistance. In order to understand their origin the so-called "correlation effects", i. e. the interplay of electronic movement and the local Coulomb repulsion in solids, had been studied for many years in the framework of simplified models like the Anderson and Hubbard model. Meanwhile, a quantitative description of weakly-interacting itinerant electronic states in simple and many transition metals as well as in band insulators, had been achieved by *ab initio* methods based on the density-functional theory (DFT) that fully take into account the complex ionic potential and multiband hopping. However, many-electron effects within DFT are treated by highly simplified static approximations employing an auxiliary independent-particle framework.

During the last twenty something years a synergy between those two efforts has led to a breakthrough in quantitative first-principles modeling of real *correlated materials*. This framework [Anisimov *et al.*, 1997b, Lichtenstein and Katsnelson, 1998] combines the standard DFT treatment for itinerant states with a much more precise and fully dynamical approach to single-site correlations on localized, typically $f$ or $d$, ionic shells. It has been successfully applied to well-known prototypical examples of the strongly-correlated behavior, like the $\alpha$-$\gamma$ transition in Ce [Held *et al.*, 2001b, Amadon *et al.*, 2006], the $\alpha$-$\delta$ transition in Pu [Savrasov *et al.*, 2001, Shim *et al.*, 2007], spectral properties of transition-metal oxides [Held *et al.*, 2001a, Pavarini *et al.*, 2004, Biermann *et al.*, 2005], the heavy-fermion state in Ce intermetallics [Shim *et al.*, 2007, Pourovskii *et al.*, 2014a] or the bad-metal behavior in iron pnictides and 4$d$ "Hund's metals" [Haule and Kotliar, 2009, Hansmann *et al.*, 2010, Mravlje *et al.*, 2011, de' Medici *et al.*, 2011], to name just a few. However, electronic correlations substantially impact the behavior of a much wider range of crystalline materials of fundamental and technological interest. A dynamical treatment of correlation effects in such materials resolves long-standing puzzles and provide a consistent picture of spectral, magnetic, thermodynamic and transport properties within the same framework.

This review focuses on two classes of materials representing, in a sense, two opposite limits

for many-electron effects in real solids: on the one hand, an itinerant transition metal, iron, on the verge of non-Fermi-liquid behavior; on the other hand, local-moment systems with their atomic-like $3d$ and $4f$ shells. Both cases can be partially treated within the standard DFT framework supplemented in the case of local-moment compounds with a static Hartree-Fock correction for the on-site Coulomb repulsion. However, in this review we will try to demonstrate that a much more consistent and refined theoretical description is achieved by taking into account the dynamics of local many-electron effects.

The review begins with the methodological Chapter 2 outlining main features of the employed *ab initio* approach (a more throughout presentation to be found in several reviews, [Kotliar *et al.*, 2006, Georges, 2004, Held, 2007]). It is based on supplementing the one-particle description of DFT with a screened on-site Coulomb repulsion between localized $d$ and $f$ states; the resulting many-electron lattice problem is then solved using the single-site dynamical mean-field theory (DMFT) [Metzner and Vollhardt, 1989, Georges and Kotliar, 1992, Georges *et al.*, 1996].

Chapter 3 reviews the role of many-body effects in the electronic structure and physical properties of iron under applied pressure and at high temperatures. Significant electronic correlations arise in this transition metal in spite of a relatively large width of its $3d$ band and result in a rich pressure-temperature phase diagram. In particular, Chapter 3 discusses the impact of correlations on the pressure-stabilized hexagonal $\varepsilon$ phase as well as on various iron phases at the extreme pressure and temperature of the solid inner core of Earth.

Strongly-localized $4f$ states of lanthanide ions can be rather successfully described within the *ab initio* DMFT framework using a simple quasi-atomic approximation for electronic correlations, which is the first subject of Chapter 4. It focuses, in particular, on technologically-important hard-magnetic rare-earth based intermetallics, where the crystal-field splitting of $4f$ shells determines the single-ion magnetic anisotropy of lanthanide ions, as well as on the impact of crystal-field effects on the electronic structure of rare-earth semimetals. In the same Chapter we also present a linear response theory, which is based on the same quasi-atomic approximation, for evaluating complex spin, orbital and multipolar inter-site exchange interactions in local-moment compounds.

Finally, in Chapter 5 we summarize the main results presented in this review. We also outline some perspective directions for future research on the role of electronic correlations in various classes of materials building up on the progress achieved to date.

Chapter 2

# *Ab initio* methodology for correlated crystalline materials

## Contents



First-principles techniques based on the density functional theory (DFT)[Hohenberg and Kohn, 1964, Kohn and Sham, 1965] have over the years developed into a sophisticated and reliable tool for predicting the structural stability and ground-state properties of crystalline materials. DFT-based methods excel at predicting relative structural stabilities in $4d$ and $5d$ transition metals (TM), their alloys and intermetallic compounds as a function of the composition and pressure conditions. Forces, phonon spectra in those systems are also quantitatively well captured within DFT. The standard DFT approach is somewhat less useful in assessing electronic excitations in solids. However, for itinerant metallic systems the Kohn-Sham band structure is found to provide a good semi-quantitative description of photoemission data; in the case of semiconductors DFT has a well-known tendency to underestimate fundamental band gaps, while the dispersion of the valence and conduction band are usually found to be in good agreement with experiment.

Though its predictive power for the structural stability of itinerant-electron systems is quite impressive, DFT, in conjunction with standard local or semi-local exchange-correlation functionals, has a clear tendency to predict too small volumes and too large bulk modula for transition-metal oxides (TMO) [Andersen *et al.*, 1980], lanthanide and late actinide metals (see, e.g. [McMahan *et al.*, 1998] and references therein) as well as for a wide range of lanthanide and actinide compounds. This overbinding is due to the fact that TM $d$ states in TMO oxides as well as $f$ states in lanthanide and actinide compounds are predicted by DFT to form partially-filled metallic bands and, hence, to contribute to the cohesion. Such picture is in clear disagreement

with experiments finding many TMO to be insulating [Imada *et al.*, 1998], while valence $f$ states in lanthainides and heavy actinides are typically found to form sharp quasi-multiplet features at high binding energies with the Fermi surface being due to itinerant *spd* bands [Lang *et al.*, 1981]. In the cases when one does observe metallic $d$-like bands in TMO, those metallic states are typically formed by heavily renormalized quasipartilces with the effective masses up to an order of magnitude larger as compared to the ones extracted from the slope of corresponding DFT bands. TMO also exhibit other, non-quasiparticle, spectral features found at binding energies of the order of few eV [Sawatzky and Allen, 1984, Fujimori *et al.*, 1992]; those feature are completely absent from the Kohn-Sham band structure. Even much larger mass enhancements of the order of handreds bare electron masses are observed in $f$-like quasiparticle bands found in many Ce, Yb and U intermetallics [Hewson, 1993]. These "heavy-fermion" bands co-exist at low (usually, below 100 K) temperatures with the usual quasi-multiplet $f$-electron features at high binding energies; with increasing temperature the "heavy-fermion" spectral weight in the vicinity of the Fermi level disappears. Hence, a rather poor description of the ground-state properties of TMO and $f$-electron compounds provided by standard DFT techniques is associated with the loss of any qualitative resemblance between the Kohn-Sham band picture and the experimental photoemission spectra.

The origin for insulating behavior of TM oxides, as was qualitatively understood by N. Mott [Mott, 1949] at the end of 40s, is a quasi-atomic nature of TM $d$ states in those compounds, where the hopping of $d$-electrons is reduced due to an increasing distance between TM atoms as compared to corresponding metals. Therefore, the $d$-electron bandwidth in TMO often becomes smaller than the Coulomb repulsion $U$ between $d$ electrons located on the same site. One may easily show that an electron hop between two neighboring TM ions initially in their ground-state occupancy $N$ increases the Coulomb repulsion energy by about $U$. Correspondingly, an on-site repulsion large compared to the $d$-electron bandwidth impedes the hopping thus forcing an insulating behavior. In other words, an on-site Coulomb interaction comparable to the relevant bandwidth leads to correlated movement of electrons; such correlated electrons cannot be reduced to non-interacting quasiparticles, for which the only effect of interaction is a modest mass enhancement. In the large-$U$ limit quasiparticles completely disappear; one finds a lattice of partially-filled localized $d$ or $f$-shells with charge fluctuations suppressed and low-energy interaction between neighboring ions stemming from virtual hopping processes. Characteristic localized occupied and empty features (lower and upper Hubbard bands) separated by a gap of the order of $U$ are then observed in the photoemission spectra (PES ) of the system.

The effect of $d$ bandwidth being reduced in TM-oxides compared to that in pure TMs is well captured in corresponding Kohn-Sham band structures; the weak $f-f$ hoping in rare-earht (RE) compounds is also clearly reflected in a small (less than 1 eV) bandwidth of the corresponding

Kohn-Sham bands. However, the actual Mott phenomena of an on-site Coulomb repulsion leading to the impeded hopping in such narrow-band systems is completely missed by DFT, due to a deficient description of electronic correlation effects by static and local exchange-correlation (XC) functionals.

The deficiency of the local-density approximation (LDA) for XC effects in narrow-band $d$ and $f$ valence bands was rather quickly realized after band-structure DFT calculations for real simple materials became routine since the end of 70s. First route for correcting this deficiency was based on relaxing the local approximation and, in particular, led to a semi-local generalized-gradient approximation (GGA) [Perdew and Wang, 1992, Perdew *et al.*, 1996a] for the XC potential. GGA is not a significant improvement for strongly-correlated TMO and RE systems, DFT-GGA still predicts narrow metallic bands pinned at the Fermi level with the corresponding overbinding error in the ground-state properties. More recent hybrid XC functionals [Becke, 1993, Perdew *et al.*, 1996b] open a gap between occupied and empty localized states in TMO and lanthanide compounds. However, in the hybrid XC approach the gap formation is associated with a symmetry breaking due to a magnetic order, though the Mott phenomenon is well known to occur also in the paramagnetic state. A characteristic electronic structure of correlated metals combining the high-energy Hubbard bands with metallic quasiparticles is not reproduced by advanced XC functionals.

Another route was to single out narrow-band $d$ and $f$ states for a different treatment as compared to itinerant wide bands that are well described within LDA or GGA. The simplest approach of this kind consists in treating the "offending" partially-filled $d$ and $f$ shells as core states. A more theoretically sound method is based on subtracting the so-called "self-interaction correction" (SIC) [Perdew and Zunger, 1981] that removes an unphysical interaction between an electron and its own Coulomb potential included within LDA or GGA. The SIC correction effectively forces the localization of that electron, hence, the number of localized states is in fact an input parameter.

## 2.1 DFT+U Hamiltonian and its construction

A much more sophisticated treatment of electron correlation effects is based on supplementing the quadratic Kohn-Sham Hamiltonian $H_0$ with explicit local Coulomb interaction, the resulting "DFT+U" Hamiltonian [Anisimov *et al.*, 1991, Anisimov *et al.*, 1997a] reads

$$\hat{H}_{DFT+U} = \hat{H}_0 + \hat{H}_U - E_{DC} = \sum_{\mathbf{k}\nu} \varepsilon_{\mathbf{k}\nu} c^\dagger_{\mathbf{k}\nu} c_{\mathbf{k}\nu} + \sum_{\substack{i, \\ 1,2,3,4}} \langle 12|U|34\rangle f^\dagger_{i1} f^\dagger_{i2} f_{i4} f_{i3} - E_{DC}, \qquad (2.1)$$

where $c^{\dagger}_{\mathbf{k}\nu}(c_{\mathbf{k}\nu})$ is the creation(annihilation) operator for the Kohn-Sham state $\psi_{\mathbf{k}\nu}$ at $k$-point $\mathbf{k}$ and the band index $\nu$, $f^{\dagger}_{i,\alpha}(f_{i,\alpha})$ is the operator creating (annihilating) localized states $w_{i\alpha}$ on the correlated shell in the unit cell $i$[1], $\alpha \equiv 1, 2, ...$ is a compound index for relevant quantum numbers labeling one-electron orbitals within that shell (for example, $\alpha \equiv \{m\sigma\}$, where $m$ is the orbital quantum number and $\sigma$ is the spin). The last term, $E_{DC}$, is the double-counting correction that will be discussed below.

The interacting term in the DFT+U Hamiltonian is naturally defined in the real space, as the interaction is assumed to act between orbitals localized on the same atomic site. A sufficient localization of the orbitals $w_{i\alpha}$ at the correlated site is thus necessary for the DFT+U Hamiltonain to be physically sensible. For extended orbitals the intersite interactions are comparable to $U$; neglecting them in (2.1) thus becomes a poor approximation [Ayral *et al.*, 2013, Hansmann *et al.*, 2013]. However, in solids one cannot define $d$ or $f$ orbital as in an isolated atom, as such definition makes sense near the nucleus, where the crystalline potential is approximately spherical, but not in the interstitial.

There exists a number of approaches for constructing such bases representing localized correlated states in solids. For example, one may employ a basis-independent framework [Marzari and Vanderbilt, 1997, Marzari *et al.*, 2012, Anisimov *et al.*, 2005, Lechermann *et al.*, 2006, Amadon *et al.*, 2008] defining the localized orbitals $w_{i\alpha}$ as Wannier functions constructed from a subset $\mathcal{W}$ of Kohn-Sham bands:

$$w_{i\alpha}(\mathbf{r}) = \sum_{\mathbf{k}\in BZ} w_{\mathbf{k}\alpha}(\mathbf{r}+\mathbf{R}_i)e^{-i\mathbf{k}\mathbf{R}_i} = \sum_{\substack{\mathbf{k}\in BZ \\ v\in\mathcal{W}}} e^{-i\mathbf{k}\mathbf{R}_i}\psi_{\mathbf{k}\nu}(\mathbf{r}+\mathbf{R}_i)P_{\nu\alpha}(\mathbf{k}), \tag{2.2}$$

where the subset $\mathcal{W}$ comprises KS bands with a substantial contribution due to correlated orbitals, $\mathbf{R}_i$ is the lattice vector of the unit cell $i$, $\hat{P}(\mathbf{k})$ is a complex matrix such that the resulting orbitals form an orthonormalized basis, $\langle w_{i\alpha}|w_{j\beta}\rangle = \delta_{ij}\delta_{\alpha\beta}$. In fact, matrices $\hat{P}(\mathbf{k})$ possessing such properties are well-known to be not uniquely defined, the resulting gauge freedom in $\hat{P}(\mathbf{k})$ can be exploited to obtain a well-localized basis of Wannier functions. Direct minimization of the spread of $w_{i\alpha}$ in the real space is employed to construct the maximally-localized Wanniers basis[Marzari and Vanderbilt, 1997]. Another, a projective construction of localized Wannier functions, avoiding the explicit spread minimization, was proposed by [Amadon *et al.*, 2008] and implemented in conjunction with the linearized augmented planewave (LAPW) band structure method by [Aichhorn *et al.*, 2009]. One may also mention a hybrid method of [Andersen and Saha-Dasgupta, 2000, Pavarini *et al.*, 2004], in which Wannier functions are constructed from outward solutions of the radial Schrödinger equation and their energy derivatives on a chosen grid of energies. Another approach [Grechnev *et al.*, 2007]

[1] For simplicity here and below we consider the case of a single correlated site per unit cell

makes use of the fact that some DFT band structure techniques expand Kohn-Sham states $\psi_{\mathbf{k}\nu}$ in a basis containing, among others, suitable "atomic-like" functions for a given correlated shell; such functions are then employed as a correlated-subspace basis. A somewhat older method of [Savrasov and Kotliar, 2004] writes the whole Hamiltonian (2.1) using atomic-like basis functions instead of $\psi_{\mathbf{k}\nu}$ and employs a subset of them to represent correlated orbitals; this approach is applicable only for few band-structure techniques employing such suitable basis functions.

Once the basis of correlated orbitals $w_{i\alpha}$ is chosen one needs to determine the on-site Coulomb repulsion between them. In principle, one may easily evaluate matrix elements of the bare Coulomb interactions $u(\mathbf{r}) = 1/r$ between such orbitals. The bare Coulomb repulsion is, however, known to be a very poor approximation for the local interaction in solids entering in eq. 2.1. For example, the average over its matrix elements between Ni $3d$ orbitals in NiO evaluates to about 20−25 eV [Sakuma and Aryasetiawan, 2013]. Experimentally, though, one finds that the splitting between occupied and empty $3d$ localized features seen in the PES/inverse-PES spectra, which is, to a first approximation, the average $\langle U \rangle$, amounts only to about 9 eV [Reinert and Hüfner, 2005][2]. This discrepancy is, of course, due to the fact that the on-site interaction between localized orbitals in solids is strongly screened by itinerant states. Hence, one should view the Hamiltonian (2.1) as a *low-energy* description of the correlated system, where the interactions between localized states $w_{i\alpha}$ and itinerant bands, which are not explicitly included, have been integrated out. In result, the effective Coulomb repulsion $u(\mathbf{r}, \mathbf{r}', \omega)$ acquires a frequency dependence, which is then passed to matrix elements in the correlated-orbitals basis:

$$\langle 12|U|34\rangle(\omega) = \int d\mathbf{r} d\mathbf{r}' w^*_{i1}(\mathbf{r}) w^*_{i2}(\mathbf{r}') u(\mathbf{r}, \mathbf{r}', \omega) w_{i3}(\mathbf{r}) w_{i4}(\mathbf{r}'), \tag{2.3}$$

with the low-frequency limit of $\langle 12|U|34\rangle(\omega)$ giving a value of on-site repulsion that is strongly reduced by screening; it is relevant for the low-energy physics described by (2.1) . The high-frequency limit of $\langle 12|U|34\rangle(\omega)$ approaches the bare Coulomb value; this high-frequency tail of $\langle 12|U|34\rangle(\omega)$ may affect the low-energy physics producing an additional enhancement of quasiparticle renormalization [Casula *et al.*, 2012b]; it also induces high-energy plasmonic spectral features [Casula *et al.*, 2012a].

Due to this complex effect of screening the local Coulomb repulsion is rather difficult to evaluate from first principles and often treated as a parameter. A more consistent and truly *ab initio* approach is based on evaluating the screening of local repulsion between a given set of local orbitals $w_{i\alpha}$ from the Kohn-Sham band structure. One popular approach of this kind, the constrained random-phase approximation (cRPA) [Aryasetiawan *et al.*, 2004], separates

[2] The optical gap of about 4 eV in this compounds is of the charge-transfer (O $2p \rightarrow$ Ni $3d$) type.

the polarization function $\Pi(\omega) = \Pi_c(\omega) + \Pi_r(\omega)$ evaluated within RPA into the contribution $\Pi_c(\omega)$ due to transitions within the subset of correlated bands $\mathcal{W}$ and $\Pi_r(\omega)$ due to all other transitions. Then the relevant interaction is obtained by screening the bare Coulomb repulsion $v(\mathbf{r})$ with $\Pi_r$ and then projecting $u(\mathbf{r}, \mathbf{r}', \omega)$ into the subspace of $w_{i\alpha}$ using (2.3). The cRPA method is a powerful technique that is able to obtain all matrix elements of $\langle 12|U|34\rangle(\omega)$ with their frequency dependence. However, cRPA is not particularly well suited for the case of a significant entanglement between the correlated $\mathcal{W}$ and itinerant band subspaces. It is difficult to define a consistent separation of the polarization into $\Pi_c(\omega)$ and $\Pi_r(\omega)$ in this case, though some versions of cRPA to handle this entanglement have been formulated [Miyake *et al.*, 2009, Seth *et al.*, 2017].

An alternative approach to first-principles evaluation of the local interaction is based on the assumption that a quantitatively correct static screening of the on-site interaction is already included at the DFT level through the local XC potential. This approach named constrained LDA (cLDA) [Dederichs *et al.*, 1984, Hybertsen *et al.*, 1989, Cococcioni and de Gironcoli, 2005] constrains the charge on the localized shell of interest on a single site within a supercell with other states unconstrained, hence, allowed to screen the on-site interaction. The band energy of corresponding "constrained" KS states is then evaluated as a function of its orbital occupancy allowing to extract the direct Coulomb repulsion parameter $U$ and Hund's rule coupling $J_H$. The method was shown to provide reasonable values of the static interaction, though it is not free from uncertainties.

The Kohn-Sham band structure, which is the quadratic part of the DFT+U Hamiltonian (2.1), is that of non-interacting electrons moving in an effective potential. However, this potential contains, among other terms, the Hartree and XC potentials corresponding to the electron density of the Kohn-Sham states. Hence, the Kohn-Sham bands are not truly that of a non-interacting system. In particular, the effect of the screened Coulomb interaction $u(\mathbf{r}, \mathbf{r}', \omega)$ acting between correlated orbitals is included in a static mean-field way by LDA; this fact is used by the cLDA method described above to extract the value of this interaction. As the same interaction explicitly enters into (2.1), it is necessary to remove this static mean-field contribution from the same Hamiltonain to avoid counting it twice. Hence, the corresponding double-counting correction (DC) is included as the last term into (2.1).

Though the local screened interaction is certainly included in some form by XC potentials determining its exact contribution is a highly nontrivial problem. Local and semi-local XC potentials are functions of the full charge density and also non-linear; they cannot be represented as a superposition of contribution due to different orbitals. Hence, the problem of formulating a theoretically sound expression for the DC term has not been fully solved to date. There exist a number of different DC formulae [Anisimov *et al.*, 1991, Czyżyk and Sawatzky, 1994,

Lichtenstein *et al.*, 2001, Park *et al.*, 2014b, Haule, 2015]. The most widely used ones are derived by assuming that XC potentials include the local Coulomb interaction in an orbitally-independent form. That form is given by the Hartree-Fock potential due to the on-site interaction term in (2.1) for a particular limit of the correlated-shell occupancy matrix. It is assumed to be uniform within the "around-mean-field" (AMF) approach [Anisimov *et al.*, 1991], which is usually employed for weakly and moderately-correlated metals. The alternative "fully-localized-limit' (FLL) form [Czyżyk and Sawatzky, 1994] assumes the most non-uniform occupancy matrix for a given shell filling and is generally employed for strongly-correlated systems like Mott insulators. The contribution due to this term into the one-electron potential for a given orbital $\alpha$ is given by

$$\Sigma^{\alpha}_{DC} = \frac{\partial E_{DC}}{\partial \rho_{\alpha}}|_{\hat{\rho}_{DC}}, \tag{2.4}$$

where the derivative over the orbital occupancy $\rho_{\alpha}$ is taken at the shell's occupancy matrix $\hat{\rho}_{DC}$ corresponding to a given limit (AMF, FLL, etc.).

## 2.2 Dynamical mean-field theory

Once all terms in the Hamiltonian (2.1) are determined the next step is, obviously, solving it to obtain the ground-state and excited properties of a given real system. This represents a formidable problem, as one may notice that this Hamiltonian can be viewed as a multi-band generalization of the famous one-band Hubbard model (HM) for which no exact solution is known for the relevant 2d and 3d cases. A breakthrough in the study of HM was achieved in the beginning of 90th in the framework of dynamical mean-field theory (DMFT) [Metzner and Vollhardt, 1989, Georges and Kotliar, 1992, Georges *et al.*, 1996]. Though initially the DMFT formalism was written for the one-band HM, here we present its formulation for the Hamiltonian (2.1) in view of applications to realistic materials. The DMFT framework focuses on the one-electron Green's function (GF) defined in the Kohn-Sham space and imaginary-time domain[3] as $G_{\nu\nu'}(\mathbf{k}, \tau - \tau') = -\langle \mathrm{T}[c_{\mathbf{k}\nu}(\tau) c^{\dagger}_{\mathbf{k}\nu'}(\tau')]\rangle$, where T is the time-ordering operator. Its Fourier transform $G(\mathbf{k}, i\omega_n)$ is the GF in the imaginary-frequency domain, where $i\omega_n = i\pi(2n-1)T$ is the fermionic Matsubara grid for the temperature $T$. Correlation effects arising due to the interaction $U$ term of (2.1) are encoded in the Kohn-Sham space by the electronic self-energy $\Sigma^{KS}(\mathbf{k}, i\omega_n) = \hat{P}^{\dagger}(\mathbf{k})\Sigma(\mathbf{k}, i\omega_n)\hat{P}(\mathbf{k})$ , where $\hat{P}(\mathbf{k})$ are projector matrices (2.2) to the correlated subspace, $\Sigma(\mathbf{k}, i\omega_n)$ is the self energy in that subspace spanned by the localized orbitals (2.2). The interacting lattice GF is thus obtained by inserting

[3] The imaginary time/frequency domain is often used in DMFT calculations for the technical reasons outlined in Sec. 2.2.1, though it is not necessary.

$\Sigma(\mathbf{k}, i\omega_n)$ through the Dyson equation:

$$G^{-1}(\mathbf{k}, i\omega_n) = G_0^{-1}(\mathbf{k}, i\omega_n) - \hat{P}^\dagger(\mathbf{k}) \left(\Sigma(\mathbf{k}, i\omega_n) - \Sigma_{DC}\right) \hat{P}(\mathbf{k}), \tag{2.5}$$

into the non-interacting lattice GF $G_0$ given by the first term of (2.1), with the DC for the self-energy defined by (2.4).

The DMFT is based on the key observation of [Metzner and Vollhardt, 1989] that one may define a (non-trivial) infinite-dimensional limit of (2.1), and that the electronic self-energy becomes purely local in this limit, i. e., **k**-independent[4], $\Sigma(\mathbf{k}, i\omega_n) \xrightarrow{d\to\infty} \Sigma(i\omega_n)$. Such single-site self-energy is given by the summation over irreducible (skeleton) Feynman diagrams involving only the single-site GF and the local vertex $\hat{U}$. The coupling between a representative correlated shell $o$ and an effective electronic "bath" representing the rest of system is then given by the bath Green's function:

$$\mathcal{G}_0^{-1}(i\omega_n) = \left[\sum_{\mathbf{k}} \hat{P}(\mathbf{k}) G(\mathbf{k}, i\omega_n) \hat{P}^\dagger(\mathbf{k})\right]^{-1} + \Sigma(i\omega_n) = i\omega_n - \hat{\varepsilon} - \Delta(i\omega_n), \tag{2.6}$$

where $\hat{\varepsilon}$ are bare (non-interacting) single-site level positions, $\Delta(i\omega_n)$ is the hybridization function due to hopping between the site and electronic bath. The single-site problem in the correlated subspace is completely defined by (2.6) and on-site Coulomb replusion $\hat{H}_U^{(o)} = \sum_{1,2,3,4} \langle 12|U|34\rangle f_1^\dagger f_2^\dagger f_4 f_3$ (omitting the irrelevant site index $o$). The lattice problem is thus mapped into an auxilary *quantum impurity problem* (QIP) [Georges and Kotliar, 1992] for a single correlated shell, which is fully analogous to the standard Anderson impurity model (AIM). However, in contrast to the usual AIM, $\Delta(i\omega_n)$ is not given by the hybridization of non-interacting bands; it should be rather viewed as a dynamical mean-field implicitly depended on the single-site self-energy through eqs. (2.5-2.6). By solving the QIP, i. e., by summing (all or subset of) local Feynman diagrams one obtains the impurity GF and self-energy:

$$\left\{\mathcal{G}(i\omega_n), \hat{H}_U^{(o)}\right\} \to \left\{G_{imp}(i\omega_n), \Sigma_{imp}(i\omega_n)\right\}. \tag{2.7}$$

One then employs the standard recipe to close the mean-field cycle as shown in Fig. 2.1: the obtained impurity self-energy is inserted for all correlated shells, $\Sigma(\mathbf{k}, i\omega_n) \equiv \Sigma_{imp}(i\omega_n)$ allowing to update the chemical potential $\mu$ and to recalculate the mean field $\mathcal{G}_0$ by eqs. (2.5-2.6). This cycle is iterated until the self-consistency is reached: the QIP solved for the mean-field $\mathcal{G}_0$ results in the same self-energy $\Sigma$ that was used to obtain this mean-field through (2.5-2.6). Alternatively,

[4] In the case of DFT+U Hamiltonian (2.1) this approximation is applied to the self-energy $\Sigma(\mathbf{k}, i\omega_n)$ in the correlated subspace, while $\Sigma^{KS}$ can still be **k** dependent due to the projectors $\hat{P}(\mathbf{k})$.

the same self-consistency condition is represented by $G_{imp}(i\omega_n) = G_{loc}(i\omega_n)$, where

$$G_{loc}(i\omega_n) = \sum_{\mathbf{k}} \hat{P}(\mathbf{k}) G(\mathbf{k}, i\omega_n) \hat{P}^{\dagger}(\mathbf{k}) \tag{2.8}$$

is the local GF of lattice problem. The problem defined by the Hamiltonian (2.1) is thus exactly solved in the limit of infinite lattice connectivity, as can be also shown explicitly, see [Georges *et al.*, 1996]. As for any mean-field approach the usefulness of DMFT method is based on its ability to describe the realistic 3d lattices, for which the single-site approximation $\Sigma(\mathbf{k}, i\omega_n) \to \Sigma(i\omega_n)$ appears to be rather reasonable, though it is not quantitatively exact. At the same time the single-site dynamics due to electronic correlations is fully included in DMFT; this explains its success in reproducing such non-perturbative phenomena as the Mott transition. The method captures not only the insulating $U/W \to \infty$ and non-interacting $U/W \to 0$ limits (where $W$ is the bandwidth of non-interacting bands $\varepsilon_{vk}$ in (2.1)) but also all intermediate regimes given by finite $U/W$.

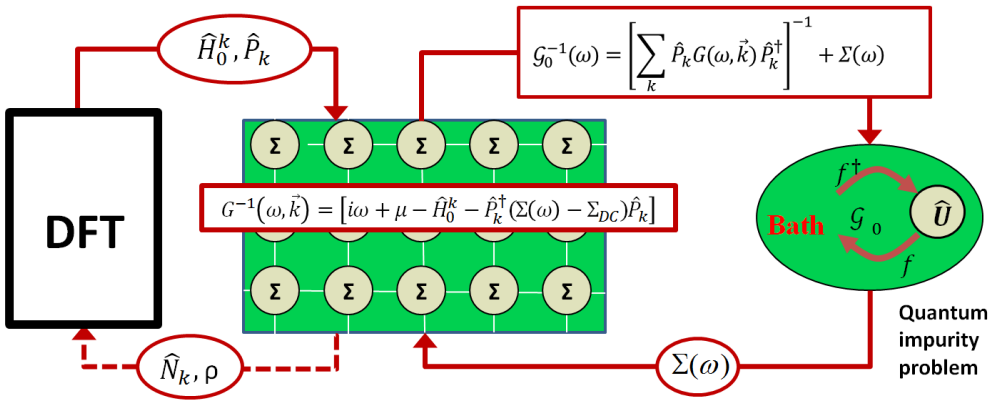


Figure 2.1: Schematic diagram of the DFT+DMFT method. The initial input from the DFT part is the quadratic KS Hamiltonain $\hat{H}_0$ and projectors $\hat{P}$ between the KS space and correlated subspace. The right-hand side represents the DMFT cycle with the lattice problem mapped into the quantum-impurity one using eq. 2.6; the calculated impurity self-energy subsequently is inserted back to the lattice, eq. 2.5. The updated DMFT density matrix can be inserted back to the DFT part (dashed arrow) to take into account modifications of the charge density and, therefore, $\hat{H}_0$, due to correlations; this results in a DFT+DMFT framework that is self-consistent in the charge density.

For 2d and quasi-2d systems the single-site DMFT is generally not an adequate approximation. The $\mathbf{k}$ dependence of the self-energy is key to describe, for example, the physics of layered cuprate superconductors, in particular, their PES [Damascelli *et al.*, 2003]. This problem was addressed by cluster extensions of the single-site DMFT, which were formulated in both the real and reciprocal spaces [Potthoff *et al.*, 2003, Maier *et al.*, 2005, Ferrero *et al.*, 2009]. The

single-site QIP (2.7) is thus generalized to the corresponding cluster problem. Such generalization increases dramatically the computational cost of solving the QIP, hence, the cluster methods are not generally applicable to full $d$ and $f$ shells; they have been extensively applied to quasi-1band systems like layered cuprates. Another more recent effort in development of extended-DMFT frameworks [Rubtsov *et al.*, 2008, Held *et al.*, 2008, Ayral and Parcollet, 2015] is based on applying the single-site approximation to two-electron correlation functions (like the vertex function) while keeping the **k**-dependence of the one-electron self-energy. These approaches are promising for applications to multiband systems, though they are still currently too heavy for applications in the cases considered in this review, when many-electron effects for the full $d$ or $f$ shell need to be taken into account.

### 2.2.1 The quantum impurity problem

The QIP problem schematically given by eq. 2.7 is a true many-electron problem, though a single-site one, and represents, in fact, a numerical "bottleneck" of the DFT+DMFT framework. In the imaginary-time path integral formalism (see e.g. [Negele and Orland, 1988]) it reads

$$G_{\alpha\alpha'}(\tau_0 - \tau_1) = \frac{1}{Z}\int \mathcal{D}[f, f^\dagger] f_\alpha(\tau_0) f^\dagger_{\alpha'}(\tau_1) \exp[-S], \tag{2.9}$$

where $\mathcal{D}[f, f^\dagger]$ is the path integration over all impurity degrees of freedom and

$$Z = \int \mathcal{D}[f, f^\dagger] \exp[-S] \tag{2.10}$$

is the impurity partition function, $S$ is the impurity action:

$$S = \sum_{\alpha_1\alpha_2} \int d\tau \int d\tau' f^\dagger_{\alpha_1}(\tau) \left[\mathcal{G}_0^{-1}(\tau - \tau')\right]_{\alpha_1\alpha_2} f_{\alpha_2}(\tau') + \int d\tau \hat{H}_U^{(o)}(\tau). \tag{2.11}$$

Many-body methods to evaluate (2.9) represent a large research field initiated by early studies of AIM and very actively developed at present, in particular, to provide efficient quantum-impurity "solvers" for the DMFT framework. They will not be reviewed here in any details; we will only briefly outline main strategies for solving the QIP and provide some useful references.

The methods dealing with QIP can be divided into numerically-exact and approximate analytical kinds. Among the former one may especially mention stochastic quantum Monte Carlo (QMC) methods; a breakthrough in this domain has been achieved by so-called "continuous-time" (CT) QMC methods [Prokof'ev and Svistunov, 1998] (see review [Gull *et al.*, 2011] on its applications to the fermionic QIP). The most popular CT-QMC approaches are based on an expansion of the partition function (2.10) in powers of $\hat{H}_U^{(o)}$ [Rubtsov *et al.*, 2005] or, alter-

natively, in powers of the hybridization function $\Delta(\tau)$, see eq. 2.6, [Werner *et al.*, 2006]. One subsequently sums up various diagrammatic contributions into GF (2.9) and other correlation function in accordance with their relative weight in $Z$ by employing a Monte Carlo importance sampling. In contrast to the older QMC approach of Hirch and Fye [Hirsch and Fye, 1986] based on discretization of the integrals over $\tau$ in (2.11) the CT-QMC approach is free from the discretization error and can treat more complex interaction vertices $\hat{H}_U^{(o)}$. All these QMC methods work in the imaginary-time/imaginary-frequency domain, hence, the resulting GF needs to be analytically continued to the real-energy axis to obtain an experimentally-observable real-frequency spectra.

The hybridization-expansion CT-QMC technique employed as a quantum-impurity solver in the DFT+DMFT calculations of Chapter 3. This approach is sufficiently computationally efficient to solve the QIP for the whole Fe $3d$ shell. Particularly, the case of simplified, "density-density" Coulomb vertex $\hat{H}_U^{(o)}$ reducible to the form $\sum_{\alpha\alpha'} U_{\alpha\alpha'}\hat{n}_\alpha\hat{n}_{\alpha'}$ allows to employ the fast "segment-picture" algorithm [Werner *et al.*, 2006, Gull *et al.*, 2011], reducing the computational effort very significantly. The density-density approximation neglects some potentially important matrix elements of the Coulomb vertex[5] and thus introduces a system-dependent error. In the case of moderately-correlated metal like iron it does not affect the qualitative picture, but is still quantitatively important (see Appendix A); for strongly-correlated systems as, for example, FeSe [Aichhorn *et al.*, 2010] this approximation may lead to qualitatively wrong results. Calculation with the full 4-index vertex are much more computationally demanding, but still nowdays possible thanks to a recent development of fast algorithms [Läuchli and Werner, 2009, Gull, 2008].

Another popular numerically-exact approach, the exact diagonalization technique [Caffarel and Krauth, 1994], see also [Lu *et al.*, 2014, Go and Millis, 2017] for more recent developments. It is based on representing the hybridization function by a set of auxiliary discrete levels $\{\varepsilon_b\}$ mixing with the impurity states, $\Delta_{\alpha\alpha'}(\omega) \sim \sum_b \frac{V_{b\alpha}V^\dagger_{b\alpha'}}{\omega-\varepsilon_b}$. The resulting large Hamiltonian including both impurity and bath states is subsequently diagonalized by Lanczos or similar techniques allowing to compute the impurity GF from obtained eigenvalues and eigenstates. Among the exact methods one should also mention the numerical renormalization-group and density-matrix renormalization-group methods [Bulla *et al.*, 2008, Hallberg, 2006].

Analytical approaches are generally applicable only in certain regimes (strong or weak coupling). Weak-coupling methods are suitable for metallic phases; they are based on the standard Wick theorem and subsequent summation of a certain subset of Feynmann diagrams, like, for example, the fluctuation-exchange approximation [Katsnelson and Lichtenstein, 1999,

[5] For example, the "spin-flip" contributions to $\hat{H}_U^{(o)}$ of the form $f^\dagger_{m\uparrow}f^\dagger_{m'\downarrow}f_{m'\uparrow}f_{m\downarrow}$ cannot be reduced to a density-density form.

Drchal *et al.*, 2005, Pourovskii *et al.*, 2005]. Strong-coupling methods employ the hybridization as a small parameter, they are briefly described in Sec. 4.1. Among numerous other analytical methods one may also mention the "slave" particle approach [Kotliar and Ruckenstein, 1986, de'Medici *et al.*, 2005, Lechermann *et al.*, 2007, Rohringer *et al.*, 2018] providing an economical and numerically efficient treatment of the quasiparticle renormalization in multiband systems. The obvious advantage of these analytical techniques is their computational efficiency. They can also easily evaluate the GF and, hence, the measurable one-electron spectra, at the real-frequency axis.

Finally, the simplest approach to solving the QIP consists in employing the static Hartree-Fock approximation; in this case DFT+DMFT is reduced to the popular LDA+U method [Anisimov *et al.*, 1991, Anisimov *et al.*, 1997a].

## 2.3 Charge density and total energy

As a result of the DMFT cycle (Fig. 2.1) one obtains the converged interacting lattice GF (2.5) in the KS space. The corresponding density matrix

$$N^{\mathbf{k}}_{\nu\nu'} = \sum_n G_{\nu\nu'}(\mathbf{k}, i\omega_n) e^{i\omega_n 0^+} \tag{2.12}$$

gives the contribution of KS bands in $\mathcal{W}$ to the charge density. Therefore, the charge density $n(\mathbf{r})$ is affected by many-electron effects through the DMFT self-energy $\Sigma(i\omega_n)$ entering into $G(\mathbf{k}, i\omega_n)$; the KS one-electron potential being a functional of $n(\mathbf{r})$ is thus modified as well. Hence, the one-electron part $H_0$ of the DFT+U Hamiltonain (2.1) comes out to be implicitly dependent on $\Sigma(i\omega_n)$.

This observation led to formulation of the charge self-consistent DFT+DMFT framework, in which $n(\mathbf{r})$ and $H_0$ are consistently updated to take into account the impact of correlations as shown in the left-hand side of Fig. 2.1. In practice, $\hat{N}^{\mathbf{k}}$ in the KS basis is submitted back to the DFT part; the corresponding contribution to $n(\mathbf{r})$ is then calculated through the expansion of $\psi_{\mathbf{k}\nu}$ in the basis of a given band-structure method. Several such self-consistent DFT+DMFT frameworks have been implemented recently [Savrasov and Kotliar, 2004, Minár *et al.*, 2005, Pourovskii *et al.*, 2007, Haule *et al.*, 2010, Aichhorn *et al.*, 2011, Gråsäs *et al.*, 2012, Park *et al.*, 2014a].

In this self-consistent framework the DMFT self-consistency condition, $G_{loc} \equiv G_{imp}$, as well as the relation between the KS potential and electronic density are derived by extremization of the following DFT+DMFT grand potential [Kotliar *et al.*, 2006] :

$$\begin{aligned}\Omega\left[n(\mathbf{r}), G_{loc}, \Delta\Sigma, \hat{\varepsilon}\right] = &- \operatorname{Tr}\ln\left[i\omega_n + \mu - H_0 - \Delta\Sigma\right] - \operatorname{Tr}\left[G_{loc}\Delta\Sigma\right] \\ &+ \sum_{\mathbf{R}}\left[\Phi_{imp}[G_{loc}(\mathbf{R})] - \Phi_{DC}[G_{loc}(\mathbf{R})]\right] + \Omega_r[n(\mathbf{r})] \\ &\equiv \Delta\Omega\left[G_{loc}, \Delta\Sigma, V_{KS}\right] + \Omega_r[n(\mathbf{r})],\end{aligned}$$

where $\Delta\Sigma$ is the difference between the impurity self-energy $\Sigma_{imp}$ and the double counting correction (2.4), $\Phi_{imp}[G_{loc}(\mathbf{R})]$ is the DMFT interaction energy functional for the site $\mathbf{R}$, $\Phi_{DC}[G^{loc}_{\mathbf{R}}]$ is the corresponding functional for the double-counting correction. The last term $\Omega_r[n(\mathbf{r})]$ depends only on the electronic charge density $n(\mathbf{r})$ and comprises the electron-nuclei, Hartree and exchange-correlation contribution, while all other terms collected in $\Delta\Omega\left[G_{loc}, \Delta\Sigma, V_{KS}\right]$ do not have an explicit dependence on $n(\mathbf{r})$. From the zero-temperature limit of (**??**) one derives [Amadon *et al.*, 2006] the following expression for the total energy:

$$E_{DFT+DMFT} = \sum_{\mathbf{k}\nu}\varepsilon_{\mathbf{k}\nu}N^{\mathbf{k}}_{\nu\nu} + \langle H_U\rangle - E_{DC} + E_{en}[n(\mathbf{r})] + E_H[n(\mathbf{r})] + E_{xc}[n(\mathbf{r})], \tag{2.13}$$

where $E_{en}$, $E_H$, $E_{xc}$ are the standard DFT electron-nuclei, Hartree and exchange-correlation contributions evaluated from the charge density $n(\mathbf{r})$ that includes the DMFT correction. The interaction energy $\langle H_U\rangle$ can be evaluated from the self-energy using the Migdal formula $\langle H_U\rangle = \frac{1}{2}\operatorname{Tr}\left[\Sigma_{imp}G_{imp}\right]$, alternatively, the expectation value $\langle f_1^\dagger f_2^\dagger f_3 f_4\rangle$ can be directly measured, e. g., by using QMC quantum-impurity solvers.

Instead of the self-consistent charge density $n(\mathbf{r})$ one may employ in (2.13) the DFT one, $n_{DFT}(\mathbf{r})$ resulting in the so-called "one-shot DMFT" scheme. The impact of the self-consistency in charge density on the DFT+DMFT total-energy and spectra has been studied in a number of works [Pourovskii *et al.*, 2007, Aichhorn *et al.*, 2011, Amadon, 2012, Leonov *et al.*, 2015, Bhandary *et al.*, 2016], though a consistent assessment for the full range of correlation strength is still lacking. However, the charge-density self-consistency seems to important for localized systems as $\gamma$-Ce and Ce oxides [Pourovskii *et al.*, 2007] and $VO_2$ [Leonov *et al.*, 2015]. The possible reason pointed out by [Bhandary *et al.*, 2016] is that the occupancy of $\psi_{\mathbf{k}\nu}$ states is very different in the localized limit as compared to a metallic band structure predicted by DFT. In the former case the KS states $\mathbf{k}\nu$ of correlated bands will be all roughly half-filed due to the contribution of corresponding lower Hubbard band. In DFT the KS states $\mathbf{k}\nu$ are occupied below $E_F$ and empty above, hence, the occupancy varies strongly in the $\mathbf{k}$ space. Another important effect of the charge-density self-consistency is an overall lower sensitivity of the result to the choice of DC; changes in DC seem to be compensated by the corresponding modifications in $V_{KS}$ [Aichhorn *et al.*, 2011].

Chapter 3

# Electronic correlations in iron under extreme conditions

Contents



## 3.1 Introduction

Iron is a key material for our civilization since the advent of "Iron Age" at about 1000 BC. The technological utility of iron originates in a vast phase space provided by iron-based alloys, allowing for divers microstructures to be produced with small variations in the composition and an appropriate thermal treatment. In particular, the rich zoo of steels is composed by three stable phases - the ferrite (body-centered cubic, bcc, $\alpha$) austenite (face-centered cubic, fcc, $\gamma$) and cementite (orthorhombic carbide $Fe_3C$) - in addition to various metastable phases, for example, the body-centered tetragonal martensite $\alpha'$ (see, e.g., [Bhadeshia and Honeycombe, 2006]). This multitude of phases observed in iron-based alloys and compounds stems from the complex physics of pure iron, which features three distinct allotropes at the ambient pressure: ground-states bcc $\alpha$-Fe transforms into fcc $\gamma$-Fe at 1185 K; the fcc phase subsequently transforms to yet another bcc phase, $\delta$-Fe, at 1667 K. Though $\alpha$ and $\delta$-Fe have the same bcc crystal structure, their physics is quite different, with the vibrational entropy believed to be playing the key role in stabilization of the later [Neuhaus *et al.*, 2014]. Iron is a classic itinerant ferromagnet, and the

ferromagnetic order is well recognized to be crucial in stabilizing $\alpha$-Fe [Zener, 1955]. However, as noted above, the $\alpha$ phase still exists above the Curie temperature of 1044 K. The fcc $\gamma$ phase is paramagnetic in its bulk form stable only at high-temperatures. However, $\gamma$-Fe can be stabilized in small precipitates in an fcc matrix, e.g., in Cu, down to zero temperature, and at low temperatures it exhibits a complex non-commensurate antiferromagnetic order [Tsunoda, 1989].

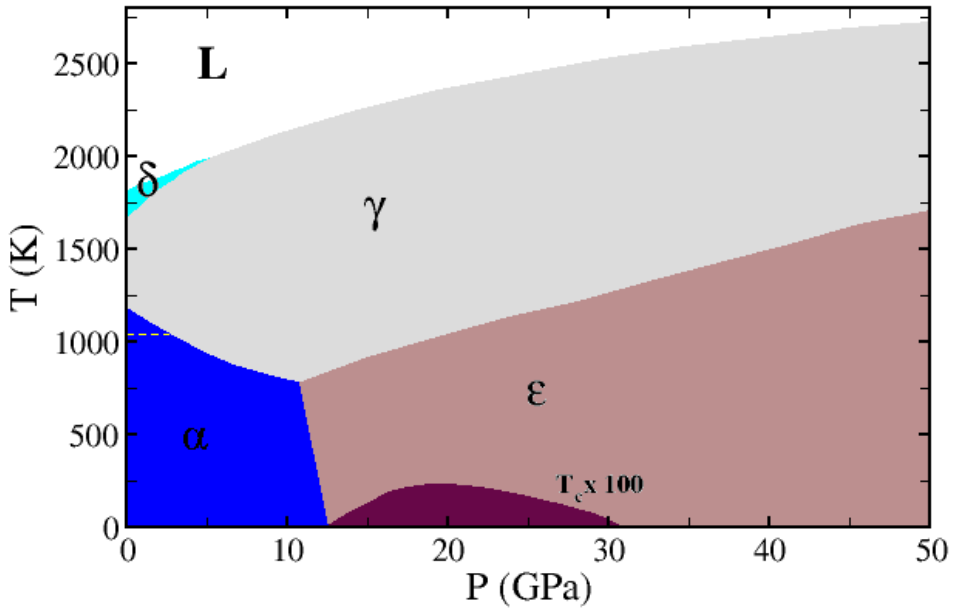


Figure 3.1: The pressure-temperature phase diagram of iron in the moderate pressure range up to 50 GPa. The superconducting transition temperature for $\varepsilon$-Fe is multiplied by 100. The yellow horizontal dashed line in the $\alpha$-Fe region indicates its ferromagnetic $T_c$.

Under applied pressures above 10 GPa $\alpha$-Fe transforms into another allotrope, hexagonal close-packed $\varepsilon$-Fe [Bancroft *et al.*, 1956, Jamieson and Lawson, 1962]. This phase is found to be stable at room temperature up to highest pressures reached to date [Mao *et al.*, 1990]; *ab initio* DFT calculations predict iron to remain in the $\varepsilon$ phase up to pressures of the order of 10 TPa [Stixrude, 2012]. Experimental studies of $\varepsilon$-Fe under moderate pressures reveal a superconducting dome in the range of pressures from 10 to 30 GPa with the maximum value of superconducting $T_c$ of about 2 K [Shimizu *et al.*, 2000]; this superconductivity is likely of non-conventional nature and mediated by spin-fluctuations [Mazin *et al.*, 2002]. No magnetic order has been detected in $\varepsilon$-Fe down to temperatures as low as 8 K [Cort *et al.*, 1982, Papandrew *et al.*, 2006]. A puzzling non-Fermi-liquid (nFL) temperature scaling $\propto T^{5/3}$ of the low-temperature resistivity of $\varepsilon$-Fe was also reported [Holmes *et al.*, 2004, Yadav *et al.*, 2013].

This rich phase diagram (Fig. 3.1) with several allotropes exhibiting various magnetic orders, a non-conventional superconductivity as well as instances of a nFL behavior in the $\varepsilon$-phase hint

at a complex many-electron physics of iron metal. Many-electron effects in iron are expected to arise due to the on-site Coulomb repulsion between rather localized $3d$ states hybridized with itinerant $4s$ bands. The typical width $W$ of the iron $3d$ band is in the range of 5 to 6 eV at ambient-moderate pressures; the estimated value of the local Coulomb interaction parameter $U$ (Slater $F^0$) is in the range from 2.3 to 6 eV, in accordance with cLDA [Anisimov *et al.*, 1991, Cococcioni and de Gironcoli, 2005, Belozerov and Anisimov, 2014] and cRPA [Miyake and Aryasetiawan, 2008, Miyake *et al.*, 2009] calculations. In spite of a large spread in the theoretical estimates of $U$, one may conclude that the ratio $U/W$ in Fe is less than or equal to 1. Taking into account only the effect of $U \leq W$ one would expect rather weak electronic correlation effects in a multiband system away from half-filling [Han *et al.*, 1998]. Indeed, the strength of electronic correlations in iron is found to be much more sensitive to Hund's coupling $J_H$, which value is in the range of 0.85 to 1 eV. In this respect the physics of iron is close to that of "Hund's metals" [de' Medici *et al.*, 2011, Haule and Kotliar, 2009, Georges *et al.*, 2013], in which the strength of correlations away from half-filling is determined mainly by $J_H$. In particular, model studies point out to a key role of $J_H$ in stabilizing the ferromagnetic phase in multiband systems away from half-filling [Frésard and Kotliar, 1997]. Another important aspect is the interplay between the local Coulomb interaction, characterized by large $J_H$, and crystal-field splitting of Fe $3d$ states. This interplay is particularly striking in the bcc $\alpha$ phase, where the partial $e_g$ density-of-states (DOS) features a large peak pinned at the Fermi level due to a van Hove singularity [Maglic, 1973, Irkhin *et al.*, 1993]. Correspondingly, this high DOS at the Fermi level in nonmagnetic $\alpha$-Fe explains its tendency towards the ferromagnetism in accordance with the Stoner criterion.

The Stoner ferromagnetism of $\alpha$-Fe is well captured by DFT calculations in conjunction with the local spin-density approximation (LSDA) exchange-correlation functional predicting the theoretical ordered moment of 2.2 $\mu_B$ that agrees well with experiment. Though DFT-LSDA incorrectly predicts $\gamma$-Fe to be the ground states [Wang *et al.*, 1985], this error is corrected by semi-local exchange-correlation potentials like GGA [Singh *et al.*, 1991, Amador *et al.*, 1992]. However, the existence of paramagnetic bcc phase is a significant challenge for the density-functional theory. Direct DFT calculations predict too small volume and too high bulk modulus for non-magnetic $\alpha$-Fe; moreover, this non-magnetic phase is mechanically and dynamically unstable within DFT [Hsueh *et al.*, 2002, Leonov *et al.*, 2012], in clear disagreement with experiment. DFT calculations predict paramagnetic $\gamma$-phase to be dynamically unstable as well [Leonov *et al.*, 2012]. A number of methods has been developed in the DFT framework to remedy its deficiency in describing paramagnetic phases. Several such techniques were subsequently applied to iron, like the disordered local-moments method [Gyorffy *et al.*, 1985, Okatov *et al.*, 2009, Zhang *et al.*, 2011], the spin-statistical-averaging method of Körmann *et*

*al.* [Körmann *et al.*, 2008], or the spin-wave approach of [Ruban and Razumovskiy, 2012], for a recent review of such techniques see, e.g., [Abrikosov *et al.*, 2016]. However, these techniques represent the paramagnetic state by a certain combination of systems with static local moments; their applicability to the cases like $\varepsilon$-Fe, where no static magnetic order or local-moment behavior is observed at any $T$, is not obvious. Moreover, such approaches are useful to describe the thermodynamics of local-moment paramagnets, but they are not designed to capture their spectral or transport properties. And even for ferromagnetic $\alpha$-Fe the DFT electronic structure is only in a rough qualitative agreement with experimental photoemission spectra, missing, in particular, the observed quasiparticle renormalization of the $3d$ bands by 40-50% and a lifetime damping of quasiparticle states [Schäfer *et al.*, 2005] .

This inability of pure DFT to fully capture the physics of iron at ambient condition, in particular, of high-temperature paramagnetic $\alpha$-Fe as well as the $\gamma$ and $\delta$ phases has prompted a number of DFT+DMFT studies of this system. In particular, Leonov and coworkers applied DFT+DMFT in conjunction with a quantum Monte Carlo impurity solver to obtain total energies and phonon dispersions in paramagnetic $\alpha$ and $\gamma$ phases [Leonov *et al.*, 2011, Leonov *et al.*, 2012]. Their calculations predicting dynamically and thermodynamically stable paramagnetic $\alpha$-Fe in the range of temperatures from $T_c$ to $1.3T_c$, in qualitative agreement with experimental phase diagram. Leonov *et al.* have subsequently extended their phonon-dispersion calculations of the bcc phase to the temperature range of existence of $\delta$-Fe [Leonov *et al.*, 2014b] finding it dynamically unstable in the harmonic approximation, this result was very recently challenged by another DFT+DMFT study [Han *et al.*, 2018]. Theoretical DFT+DMFT calculations of the one-electron spectra of iron [Katsnelson and Lichtenstein, 1999, Lichtenstein *et al.*, 2001, Minár *et al.*, 2005, Grechnev *et al.*, 2007, Sánchez-Barriga *et al.*, 2009, Hausoel *et al.*, 2017, Han *et al.*, 2018] have been mostly confined to the ferromagnetic $\alpha$ phase, for which experimental angular-resolved photoemission (ARPES) spectra are available [Schäfer *et al.*, 2005, Sánchez-Barriga *et al.*, 2009]. [Katanin *et al.*, 2010] and [Igoshev *et al.*, 2013] also studied the one-electron spectral function and magnetic susceptibilities of the paramagnetic $\alpha$ and $\gamma$ phases. Overall, the most recent studies [Sánchez-Barriga *et al.*, 2009, Hausoel *et al.*, 2017, Han *et al.*, 2018] find a reasonable agreement between the theoretical **k**-resolved spectral function and experimental ARPES spectra, though discrepancies for some high-symmetry directions are still present. Hence, [Sánchez-Barriga *et al.*, 2009] concluded that a purely-local single-site DMFT self-energy is not sufficient to obtain a quantitative agreement with ARPES. Similarly, a semi-quantitative agreement with the experimental ARPES was obtained by including both local non-local many-electron effects within a weak-coupling quasiparticle GW approach [Sponza *et al.*, 2017].

Hence, a combination of non-perturbative treatment of the on-site correlations with a weak-coupling approach to non-local ones (see, e.g., [Biermann *et al.*, 2003, Tomczak *et al.*, 2017]) is probably necessary to fully account for one-electron spectra of ferromagnetic $\alpha$-Fe.

Correlation effects in iron under moderate and high pressure have been comparatively less studied with DFT+DMFT until recently. The present chapter focuses on this topic, reviewing, in particular, the results presented in our several recent papers on the subject [Glazyrin *et al.*, 2013, Pourovskii *et al.*, 2013, Pourovskii *et al.*, 2014b, Vekilova *et al.*, 2015, Pourovskii *et al.*, 2017]. First, we consider the hcp $\varepsilon$ phase, which puzzling ground-state and transport properties in the moderate pressure range of 10 to 60 GPa were shortly described above. The subsequent section deals with properties of the $\alpha$, $\gamma$ and $\varepsilon$ iron and iron-nickel alloy at the volume of 7.05 Å/atom and at temperatures up to 6000 K. These density and temperature are expected for the inner core of Earth, hence, the phase stability and transport properties of iron at such conditions are of a particular relevance to the geophysics. Though high density is expected to diminish the relative importance of potential energy, we still find a rather significant impact of the local interaction between $3d$ electrons on the electronic structure, phase stability as well as on magnetic and transport properties.

## 3.2 $\varepsilon$-Fe under moderate pressure: equation of state, resistivity and electronic topological transitions

As noted above, DFT successfully captures the magnetic state $\alpha$-Fe; DFT calculations also predict the ground-state properties of this phase in good agreement with experiment. In contrast, the same theory fails to account even for basic ground-state properties of $\varepsilon$-Fe. Within the local-spin and generalized-gradient approximations for the exchange-correlation potential it predicts a rather strong antiferromagnetism, with the iron moment of about 1.5 $\mu_B$ at the volume of 73 $(\text{a.u.})^3$/atom, corresponding to that of the $\varepsilon$-phase at the $\alpha \rightarrow \varepsilon$ transition point [Steinle-Neumann *et al.*, 2004]. No antiferromagnetic phase has been observed experimentally in $\varepsilon$-Fe down to 8 K [Cort *et al.*, 1982, Papandrew *et al.*, 2006] (though [Monza *et al.*, 2011] observed a magnetic signal in X-ray emission spectroscopy, which they ascribed to anitferromagnetic fluctuations). If the nonmagnetic ground state is imposed, DFT total energy calculations predict an equation of state that drastically disagrees with experiment. The bulk modulus is overestimated by more than 50%, and the equilibrium volume is underestimated by 10% compared to the experimental values [Steinle-Neumann *et al.*, 1999]. Another puzzling experimental observation is a large enhancement in the resistivity across the $\alpha$-$\varepsilon$ transition. The room temperature total resistivity of $\varepsilon$-Fe is twice as large as that of the $\alpha$ phase [Holmes *et al.*, 2004]. The electron-phonon-scattering contribution to resistivity calculated within GGA is in excel-

lent agreement with the experimental total resistivity for the $\alpha$ phase [Sha and Cohen, 2011], however, these calculations predict virtually no change in the resistivity across the transition to antiferromagnetic hcp-Fe. All these discrepancies between DFT calculations and experiment point out to a possible important role of dynamic correlations in $\varepsilon$-Fe.

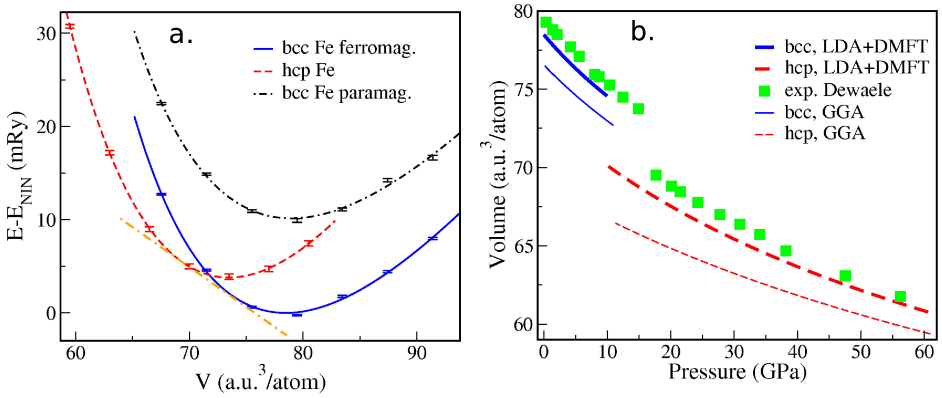


Figure 3.2: a). DFT+DMFT total energy vs. volume per atom for $\alpha$ (ferromagnetic, solid blue line, and paramagnetic, dot-dashed black line) and $\varepsilon$ (dashed red line) Fe. The error bars are the CT-QMC method stochastic error. The orange long dash-dotted straight line indicates the common tangent construction for the $\alpha - \varepsilon$ transition. b). Equations of states (EOS) for ferromagnetic $\alpha$ (low pressure) and paramagnetic $\varepsilon$ (high pressure) Fe. Theoretical results are obtained by fitting the DFT+DMFT (thick line) and GGA (thin line) total energies, respectively, using the Birch-Murnaghan EOS. The experimental EOS of iron shown by green filled squares is from [Dewaele *et al.*, 2006]. Adapted from [Pourovskii *et al.*, 2014b]

The evolution of electronic correlations across the $\alpha \rightarrow \varepsilon$ transition as well as its impact on the equation of state and electrical resistivity were studied by [Pourovskii *et al.*, 2014b] using the self-consistent DFT+DMFT approach outlined in Ch. 2; the quantum impurity problem was solved using the hybridization-expansion CT-QMC method introduced in Sec. 2.2.1. In order to achieve the necessary accuracy with a manageable computational cost the non-density-density terms in the Coulomb vertex were neglected, see Appendix A. This local Coulomb interaction vertex between Fe $3d$ states was parametrized by $U = F^0$ =4.3 eV and $J_H$=1 eV. These values of the interaction parameters were chosen on the basis of the previous cRPA calculations for iron by [Miyake *et al.*, 2009]; their value of $U$ =3.4 eV for $\alpha$-Fe was increased by about 25% to effectively account for the high-frequency tails of the Coulomb vertex [Casula *et al.*, 2012b]. The value of $J_H$ was fixed at the top of the accepted range of 0.85 to 1.0 eV to reproduce the value of magnetic moment in $\alpha$-Fe at the ambient conditions.

Overall, DFT+DMFT total energy calculations of [Pourovskii *et al.*, 2014b] provide a comprehensive and quantitatively correct picture for the ground-state properties of both phases including their ground-state volumes, bulk moduli as well as the pressure dependence of the $c/a$

ratio in $\varepsilon$-Fe. In particular, they predict a ferromagnetic $\alpha$-Fe ground state and a transition $\alpha \rightarrow \varepsilon$ phase at 10 GPa, in agreement with experiment (Fig. 3.2a). The calculated difference in total energy between the ferromagnetic and paramagnetic states of $\alpha$-Fe is of about 10 mRy (1500 K), in a good correspondence to its experimental Curie temperature of 1043 K. The Birch-Murnaghan equations of states (EOS) fitted to DFT+DMFT total energies of $\alpha$ and $\varepsilon$-Fe agree well with the corresponding experimental EOS (Fig. 3.2b). One observes a particularly significant improvement for the case of $\varepsilon$-Fe, for which the DFT-GGA framework performs quite poorly. In contrast, the DFT+DMFT corrections to EOS of ferromagnetic $\alpha$-Fe are rather small; as noted in Sec. 3.1, the DFT in conjunction with GGA already describes the ground-state properties of this phase quite well.

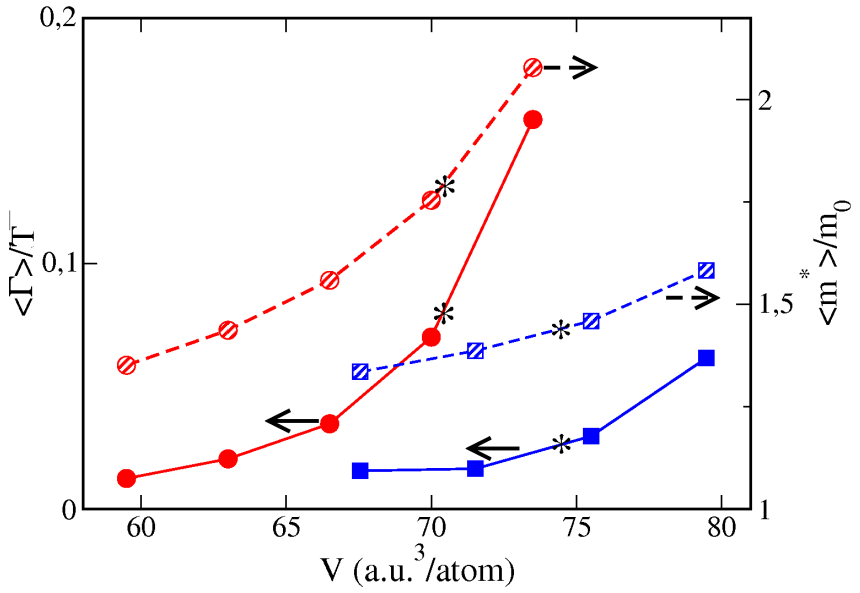


Figure 3.3: The ratio of the average inverse quasiparticle lifetime $\langle\Gamma\rangle$ to temperature (the left axis) and the average mass enhancement $\langle m^*\rangle/m_0$ (the right axis) vs. volume per atom. The solid lines (filled symbols) and dashed lines (hatched symbols) are $\langle\Gamma\rangle/T$ and $\langle m^*\rangle/m_0$, respectively. The values for $\alpha$ and $\varepsilon$ phases are shown by blue squares and red circles, respectively. The black stars indicated their corresponding atomic volumes at the transition point. Adapted from [Pourovskii *et al.*, 2014b]

The fact that many-body corrections to the ground-state properties are much more significant in the case of $\varepsilon$-Fe as compared to $\alpha$-Fe hints at stronger dynamic electronic correlations in the former. Indeed, the average mass enhancement $\langle m^*\rangle$ and the inverse quasiparticle lifetime

$$\Gamma_\alpha = -Z_\alpha \Im\Sigma_\alpha(\omega = 0), \tag{3.1}$$

where $\alpha$ is the $m$ and spin quantum numbers labeling Fe $3d$ orbitals, $Z_\alpha$ =

$[1 - d\Im\Sigma_\alpha(i\omega)/d\omega|_{\omega\to 0}]$ is the quasiparticle residue, extracted from the DMFT self-energy exhibit a large increase at the $\alpha \to \varepsilon$ transition (Fig. 3.3). This enhancement of dynamic correlations is due to the suppression of the static magnetic order at this transition. In fact, paramagnetic $\alpha$-Fe is a strongly-correlated non-Fermi-liquid system, with a particularly large value of $\Gamma$ for localized $e_g$ states [Katanin *et al.*, 2010, Pourovskii *et al.*, 2013]. In contrast, only a modest Fermi-liquid renormalization of Fe $3d$ DFT band structure is detected by ARPES for the ferromagnetic phase [Schäfer *et al.*, 2005]; their value for the mass enhancement of about 40-50% agrees reasonably with the DFT+DMFT prediction of 1.6 for $\langle m^* \rangle$ for the ambient conditions (Fig. 3.3).

A step-wise increase of the inverse quasiparticle lifetime $\Gamma$ at the $\alpha \to \varepsilon$ transition point should result in a corresponding step-wise increase of the electron-electron-scattering contribution to the electrical resistivity. Indeed, DFT+DMFT calculations for the transport presented in the same paper [1] predict such a jump with the electron-electron contribution enhanced by a factor of 3, from 0.5 $\mu\Omega$·cm in $\alpha$-Fe to 1.5 $\mu\Omega$·cm in the $\varepsilon$ phase. The jump in total resistivity $\rho$ at the transition observed experimentally [Holmes *et al.*, 2004, Yadav *et al.*, 2013] features an overall qualitative shape of the resistivity vs. pressure in iron strongly resembling the DFT+DMFT one. However, the experimental jump in $\rho$ at the $\alpha \to \varepsilon$ transition for the room temperature is an order of magnitude larger than 1 $\mu\Omega$·cm predicted by our calculations. The present approach, apparently, misses the main source of this resistivity enhancement. The fact that the resistivity jump is still well resolved at $T$ =4 K lends a strong support to its electron-electron-scattering origin. A strongly nonFL behavior of $\varepsilon$-Fe in the temperature range from 2 to (at least) 30 K, in conjunction with a non-conventional superconducting state at lower $T$ points out at important intersite correlations, e.g. spin fluctuations, which are neglected by the single-site DFT+DMFT framework. Alternatively, one may suggest that local non-density-density interaction terms neglected in [Pourovskii *et al.*, 2014b] have a crucial impact on the low-energy behavior of the self-energy $\Sigma(\omega)$ and, hence, at the transport. This problem is an interesting subject for future works.

No experimental ARPES of $\varepsilon$-Fe has been reported to date due to the obvious difficulty of performing such measurements at a high pressure of tens GPa. [Glazyrin *et al.*, 2013] studied the impact of pressure on the electronic structure of the $\varepsilon$ phase by measuring a set of quantities readily accessible at high pressure conditions, namely, the Debye sound velocity, Mössbauer central shift and hexagonal cell $c/a$ ratio, in pure Fe and in $Fe_{0.9}Ni_{0.1}$. All three quantities are found to exhibit a distinct peculiarity at about 40 GPa. One sees, for example, a clear change of slope in the evolution of $c/a$ vs. $P$ as well as a peculiarity in the Mössbauer central shift at this pressure, which is especially pronounced in the case of

[1] See Sec. 3.3.2 for a brief summary of the formalism for transport calculations

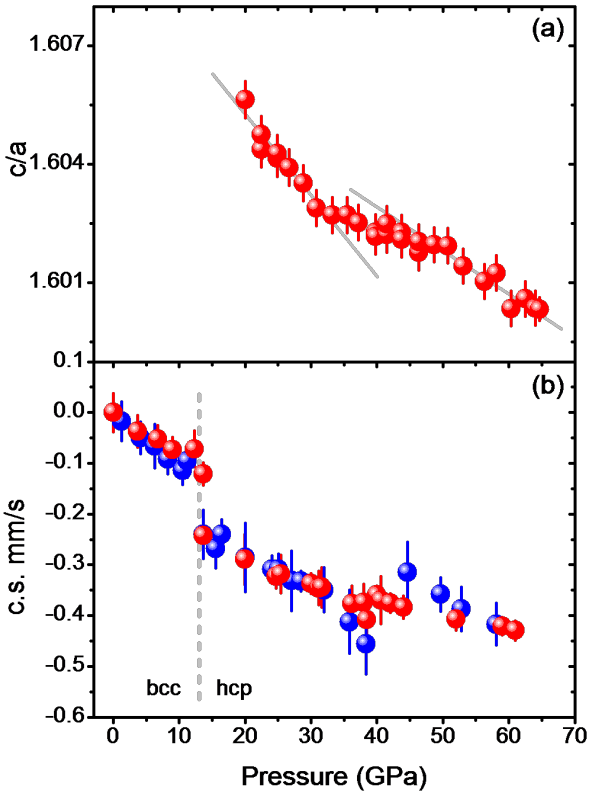


Figure 3.4: Experimental pressure dependence of (a) hcp phase $c/a$ ratio and (b) the Mössbauer centre shift based on several experimental datasets for pure iron (red circles) and for $Fe_{0.9}Ni_{0.1}$ alloy (blue circles). The centre shift values are given relative to pure $\alpha$ iron. Straight grey lines in (a) are guides for the eye. Adapted from [Glazyrin *et al.*, 2013].

$Fe_{0.9}Ni_{0.1}$ (Fig. 3.4). As discussed by [Glazyrin *et al.*, 2013] peculiarities simultaneously appearing in all three quantities can be qualitatively explained by an electronic topological transition (ETT) due to the appearance of new Fermi-surface hole pockets at a given pressure [Vaks and Trefilov, 1991, Novikov *et al.*, 1999, Katsnelson and Trefilov, 2000]. The resulting peculiarities in these quantities are proportional to the change of DOS at the Fermi level, $\delta N(E_F)$, due to the ETT.

In order to precisely identify the ETT at the origin of observed peculiarities [Glazyrin *et al.*, 2013] calculated the DFT+DMFT $\mathbf{k}$-resolved spectral function $A(\mathbf{k},\omega) = -\frac{1}{\pi}\Im G(\mathbf{k},\omega + i\delta))$ from the analytically-continued lattice GF (2.5) as a function of volume. $A(\mathbf{k},\omega)$ obtained by DFT+DMFT clearly features the emergence of new hole pockets at the $\Gamma$ and $L$ high symmetry point (Fig. 3.5a and 3.5b). The corresponding critical pressure for the ETT is found to be in the range of 40-80 GPa, depending on the chosen value of $U$. In contrast,

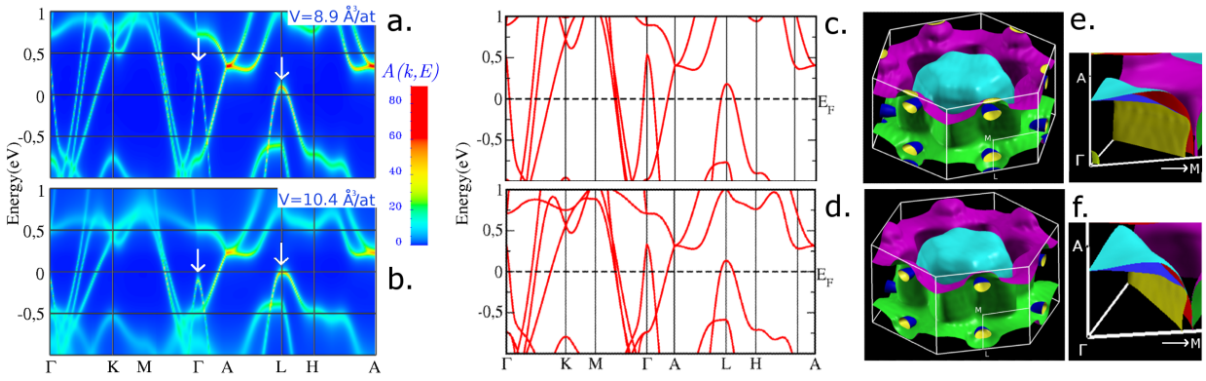


Figure 3.5: The DFT+DMFT **k**-resolved spectral function $A(\mathbf{k},\omega)$ ( in units of $V_{at}$/eV), where $V_{at}$ is the volume per atom) of $\varepsilon$-Fe at volumes $V_{at}$ of 8.9 Å$^3$/atom (a) and 10.4 Å$^3$/atom (b) corresponding to pressures of 69 and 15.4 GPa, respectively. The energy zero is taken at the Fermi level. The hole-like bands at the Γ and L points at volume 8.9 Å$^3$/atom (indicated by the white arrows) are below $E_F$ at V=10.4Å$^3$/atom. The corresponding DFT band structures are shown in c and d, respectively. The corresponding DFT+DMFT Fermi surfaces for two volumes are shown in e and f, respectively. Adapted from [Glazyrin *et al.*, 2013].

the DFT band structure features those hole pockets (Fig. 3.5d) already at 10.4 Å$^3$/at, which is the atomic volume of $\varepsilon$-Fe at the $\alpha \rightarrow \varepsilon$ transition. Hence, DFT does not predict any ETT to occur in the $\varepsilon$ phase in its experimental range of existence.

This significant shift of ETT to lower volumes/higher pressures in DFT+DMFT compared to pure DFT are mainly due to many-electron corrections to the overall position of the valence $d$ bands with respect to the $s$ ones, leading to a relative shift of states with a significant $s$ contribution with respect to the rest. A similar significant impact of many-body corrections was recently predicted even for such weakly correlated system as the osmium metal [Feng *et al.*, 2017]. They found the transition pressures for a series of ETTs to be in a better agreement with experiment when DMFT corrections were included. One may notice, however, that the relative shift of "correlated" $d$ vs. "uncorrelated" $s$ states is sensitive to the choice of the DC correction. Both [Pourovskii *et al.*, 2014b] and [Feng *et al.*, 2017] employ the "around mean-field" form of DC, which is believed to be appropriate for such relatively itinerant systems.

On the experimental side, [Dewaele and Garbarino, 2017] have very recently reported new measurements of the equation of state and $c/a$ ratio of $\varepsilon$-Fe. The experimental equation of state is found to be in good agreement with calculations of [Pourovskii *et al.*, 2014b]. Though no sign of peculiarity was observed in the $c/a$ ratio by [Dewaele and Garbarino, 2017], one may notice that the scatter of their points is significantly larger than that of [Glazyrin *et al.*, 2013].

## 3.3 Many-electron effects in iron and iron-nickel alloy at the Earth's inner core conditions

The wealth of available data on seismic wave propagation, planetary density and gravitational field, abundance of elements in the Solar system lends strong support to the hypothesis of iron being one of principal component of Earth and Earth-like planets [Birch, 1952, Dziewonski and Anderson, 1981, Lowrie, 2007]. In particular, the solid inner and liquid outer cores of Earth are believed to consist mainly of iron. The measured Earth interior density profile as well as data on the meteorite composition favor a picture of a solid Earth's inner core (EIC) composed of iron alloyed with about 10% of nickel and non-negligible quantities of light elements like Si, S, or O. Inside the EIC the matter is subjected to pressure $P$ in the range of 330 to 360 GPa at temperature $T$ of about 6000 K, though the relevant range of $T$ for the inner core is still actively debated [Boehler, 1993, Alfé *et al.*, 1999, Belonoshko *et al.*, 2000]. The temperature of solid phase inside EIC is close to its melting point. The phase stability and properties of solid iron and iron-rich alloys at such extreme conditions are of high importance for the geophysics as they represent a key input to geophysical models of Earth's core dynamics and its evolution. In particular, the interpretation of seismic data is largely based on the assumed phase diagram for relevant iron-rich alloys at the core's conditions [Tkalčić, 2015]. The models of core evolution in time are constrained by the accepted range of values for the thermal and electrical conductivities [Buffett, 2012, Pozzo *et al.*, 2012]. Therefore, significant research efforts, both experimental and theoretical, are focused on reliably determining the nature of Fe phases stable in the relevant ($P$,$T$) range and their physical properties.

Iron and its alloys at extreme conditions have been studied experimentally using the dynamical shock-wave compression and, more recently, with the static heated diamond anvil cell method. As noted in the previous section, these studies have established the stability of $\varepsilon$-Fe up to the pressure range of EIC at the room temperature [Mao *et al.*, 1990]. The situation is less clear for the high-T region, where some recent experiment [Tateno *et al.*, 2010, Tateno *et al.*, 2012, Anzellini *et al.*, 2013] found the $\varepsilon$-phase to remain stable in the relevant pressure range up to the EIC temperatures, while other studies [Dubrovinsky *et al.*, 2007, Hrubiak *et al.*, 2018] observed bcc $\alpha$-Fe to emerge at high temperatures approaching the melting point. [Tateno *et al.*, 2010] claimed to reach the EIC conditions and observed only the $\varepsilon$ phase in the studied range of $P$ from 100 GPa to the highest pressure of 377 GPa and $T$ from 2000 to 5700 K. However, their interpretation of the data was subsequently disputed by [Dubrovinsky *et al.*, 2011], who suggested that the EIC temperature was not in fact reached by [Tateno *et al.*, 2010]. Overall, currently there is no experimental consensus regarding the stable phase of Fe at EIC conditions.

The theory input is particularly valuable in such situation, hence, a number of DFT based simulations of Fe and its alloy has been published in the last two decades. These studies treated lattice vibrations in the quasi-harmonic approximation [Mikhaylushkin *et al.*, 2007, Stixrude, 2012] or with the full *ab initio* molecular dynamics approach [Vočaldo *et al.*, 2003, Godwal *et al.*, 2015, Belonoshko *et al.*, 2017]. The results of these calculations are also inconclusive, with all three known phase of iron predicted to be stable at EIC conditions by different authors. The difference in DFT free energy between those phases is found to be decreasing with increasing temperature and pressure. Thus the relative stability becomes sensitive to small differences in the calculational setup like the size of simulation supercell or the density of **k**-mesh employed in the Brillouin zone integration [Godwal *et al.*, 2015, Belonoshko *et al.*, 2017]. In particular, the non-magnetic $\alpha$ phase dynamically unstable at low temperature is claimed by [Belonoshko *et al.*, 2017] to be stabilized by an unconventional high-T diffusion mechanism; in contrast, [Godwal *et al.*, 2015] found $\alpha$-Fe to be dynamically unstable at the EIC conditions. The free-energy difference between $\gamma$ and $\varepsilon$-Fe becomes extremely small close to the melting temperature in accordance with [Mikhaylushkin *et al.*, 2007], who predicted $\gamma$-Fe to be stable at the EIC conditions, while [Stixrude, 2012] found the $\varepsilon$-phase to be more stable. In all these *ab initio* simulations the standard DFT framework in the conjunction with LDA or GGA exchange-correlation potential was employed thus neglecting dynamical correlation effects. This approximation is usually justified (see, e. g., [Stixrude, 2012]) by the fact that the local Coulomb repulsion $U$ between iron $3d$ states is smaller than the effective $3d$ bandwidth, especially at high pressure. Though this statement is correct even at the ambient pressure, this does not mean that correlation effects in iron are negligible. As noted in the previous section, the strength of local many-electron effects in iron is much more sensitive to the Hund's rule coupling $J_H$, which is expected to be quite insensitive to pressure. High temperature stabilizing high-entropy states may strengthen the tendency towards a nonFL behavior or the formation of local magneitc moments. Hence, the role of many-electron effects needs to be evaluated with explicit calculations.

This problem was addressed in [Pourovskii *et al.*, 2013] by DFT+DMFT calculations for the all three phases, $\alpha$, $\gamma$ and $\varepsilon$, for the volume of 7.05 Å/atom, corresponding to the density of EIC, and for temperatures up to 5800 K by employing the same self-consistent in the charge density full-potential DFT+DMFT framework as in the studies of $\varepsilon$-Fe described in the previous section. This work evaluated the impact of many-electron effects on the electronic structure, magnetic susceptibility and relative stability of the three Fe phases. All DFT+DMFT calculations were done for the corresponding perfect fixed lattices. The lattice vibrations play a paramount role at the extreme temperatures inside the EIC, but including their effect within a kind of DFT+DMFT-based molecular dynamics is prohibitively costly at present. The fixed-lattice cal-

culations of [Pourovskii *et al.*, 2013], however, allowed evaluating the structural dependence of correlation effects, assessing (though quite roughly) their impact on the electronic free energy "landscape" in the structural coordinates. A subsequent work of [Vekilova *et al.*, 2015] carried out similar calculations for Fe-rich FeNi alloys in order to assess the impact of Ni substitution on many-electron effects. A later study [Pourovskii *et al.*, 2017] concentrated on the $\varepsilon$-phase evaluating its electronic state as well as electrical and thermal conductivities. The results obtained in these works for the electronic structure, magnetism, thermodynamic stability and transport are reviewed below together with relevant calculations of other authors.

### 3.3.1 Electronic structure and magnetic susceptibility of iron and iron-nickel alloys

The ratio $\Gamma/T$ (see eq. 3.1) calculated at the EIC atomic volume as a function of $T$ in [Pourovskii *et al.*, 2013] is shown in Fig. 3.6 for all relevant irreducible representations of the three phases. One may readily notice a qualitative difference in the behavior of $\Gamma$ between these phases. The temperature scaling $\Gamma/T \propto T$ expected in the case of a good FL is clearly observed for the $\varepsilon$-phase. In contrast, $\Gamma/T$ for the bcc iron $e_g$ states features a linear and steep rise for $T < 1000$ K and then behaves non-linearly, indicating a non-coherent nature of those states at high temperatures. The bcc Fe $t_{2g}$ and fcc Fe $e_g$ electrons are in an intermediate situation with

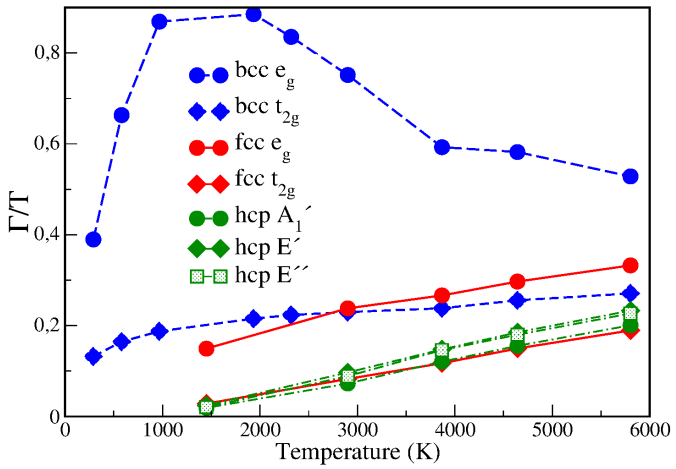


Figure 3.6: The ratio of the inverse quasiparticle lifetime $\Gamma$ to temperature $T$ vs. $T$. The solid red, dashed blue and dash-dotted green curves correspond to 3d states in fcc, bcc, and hcp Fe, respectively. They are split by the crystal field into $t_{2g}$ (diamonds) and $e_g$ (circles) representations in the cubic (bcc and fcc) phases, and two doubly-degenerate ($E'$ and $E''$, shown by diamonds and squares, respectively) and one singlet ($A_1'$, circles) representations in the hcp phase, respectively . A non-linear behavior of $\Gamma$/T for bcc Fe $e_g$ states is clearly seen. Adapted from [Pourovskii *et al.*, 2013].

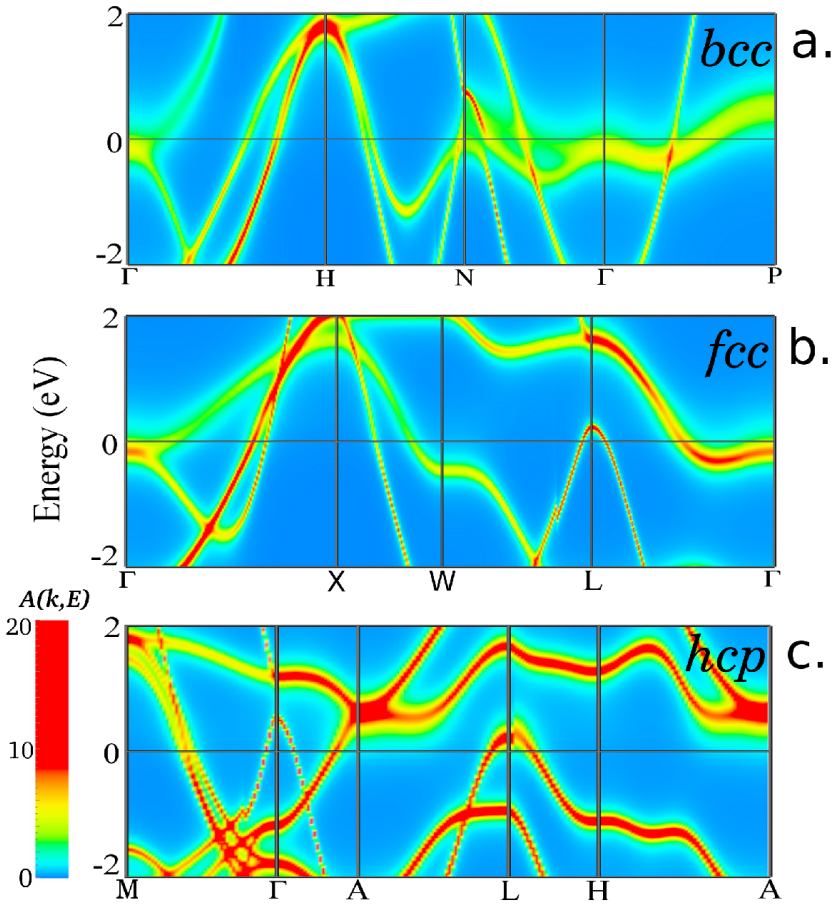


Figure 3.7: The DFT+DMFT **k**-resolved spectral function $A(\mathbf{k},\omega)$ (in $V_{atom}$/eV) for bcc (a), fcc (b), and hcp (c) Fe at volume $V_{at}$ =7.05 Å$^3$/atom and temperature 5800 K. A non-quasiparticle $e_g$ band is seen in the vicinity of the Fermy energy along the $N-\Gamma-P$ path in (a). Adapted from [Pourovskii *et al.*, 2013].

some noticeable deviations from the FL behavior.

The same conclusions can be drawn from the **k**-resolved spectral function $A(\mathbf{k},\omega)$ plotted in Fig. 3.7 for the temperature of 5800 K. The bcc phase features a low-energy $e_g$ band along the $N-\Gamma-P$ path that is strongly broadened, thus indicating destruction of quasiparticle states. The non-FL behavior of $e_g$ states in $\alpha$-Fe is explained by the narrow peak in its partial density of states (PDOS) induced by a van Hove singularity in the vicinity of $E_F$. Such narrow peak in PDOS located at $E_F$ leads to suppression of the low-energy hopping and to the corresponding enhancement of correlations[Mravlje *et al.*, 2011]. In hcp Fe the electronic states in the vicinity of $E_F$ are sharp (their red color indicating high value of $A(\mathbf{k},\omega)$), hence $\varepsilon$−Fe exhibits a typical behaviour of a FL with large quasi-particle life-times in the vicinity of $E_F$. $\gamma$-Fe is in an intermediate state, with some broadening noticeable in the $e_g$ bands at $E_F$ in the vicinity of

the $\Gamma$ and $W$ points.

The conclusion of [Pourovskii *et al.*, 2013] on the FL nature of $\varepsilon$-Fe was subsequently challenged by [Zhang *et al.*, 2015], who recalculated $\varepsilon$-Fe at the EIC volume within DFT+DMFT [2] and found a strongly non-FL linear dependence of $\Gamma$ vs. $T$. In contrast to [Pourovskii *et al.*, 2013] employing the density-density approximation to the local Coulomb vertex defined by $U$ =3.4 eV and $J_H$ =0.94 eV, [Zhang *et al.*, 2015] used the full rotationally-invariant form for the vertex parametrized by a higher value of $U$ = 5 eV and almost the same $J_H$. Therefore, in order to convincingly establish the nature of electronic state in $\varepsilon$-Fe [Pourovskii *et al.*, 2017] performed new DFT+DMFT calculations for the $\varepsilon$-phase with the full rotationally-invariant Coulomb interaction and explored the range of $U$ from 4 to 6 eV. These calculations predicted almost perfect quadratic FL temperature scaling of $\Gamma$.

A significant problem in the analysis of DFT+DMFT results carried out in [Pourovskii *et al.*, 2013, Zhang *et al.*, 2015] stems from the fact that the DMFT self-energy is calculated by CT-QMC on imaginary-frequency Matsubara points. The analytical continuation needed to obtain real-frequency data from this imaginary-frequency self-energy $\Sigma(i\omega)$ is known to be a mathematically ill-defined problem and quite sensitive to the details of its implementation. Even the extrapolation of $\Sigma(i\omega)$ to $\omega$ =0 needed to evaluate $\Gamma$, eq. 3.1, becomes rather less reliable for high temperatures, where the first Matsubara point $\omega_1 = i\pi k_B T$ is significantly shifted away from the real axis.

Hence, [Pourovskii *et al.*, 2017] also assessed the FL nature of $\varepsilon$-Fe by analyzing the imaginary-frequency self-energy without resorting to any analytical continuation. This is done by employing the so-called "first-Matsubara-frequency" rule. As demonstrated, e. g., by [Chubukov and Maslov, 2012], in a Fermi liquid the imaginary part of electronic self-energy at the first Matsubara point within a local approximation like DMFT must be proportional to the temperature, i.e. $Im[\Sigma(i\pi k_B T)] = \lambda T$, where $\lambda$ is a real constant. In Fig. 3.8a $Im[\Sigma(i\pi k_B T)]$ is plotted as a function of temperature for all inequivalent orbitals in hcp and bcc Fe. One clearly sees that in the $\varepsilon$ phase $Im[\Sigma(i\pi k_B T)]$ is almost perfectly proportional to $T$, in contrast to bcc Fe, where it exhibits significant deviations from the "first-Matsubara-frequency" rule. This deviation is especially pronounced for the $e_g$ states of the bcc phase, which are indeed of a strongly non-FL nature, as discussed above.

[Pourovskii *et al.*, 2017] also verified the scaling of the full analytically-continued DMFT self-energy , which in a FL state exhibits the quadratic frequency dependence at low $\omega$ with $\Sigma(\omega) = C \cdot (\omega^2 + (\pi k_B T)^2)$. The constant of proportionality $C$ can be written as $1/(Z\pi k_B T_0)$ with the characteristic scale $T_0 \sim 10 T_{FL}$, where $T_{FL}$ is the temperature where resistivity ceases to

[2] [Zhang *et al.*, 2015] was subsequently retracted by the authors ([Zhang *et al.*, 2016]) due to a numerical mistake in their transport calculations. However, this retraction does not concern their conclusions on a non-FL nature of $\varepsilon$-Fe at the EIC conditions.

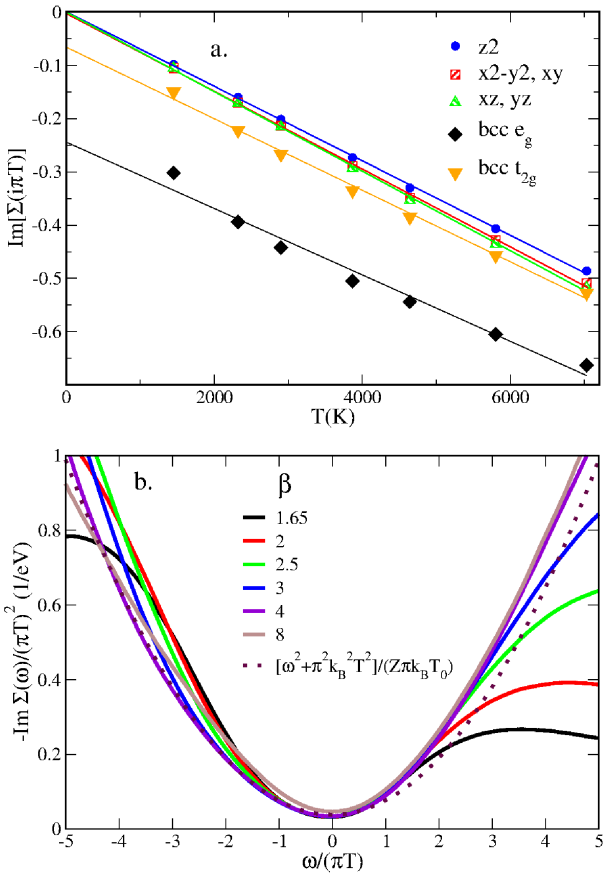


Figure 3.8: Fermi-liquid scaling of the DMFT self-energy in $\varepsilon$-Fe. a. The imaginary part of the DMFT self-energy at the first Matsubara point $\omega_1 = i\pi k_B T$ vs. temperature for hcp and bcc Fe. Note that $Im[\Sigma(i\pi k_B T)]$ being proportional to T is a signature of a Fermi-liquid [Chubukov and Maslov, 2012] . The lines are the linear regression fits to the calculated points for corresponding $3d$ orbitals of Fe. b. The rescaled imaginary part of the DMFT self-energy at the real axis $Im[\Sigma(\omega)]/(\pi k_B T)^2$ vs. $\omega/(\pi k_B T)$. One sees that all self-energies collapse into a single curve described by a parabolic fit (the dotted line) defined by the quasiparticle weight $Z$ =0.7 and the characteristic Fermi-liquid temperature scale $T_0$ =12 eV. Adapted from [Pourovskii *et al.*, 2017].

follow a strict $T^2$ temperature dependence [Berthod *et al.*, 2013]. Indeed, one sees in Fig. 3.8b that the real-frequency self-energies for different temperatures collapse into a single curve when plotted as $Im[\Sigma(\omega)]/(\pi k_B T)^2$ vs. $\omega/(\pi k_B T)$. The value of $k_B T_0 = 12$ eV extracted from this plot corresponds to a $T_{FL} \approx$14000 K, which is significantly higher than the range of temperatures expected inside the EIC. This analysis of both the Matsubara and real-ferquency self energy of $\varepsilon$-Fe has thus convincingly confirmed its FL state. We will see in Sec. 3.3.2 that this results has a direct bearing on the transport properties of $\varepsilon$-Fe at the EIC conditions.

The temperature dependence of uniform susceptibility $\chi$ was also calculated

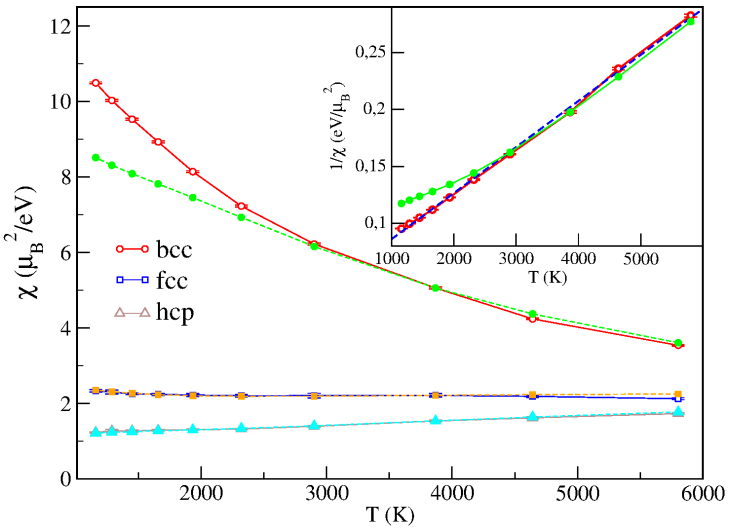


Figure 3.9: The uniform magnetic susceptibility in paramagnetic state versus temperature. The error bars are due to the CT-QMC stochastic error. The dashed lines with corresponding filled symbols are fits to the enhanced Pauli law, see the text. Inset: the inverse uniform magnetic suscptibility of bcc Fe is shown in red (empty circles), the blue dot-dashed and green (filled circles) lines are fits to the Curie-Weiss and enhanced Pauli law, respectively. Adapted from [Pourovskii *et al.*, 2013].

[Pourovskii *et al.*, 2013] by evaluating the response to a small external field. The obtained temperature dependence (see Fig. 3.9) is consistent with the results on electronic structure discussed above. A Pauli behavior found for the FL $\varepsilon$ and $\gamma$ phases, while the non-FL bcc $\alpha$ exhibits a Curie-Weiss behavior well described by the fit $\chi = \frac{1}{3}\frac{\mu_{eff}^2}{T+\Theta}$ with $\mu_{eff}$ =2.6 $\mu_B$ and $\Theta$ =1396 $K$ (see inset in Fig. 3.9). Alternatively, one may try to account for the same dependence with an enhanced Pauli law, $\chi = \chi_0/(1 - I * \chi_0)$, where $I$ is the Stoner parameter and the strong temperature dependence of $\chi$ stems from a narrow peak at $E_F$ in the $e_g$ PDOS due to the van Hove singularity. However, the enhanced Pauli-law fit describes the behavior of $\chi$ less well than the Curie-Weiss one, the difference is clear for lower $T$ <3 below 2500 K. Hence, from these calculations one may infer the existence of a rather large local magnetic moment in the bcc phase at the EIC conditions. One may expect a significant contribution to the $\alpha$-phase free energy due to the corresponding magnetic entropy.

The EIC is expected to contain, apart of iron, also non-negligible contributions of other transition metals, mainly of nickel as evidenced by the composition of metallic meteorites. The contribution of nickel is evaluated to 5-10% based on geochemical models [McDonough and s. Sun, 1995] The impact of Ni substitution on many-electron effects in iron at the EIC conditions is hence an important subject and has been studied by [Vekilova *et al.*, 2015, Hausoel *et al.*, 2017]. In particular, [Vekilova *et al.*, 2015] employed

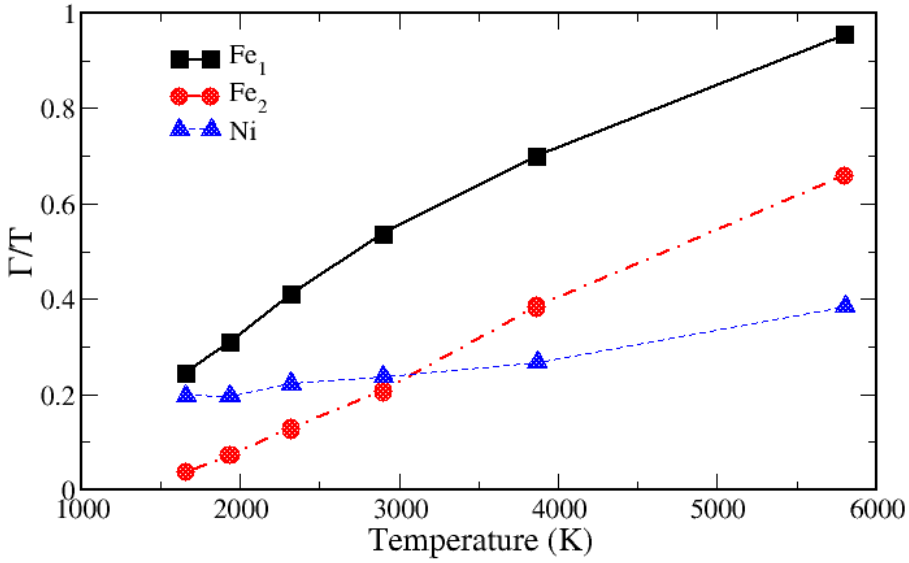


Figure 3.10: The inverse quasiparticle lifetime Γ as a function of $T$ for three inequivalent sites, $Fe_1$ (six Ni and six Fe nearest neighbors) , $Fe_2$ (all nearest neighbors are Fe) and Ni, in the hcp $Fe_3Ni$ supercell.

the same computational framework as [Pourovskii *et al.*, 2013] and modeled the random $Fe_3Ni$ alloy by the smallest supercells capable to accommodate 25% of Ni substitution. These supercells comprise two, one, and two conventional cells in the case of bcc, fcc, and hcp lattices, respectively. In order to model more realistic lower Ni concentrations one would have to employ larger supercells with the corresponding heavy increase in the computational effort. In addition, [Vekilova *et al.*, 2015] made use of different environment of two inequivalent Fe sites in their bcc and hcp supercells , with only one of those having Ni nearest neighbors, to evaluate the effect of Ni nearest neighbors on correlations on iron sites. Many-electron effects on Ni were included in the same way as for Fe with the corresponding local Coulomb interaction specified by the same values of $U = 3.4$ eV and $J_H = 0.9$ eV.

The effect of Ni nearest neighbors (NN) on electronic correlations on Fe sites was found to be structure-dependent. In the bcc phase it results in significant deviations from the Curie-Weiss behavior for the uniform susceptibility $\chi$ and reduced Γ for the $e_g$ states. Overall the presence of Ni NNs reduced the degree of "non-Fermi-liquidness" for the bcc $e_g$ states. The opposite effect was found for the hcp phase, where the presence of Ni NNs enhanced the uniform susceptibility and Γ (Fig. 3.10). These effects can be related to modifications of corresponding Fe PDOS due to the presence of Ni NNs. Namely, in the case of bcc one observes a smearing of the $e_g$ peak at $E_F$, conversely, in the case of $\varepsilon$-Fe a characteristic dip in PDOS in the vicinity of $E_F$ becomes

more shallow.

[Vekilova *et al.*, 2015] found rather weak correlation effects on Ni sites at the EIC conditions. As shown in Fig. 3.10, Γ for Ni features a non-FL behavior with a rather slow increase in the studied range of $T$.

Many-electron effects in Ni and FeNi alloys under extreme conditions were subsequently studied in a recent work by [Hausoel *et al.*, 2017]. The authors used a DFT+DMFT technique that is similar to the one used in [Pourovskii *et al.*, 2013, Vekilova *et al.*, 2015] and mainly focused on non-FL properties of Ni $t_{2g}$ states, this question was not addressed by [Vekilova *et al.*, 2015]. They modeled random $Fe_{1-x}Ni_x$ alloys ($x$ =0.05, 0.20) at the EIC density within the coherent-potential approximation (CPA). The advantage of CPA is that one can treat any concentration $x$ with the same computational cost, however, the local environment effects, which seems to be quite important as one sees in Fig. 3.10, are neglected. [Hausoel *et al.*, 2017] predicted a strong enhancement of Γ due to the Ni substitution as compared to pure $\varepsilon$-Fe for the studied range of temperatures up to 2000 K. This result is in agreement with Fig. 3.10, if one compares the magnitude of Γ for the iron site $Fe_2$ without Ni NNs with that for Ni at $T$ <2000 K. However, one also sees that Γ of Ni exhibits a slow almost linear-in-T scaling, while Γ of $Fe_2$ scales quadratically with $T$, hence at the EIC temperature of about 6000 K the scattering due to the iron sites dominates and the Ni contribution is relatively weaker.

### 3.3.2 Electron-electron scattering and transport in $\varepsilon$-Fe

Transport properties of iron at the extreme conditions are of significant importance for geophysics. In particular, the thermal conductivity of the iron-rich matter inside the liquid outer core of Earth is a key parameter determining the stability of the geodynamo generating the Earth' magnetic field. This geodynamo runs on heat from the growing solid inner core and on chemical convection provided by light elements issued from the liquid outer core on solidification [Pozzo *et al.*, 2012]. The power supplied to drive the geodynamo is proportional to the rate of inner core growth, which in turn is controlled by heat flow at the core-mantle boundary [Lay *et al.*, 2008]. It is this heat flow that critically depends on the thermal conductivity of liquid iron under the extreme pressure and temperature conditions in the Earth's core. For a long time there has been agreement that convection in the liquid outer core provides most of the energy for the geodynamo and has been doing so for at least 3.4 billion years [Olson, 2013, Stacey and Loper, 2007]. Recently, such a view has been challenged by first-principles calculations [de Koker *et al.*, 2012, Pozzo *et al.*, 2012], suggesting a much higher capacity for the liquid core to transport heat by conduction and therefore less ability to transport heat by convection [Olson, 2013]. The calculated conductivities have been found to be two to three times higher than the earlier generally accepted estimates, urging for reassessment

of the core thermal history and power requirements [Pozzo *et al.*, 2012].

Convection also plays a crucial role in the current theory of the EIC dynamics, as a radial motion of the inner core matter is invoked to explain the observed seismic anisotropies of the inner core [Romanowicz *et al.*, 1996, Buffett, 2009, Monnereau *et al.*, 2010]. However, *ab initio* calculations of [Pozzo *et al.*, 2014] similarly predict a too high thermal conductivity for hexagonal close-packed (hcp) $\varepsilon$-iron to sustain this convection.

The first-principles calculations for liquid and solid iron of [de Koker *et al.*, 2012, Pozzo *et al.*, 2012, Pozzo *et al.*, 2014] employed the standard density-functional-theory (DFT) framework in which electron-electron repulsion is not properly accounted for as dynamical many-body effects are neglected. Hence, the contribution to resistivity from the electron-electron scattering (EES) of $d$-electrons due to correlations was not taken into account in those calculations. In order to elucidate how large the EES contribution to the electrical and thermal resistivity at Earth's core conditions [Pourovskii *et al.*, 2017] extended their DFT+DMFT approach to calculations of the electrical and thermal conductivities of pure $\varepsilon$-Fe at the EIC density. Using the analytically-continued DMFT self-energy (see Fig. 3.8b) they evaluated the conductivity from the corresponding DFT+DMFT spectral function using the Kubo linear-response formalism described in [Kotliar *et al.*, 2006, Aichhorn *et al.*, 2016]. Namely, the electrical and thermal conductivity read

$$\sigma_{\alpha\alpha'} = \frac{e^2}{k_B T} K^0_{\alpha\alpha'}, \tag{3.2}$$

$$\kappa_{\alpha\alpha'} = k_B \left[ K^2_{\alpha\alpha'} - \frac{(K^1_{\alpha\alpha'})^2}{K^0_{\alpha\alpha'}} \right], \tag{3.3}$$

where $\alpha$ is the direction ($x$, $y$, or $z$), $k_B$ is the Boltzmann constant. The kinetic coefficients $K^n_{\alpha\alpha'}$ can be calculated from the real-energy DFT+DMFT spectral function $A(\mathbf{k},\omega)$ and the velocities of Kohn-Sham states, $v_\alpha(\mathbf{k})$, the later is evaluated by DFT band structure methods as described, e. g., in [Ambrosch-Draxl and Sofo, 2006] for the case of LAPW method.

The contributions of electron-electron scattering into the electrical resistivity and thermal conductivity of $\varepsilon$-Fe obtained by [Pourovskii *et al.*, 2017] are displayed as a function of $T$ in Figs. 3.11a and 3.11b, respectively. First, one sees that the electrical resistivity $\rho$ features a clear $T^2$ FL dependence, as expected on the basis of the analysis of its DMFT self-energy as discussed in Sec. 3.3.1. Second, its magnitude of $1.6\cdot 10^{-5}$ $\Omega$·cm at $T$ =5800 K is rather insignificant compared to the electron-phonon-scattering contribution of about $5.3\cdot 10^{-5}$ $\Omega$·cm predicted by DFT calculations of [Pozzo *et al.*, 2014]. This indicates that the electron-electron scattering should not strongly influence the electrical resistivity in hcp-Fe at Earth's core conditions. Third, the electron-electron-scattering thermal conductivity $\kappa_{e-e}$ of 540 $\mathrm{Wm^{-1}K^{-1}}$ $T$ =5800 K

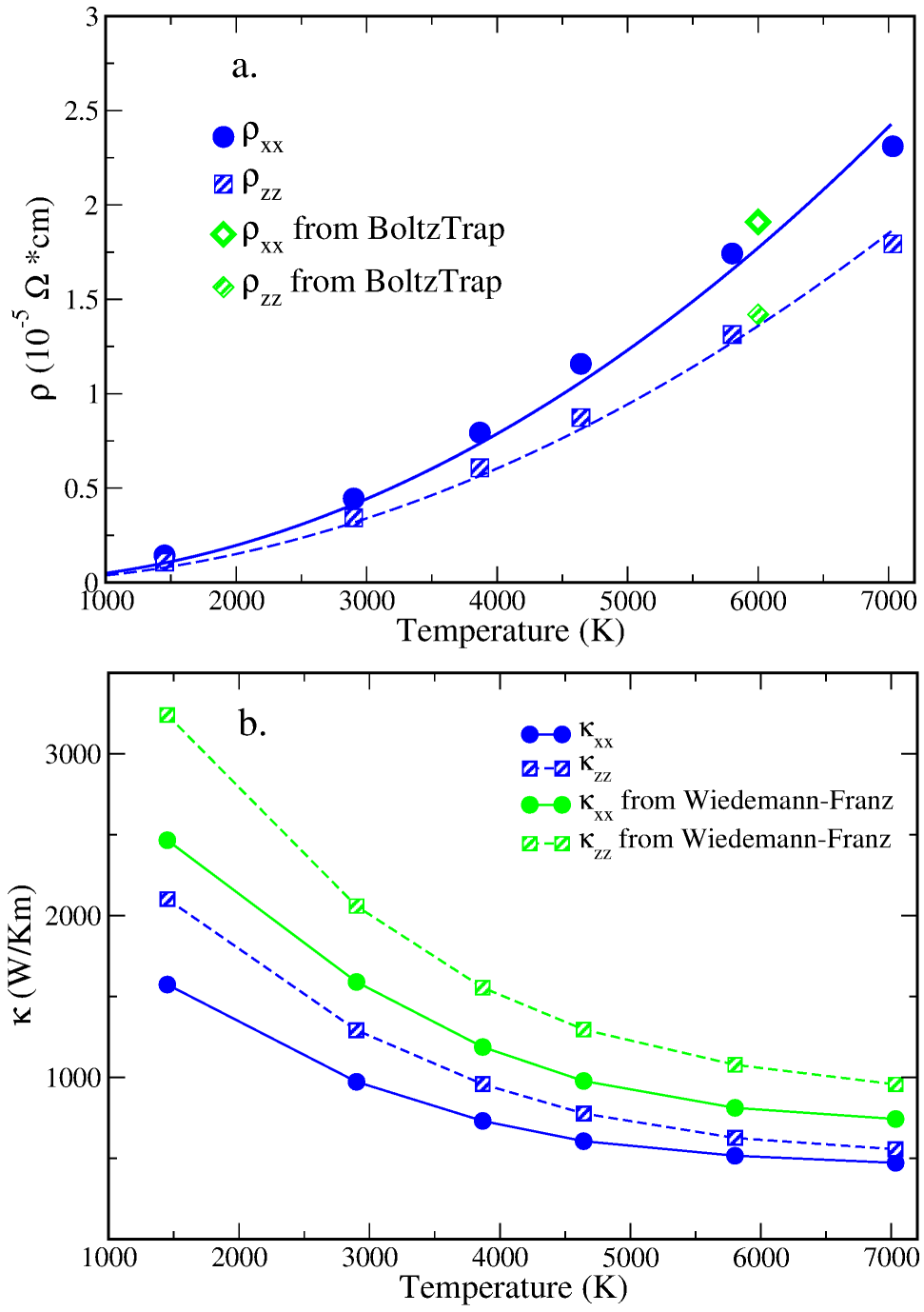


Figure 3.11: Calculated electron-electron-scattering contribution to the electrical and thermal resistivity of hcp iron at Earth's core density. a. Electrical resistivity. Blue filled circles and hashed squares are DFT+DMFT results for $\rho_{xx}$ and $\rho_{zz}$ , respectively. Green empty and hashed diamonds are the corresponding resistivities calculated by the Boltzmann-transport code BoltzTrap [Madsen and Singh, 2006] assuming a Fermi-liquid with the scattering rate $\Gamma/Z$ =0.09 eV. b. Thermal conductivity. Blue filled circles and hashed squares are DFT+DMFT results for $\kappa_{xx}$ and $\kappa_{zz}$, respectively. Green lines/symbols are the corresponding conductivities obtained from the calculated electrical conductivity using the Wiedemann-Franz law with the standard Lorenz number of $2.44{\cdot}10^{-8}$ W$\Omega$K$^{-2}$. Adapted from [Pourovskii *et al.*, 2017].

is not high and comparable to the corresponding value due to the electron-phonon scattering $\kappa_{e-ph}$ ≈300 $\mathrm{Wm^{-1}K^{-1}}$ obtained by [Pozzo *et al.*, 2014]. Hence, in contrast to $\rho$ the electron-electron scattering contribution to the thermal conductivity is quite important. By including both the electron-electron and electron-phonon scattering effects the total conductivity is reduced to about 190 $\mathrm{Wm^{-1}K^{-1}}$, hence, the corresponding resistivity is enhanced by about 60%.

An important observation of [Pourovskii *et al.*, 2017] is that the DFT+DMFT electron-electron-scattering thermal conductivity of $\varepsilon$-Fe is significantly lower than the one calculated from the corresponding contribution to $\rho = 1/\sigma$ in accordance with the Wiedemann-Franz law, $\kappa/(\sigma T) = \frac{\pi^2}{3}\left(\frac{k_B}{e}\right)^2 = L_0$ (where the standard Lorenz number $L_0$ is $2.44{\cdot}10^{-8}\mathrm{W\Omega K^{-2}}$), see Fig. 3.11b. By employing simple analytical calculations in the Boltzmann formalism [Herring, 1967] showed that the quadratic FL frequency dependence of the imaginary part of the self-energy and, hence, of the quasiparticle life-time

$$1/\tau(\varepsilon) = 1/\tau(\varepsilon = 0) \cdot \left(1 + \varepsilon^2/(\pi k_B T)^2\right),$$

leads to a substantial reduction of the Lorenz number

$$\kappa/(\sigma T) = L_0/1.54 = L_{FL}.$$

The stronger effect of the frequency-dependence of $\tau(\omega)$ on the thermal conductivity as compared to $\sigma$ is due to the additional power $\varepsilon^2$ in the numerator of the transport integrals for $\kappa$, see [Ashcroft and Mermin, 1976]. Hence, the enhancement of the electron-electron-scattering contribution to the thermal resistivity obtained within DFT+DMFT stems directly from the Fermi-liquid state of the $\varepsilon$-Fe phase at the EIC conditions.

The reduction of the thermal conductivity due to the electron-electron scattering predicted by [Pourovskii *et al.*, 2017] is still insufficient to explain the stability of convection by itself. On the other hand, the extremely low values of $\kappa_{tot}$ ∼50 $\mathrm{Wm^{-1}K^{-1}}$ may not be required to reconcile theoretical calculations of the thermal conductivity with geophysical observations [O'Rourke and Stevenson, 2016, Hirose *et al.*, 2017].

Moreover, the impact of alloying and lattice vibrations have not been to date taken into account in the DFT+DMFT transport calculations. For example, the DFT+DMFT calculations for Fe-Ni alloy at the inner core conditions discussed in the previous section point out at an important local environment effects that may affect the electron-electron scattering in real material of the EIC. The impact of all those effects on transport properties of the EIC matter remains to be evaluated.

### 3.3.3 Many-electron effects and structural stability

The stable phase of pure iron at the EIC conditions has not been clearly identified experimentally; neither have *ab initio* DFT calculations resulted in an unambiguous prediction due to a small energy difference between the three phases, as described in the introduction of Sec. 3.3. Hence, corrections due to the many-electron effects neglected by DFT can have a qualitative impact on the nature of stable iron phase at the EIC conditions.

A quantitative estimation for the contribution of correlations to the electronic free energy of the three phases was obtained by [Pourovskii *et al.*, 2013] together with their other magnetic and electronic properties (see Sec. 3.3.1). Their fixed-lattice calculations neglected the contribution of lattice vibrations to the phase stability, which are expected to be very significant at such extreme temperatures. However, such calculations are still able to assess the structural dependence of this contribution.

In spite of the simplifying fixed-lattice approximation evaluating the electronic free energy within the DFT+DMFT framework remains a highly non-trivial task. The total-energy calculations in this framework have nowadays become quite standard as described in Sec. 2.3. Such DFT+DMFT calculations evaluating the total energy using eq. 2.13 have been applied, for example, by Leonov *el al.* [Leonov *et al.*, 2011] to study the $\alpha$-$\gamma$ phase transition in iron.

In contrast, the partition function and, correspondingly, free energy cannot be generally directly sampled by the usual Metropolis algorithm. In the context of DMFT quantum impurity problem solved by CT-QMC or other numerical technique, it is the contribution of DMFT functional $\Phi_{imp}[G_{loc}(\mathbf{R})]$ into (**??**), which is the sum of all local skeleton diagrams constructed with the local GF $G_{loc}(i\omega_n)$ and the on-site vertex, that cannot be computed directly. Different types of the numerical thermodynamic integration are employed instead, in particular, the one from an analytical high-temperature limit [Haule and Birol, 2015]. Such integration remains non-trivial in the present case of Fe at the EIC conditions, as the temperature $T$ ≈6000 K is still low compared to other energy scales like the bandwidth or $U$. [Pourovskii *et al.*, 2013] employed instead the numerical thermodynamic integration over the coupling strength $\lambda \in [0:1]$, where the corresponding free energy is defined $F_\lambda = -\frac{1}{\beta}\ln \mathrm{Tr}\left(\exp[-\beta(\hat{H}_0 + \lambda \hat{H}_{int})]\right)$, $H_0$ is the one-electron part of the DFT+U Hamiltonian (2.1), $\hat{H}_{int} = \hat{H}_U - E_{DC}$ is the interacting part. The coupling constant integration results in the following expression for the many-body correction:

$$\Delta F = F - F_{DFT} = \int_0^1 \frac{\langle \lambda \hat{H}_{int} \rangle_\lambda}{\lambda} d\lambda, \tag{3.4}$$

where $F_{DFT}$ is the electronic free energy in DFT. In derivation of Eq. 3.4 one neglects the $\lambda$ dependence of the one-electron part, and, hence, the charge density renormalization due to

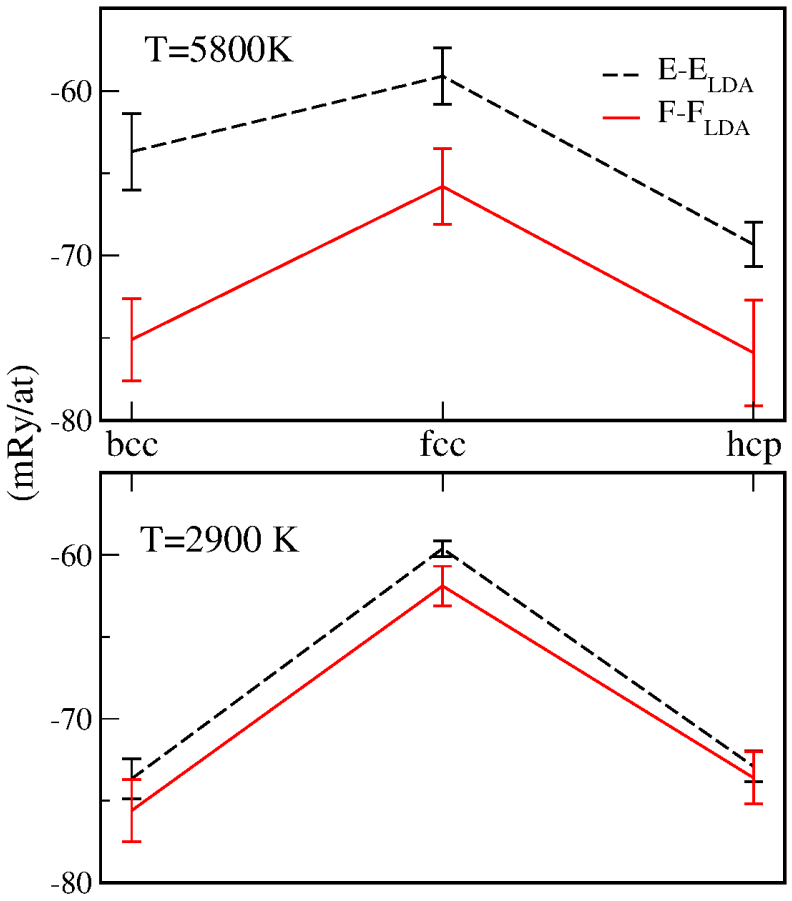


Figure 3.12: Many-body correction to the total (black dashed line) and free (red solid line) energy for the three phases of Fe at the volume of 7.05 Å/atom at T=5800 K (upper panel) and 2900 K (lower panel). The error bars are due to the CT-QMC stochastic error. Adapted from [Pourovskii *et al.*, 2013].

many-body effects. In practice, the integrand in (3.4) was evaluated numerically with $\frac{\langle\lambda\hat{H}_{int}\rangle_\lambda}{\lambda}$ computed for a discrete mesh in $\lambda \in [0:1]$ by performing DFT+DMFT simulations with the Coulomb interaction scaled accordingly. This method was subsequently applied in DFT+DMFT calculations of [Bieder and Amadon, 2014] to evaluate the free energy of the cerium metal.

The resulting DMFT correction to the free energy for the three phases is plotted in Fig. 3.12 togehter with the correction to the total energy calculated given by the difference of (2.13) and $E_{DFT}$. Within rather significant error bars the magnitude of $\Delta F$ is the same for bcc and hcp Fe, which are suggested as stable phases of iron [Vočaldo *et al.*, 2003] and iron-based alloys [Lin *et al.*, 2002, Dubrovinsky *et al.*, 2007] at the Earth's inner core conditions. Though the correlation strength (as measured, for example, by the inverse quasiparticle lifetime $\Gamma$, Fig. 3.6), is higher for $\alpha$-Fe, this is apparently compensated by a higher value of $U$ predicted for the $\varepsilon$-

phase by cRPA calculations of the same work [Pourovskii *et al.*, 2013]. The magnitude of $\Delta F$ is, however, at least several mRy smaller in the case of fcc Fe, showing that the many-body correction may significantly affect relative energy differences among iron phases at the Earth core conditions. One may also notice that the entropic contribution $T\Delta S = \Delta E - \Delta F$ becomes much more significant at the higher temperature, and its contribution is almost twice larger in the case of the bcc phase compared with two others. This is in agreement with the local-moment behavior of this phase predicted by DFT+DMFT calculations, as described in Sec. 3.3.

Chapter 4

# Localized systems in quasi-atomic approximation: multiplets, crystal field and inter-site exchange interactions

Contents



## 4.1 Introduction

A very wide range of crystalline materials exhibits a particular behavior stemming from degrees of freedom due to localized partially-filled $d$ ($f$-electron) shells on transition-metal (rare-earth) ions. In such compounds charge fluctuations are suppressed due to a large value of the on-site Coulomb repulsion as compared to the bare bandwidth $W$ of the relevant $d$ (or $f$) band, $W \ll U$. The corresponding degrees of freedom are hence due to spin, orbital or high-order multipolar moments for a given ground-state shell occupancy. Experimentally this behavior will be generally associated with a Curie response to an external magnetic field at high temperatures and the corresponding contribution to the system's entropy. High temperatures here are defined in comparison to the temperature scale $T_o$ at which the local moments will order due to an inter-site coupling generated as a low-order perturbative term

in $W/U$. The most important mechanisms for such ordering are the superexchange (SE) in correlated insulators [Anderson, 1950] and Ruderman-Kittel-Kasuya-Yosida (RKKY) coupling [Ruderman and Kittel, 1954, Kasuya, 1956, Yosida, 1957] in metals. The condition $W \ll U$ is rather loose in the later metallic case, as the Kondo screening of local moments (see, e.g., [Hewson, 1993, Coleman, 2002] for review) characterized by the scale $T_K$ may become larger than the energy gain due to the local spin ordering. Below $T_K$ the hybridization between localized and conduction states is well know to give rise to a partial delocalization of the former resulting in the formation of strongly renormalized quasiparticle bands in the vicinity of the Fermi level. The Kondo scale is given by $T_K \propto \exp(-1/J_K\rho_F)$, where $J_K \propto V^2/U$ is the on-site antiferromagnetic coupling between the localized and conduction electron spins, $\rho_F$ is the conduction-electron density of states at $E_F$, and $V$ is the on-site hybridization matrix element between the localized and conduction states. The energy gain due to a magnetic order induced by RKKY interactions can be shown to be $E_{RKKY} \propto J_K^2\rho_F$ and it becomes smaller than $T_K$ with increasing $V$ (e. g., by pressure) as first demonstrated by [Doniach, 1977]. Correspondingly, in the case of metals the localized-moment regime is defined by $E_{RKKY} \gg T_K$ or, for the case of $E_{RKKY} \lesssim T_K$, by high temperatures $T \gg T_K$.

The rich variety of local-moment phenomena in actual compounds stems from the high degeneracy of $d$ or $f$ shells and its interplay with the crystalline environment. In particular, the crystal-field (CF) splitting plays a crucial role in determining the nature of local degrees of freedom in such systems. In localized transition-metal (TM) compounds, e.g. oxides, the orbital magnetic moment is quenched by the CF that is larger than the second Hund's rule coupling determined by the value of $J_H$. The CF in these systems is not determined solely by the actual electrostatic potential of crystalline environment, but includes also a large contribution of the "ligand field", i. e., of the hybridization between TM $d$ and ligand $p$ states. The orbital physics in such compounds is due to an anisotropic shape of CF orbitals leading to a directional-dependent superexchange [Goodenough, 1955, Kanamori, 1959] and strong coupling of the orbital order to the lattice distortions [Kugel' and Khomskii, 1982]. In contrast, the crystal-field splitting $\xi_{cf}$ is typically the smallest single-ion energy scale in the rare-earth (RE) $4f$ shells, i. e., $\xi_{cf} \ll \lambda_{SO} \ll J_H \ll U$, where $\lambda_{SO}$ is the spin-orbit coupling.

As mentioned above, the effect of hybridization in the local-moment state can be well described by a low-order perturbation theory in $W/U$, while the CF potential can be considered as essentially one-electron. Hence, the local-moment physics looks rather trivial compared to truly non-perturbative problems like the Mott or heavy-fermion phenomena. Though this is correct on the model level, our ability to quantitatively account for observed phenomena in real local-moment system is still quite limited, as compared, for example, with a quite impressive success of DFT in describing the ground-state properties of ferromagnetic $3d$ metals (for example, $\alpha$-Fe,

see Sec. 3.1). As described in Chap. 2, these difficulties are well understood to be caused by the static mean-field treatment of localized $d$ (in TM compounds) and $f$ (in REs) shells by local or semi-local exchange-correlation potentials. A popular *ad hoc* approach, in particular in the case of RE $4f$ states, consists in treating them as "open-core"; this approach predicts the ground-state volumes and balk moduli of elementary rare-earth metals in good agreement with experiment [Delin *et al.*, 1998]. However, the "spilling" of localized states outside of the core is then completely neglected; the calculated valence density of states misses, obviously, all $f$-electron features. A much more consistent approach is based on the explicit treatment of the on-site Coulomb repulsion by methods beyond the standard DFT framework introduced in Chap. 2. The simplest approach of this kind, LDA+U [Anisimov *et al.*, 1991, Anisimov *et al.*, 1997a], successfully captures the localization phenomena. However, the LDA+U is a single-electron framework, where the localization is (incorrectly) caused by the symmetry breaking. Atomic multiplets, which are sets of many-electron states degenerated in the case of spherical symmetry, are not present in LDA+U; spectral and magnetic properties of high-$T$ phases, correspondingly, cannot be directly calculated.

The more general DFT+DMFT framework has thus significant advantages over DFT+U as the many-electron physics of localized shells in a crystalline environment can be fully taken into account. In the case of localized-moment one has, as noted above, a natural small parameter, $W/U$. Hence, a number of approximate analytical techniques based on the expansion around the strong-coupling limit and partial resummation of the resulting diagrams can be employed to solve the DMFT quantum impurity problem (Sec. 2.2.1), for example, the first-order expansion in the hybridization [Dai *et al.*, 2005, Jia-Ning *et al.*, 2010], non-crossing [Bickers, 1987] and one-crossing [Pruschke and Grewe, 1989, Haule *et al.*, 2001] approximations. This chapter focuses on the simplest strong-coupling method, the so-called Hubbard-I approximation (HIA) [Hubbard, 1963], in which the hybridization function is completely neglected in the DMFT quantum impurity problem. In result, the later is reduced to the diagonalization of a single-shell Hamiltonian $\hat{H}_{at} = \sum_{ab} \varepsilon_{ab} f_a^\dagger f_b + \hat{H}_U$, where $\hat{\varepsilon}$ is the non-interacting level positions [Lichtenstein and Katsnelson, 1998]. In the DMFT framework $\hat{\varepsilon}$ obtained by a high-frequency expansion of the bath Green's function (2.6) reads:

$$\hat{\varepsilon} = -\mu + \langle \hat{H}_0 \rangle^{ff} - \Sigma_{\mathrm{DC}} \tag{4.1}$$

where $\mu$ is the chemical potential, $\langle \hat{H}_0 \rangle^{ff}$ is the Kohn-Sham Hamiltonian projected to the basis of $4f$ Wannier orbitals (2.2) and summed over the Brillouin zone, $\Sigma_{\mathrm{DC}}$ is the double counting correction term (2.4).

The single-shell Hamiltonian $\hat{H}_{at}$ commutes with the number operator and can be diagonal-

ized separately for each occupancy (with the largest Hilbert space of $\sim 10^3$ states in the case of an $f$ shell) and the atomic GF is then computed in the Lehmann representation

$$G_{at}^{\alpha\beta}(i\omega_n) = \sum_{\Gamma\Gamma'} \frac{\langle\Gamma|f_\alpha|\Gamma'\rangle\langle\Gamma'|f_\beta^\dagger|\Gamma\rangle}{i\omega_n - E_{\Gamma'} + E_\Gamma}(X_\Gamma + X_{\Gamma'}), \tag{4.2}$$

where $|\Gamma\rangle$ and $|\Gamma'\rangle$ are many-electron eigenstates of $\hat{H}_{at}$, $E_\Gamma$ and $X_\Gamma = \frac{e^{-\beta E_\Gamma}}{Z}$ are the corresponding eigenenergies and Boltzmann weights, respectively, $\alpha$ and $\beta$ label $4f$ orbitals, $Z$ is the partition function.

The method is very fast but is not fully consistent in the DMFT sense. The main DMFT condition is not satisfied, $G_{at} \equiv G_{imp} \neq G_{loc}$, because the hybridization function contributes to the local GF of the lattice problem (2.8) but not to the impurity GF $G_{imp}$. The width of Hubbard bands due to hybridization effects is thus underestimated in the HIA spectral function, $A(\mathbf{k},\omega) = \Im G(\mathbf{k},\omega+i\delta)$ [Dai *et al.*, 2005]. In spite of these inconsistencies this DFT+DMFT in conjunction with the HIA (abbriviated below as DFT+HubI) has been rather successfully used in calculations of the total-energy of localized Ce compounds [Pourovskii *et al.*, 2007, Amadon, 2012] as well as the spectral function of different RE and actinide systems [Lebègue *et al.*, 2005, Lebègue *et al.*, 2006, Pourovskii *et al.*, 2009, Shick *et al.*, 2009, Locht *et al.*, 2016]. In the later case the DFT+HubI spectral function basically represents a quasi-atomic multiplet structure of $f$ shell superimposed on the conduction-electron band structure provided by DFT. The effect of the solid-state environment on the $4f$ spectra is included in such calculations through the input screened value of $U$ (the value of $J_H$ in RE ions is known to be almost completely independent of the crystalline environment and is tabulated, e.g., in [Carnall *et al.*, 1989]), the self-consistent $f$ level positions $\hat{\varepsilon}$ introduced above and an (underestimated) broadening of the multiplet peaks due to hybridization effects. The method's limitations discussed above are not so significant for quasi-atomic RE $4f$ shells, and, for example, the DFT+HubI description of the spectroscopic features of RE metals compares quite satisfactory with the experiment [Locht *et al.*, 2016]. The method has also been applied, in conjunction with an additional correction for the value of $p-d$ semiconducting gap, to evaluate the color of RE-based semiconductors [Tomczak *et al.*, 2013].

This chapter discusses the application of DFT+HubI to somewhat more subtle problems, where one deals with comparable and competing energy scales arising due to the interaction between a localized atomic shell and its crystalline environment. Those scale are, in particular, the CF and exchange field (EF); their interplay with the spin-orbit coupling determines the key single-ion anisotropy of RE ions in rare-earth-based hard magnetic intermetallics [Buschow, 1991]. A DFT+HubI-based approach to their *ab initio* evaluation [Delange *et al.*, 2017] is presented in Sec. 4.2. The CF and EF interplay determines the low-

energy eigenstates of $\hat{H}_{at}$ and, through $G_{at}$ (4.2), the atomic self-energy and, therefore, the spectral function $A(\mathbf{k},\omega)$. Hence, the high-energy multiplet features forming Hubbard bands are also influenced by small CF and EF splitting; the same interplay is also shown to impact the exchange splitting of conduction states forming the Fermi surface [Pourovskii *et al.*, 2009]. These phenomena are considered in Sec. 4.2.4.

Another key energy scale in real localized compounds is the inter-site exchange (ISE) arising, as shortly described above, in perturbation treatment around the atomic limit as a $\propto W^2/U$. The ISE is often comparable to $\xi_{cf}$ in RE compounds [Fulde and Loewenhaupt, 1985] or to the spin-orbit splitting in TM Mott insulators leading to a complex interplay between the single-site physics and ordering phenomena. In crystal-field dominated RE compounds $\xi_{cf}$ is substantially larger than the inter-site interactions and only the lowest CF level is relevant. The low-energy order parameter in such cases can be still highly nontrivial in the case of a non-Kramers ion or a quadrupole lowest CF level resulting in an ordering of high-rank multipole moments [Santini *et al.*, 2009, Cameron *et al.*, 2016]. In the case of TM compounds the ISE couples orbital and spin moments of neighboring sites leading to Kugel-Khomskii-type Hamiltonains [Kugel' and Khomskii, 1982]; in $5d$ TM systems its interplay with a SO coupling leads to exotic magnetic phases [Jackeli and Khaliullin, 2009]. A reliable evaluation of such ISE coupling various local degrees of freedom in real insulating materials is therefore of high importance. A theory for *ab initio* evaluation of the ISE on the basis of DFT+HubI approximation was proposed by [Pourovskii, 2016]. It is described in Sec. 4.3.

## 4.2 Crystal-field and exchange-field effects in lanthanide compounds

Experimental values of crystal-field (CF) are directly obtained by measuring dynamic response functions due to transitions between CF levels (inelastic neutron scattering [Fulde and Loewenhaupt, 1985], dipole-forbidden inter-multiplet optical transitions in insulators [Carnall *et al.*, 1989]). Another set of measurements probes only the occupied CF levels: the static magnetic susceptibility (see, e.g., [Dunlap *et al.*, 1984]), magnetic form-factor [Boucherle *et al.*, 1982], Schottky anomaly in the specific heat (e.g., [Radousky *et al.*, 1983]). In these techniques the actual CF splitting is inferred from the temperature dependence of the signal. The X-ray spectroscopy was recently successfully employed to determine CF ground-state wave function in lanthanide compounds [Hansmann *et al.*, 2008, Willers *et al.*, 2012]. Generally, full calculations of the corresponding response functions are necessary to account for CF effects in different experimental probes. However, in the quasiatomic approximation employed by DFT+HubI the CF and exchange-field splitting will be determined solely by the corresponding

one-electron term of the following single-site Hamiltonian:

$$\hat{H}_{at} = \hat{H}_{1\mathrm{el}} + \hat{H}_U = \hat{E}_0 + \lambda \sum_i s_i l_i + 2\mu_B B_{\mathrm{ex}} \hat{S}_f^a + \hat{H}_{cf} + \hat{H}_U^{(o)}, \tag{4.3}$$

where the one-electron part of the Hamiltonian corresponds to the first four terms on the right-hand side, namely, a uniform shift, spin-orbit, exchange-field, and crystal field terms, $\hat{H}_U^{(o)}$ is the on-site Coulomb interaction. The exchange field $B_{\mathrm{ex}}$ due to a magnetic TM sublattice is explicitly included in (4.3) in anticipation of the subsequent discussion on RE-based magnetic intermetallics. It is coupled to the projection $\hat{S}_f^a$ of RE spin along a given direction $a$.

A more complete treatment of CF effects should generally include the impact due to hybridization, which is particularly important in TM Mott oxides. This can be accomplished by employing a cluster Hamiltonian that includes TM ion $d$ shell with the nearest-neighbor oxygen $p$ orbitals providing the "ligand field" (see, e. g., [Haverkort *et al.*, 2012] and references therein); the renormalization of CF spitting due to hybridization effects can be also inferred from the full solution of single-site DMFT quantum impurity problem by exact methods [Poteryaev *et al.*, 2008]. Below we show that the impact of hybridization on CF is still significant even for the $4f$ shell of rare-earth ions, but it can be effectively included by constructing "extended" Wannier functions representing the RE $4f$ orbitals in a solid.

By making use of the known angular character of $4f$ orbitals $w_{i\sigma}(\mathbf{r})$ centered on a given RE cite $i$ one may show that the CF term can be written as

$$\hat{H}_{cf} = \sum_{kq} L_k^q \hat{T}_k^q, \tag{4.4}$$

where

$$\hat{T}_k^0 = \hat{C}_k^0;\ \hat{T}_k^{\pm|q|} = \sqrt{\pm 1}\left[\hat{C}_k^{-|q|} \pm (-1)^{|q|}\hat{C}_k^{|q|}\right]$$

are Hermitian combinations of the Wybourne's operators $\hat{C}_k^q(\mathbf{r}) = \sqrt{4\pi/(2k+1)}Y_{kq}(\mathbf{r})$ [Wybourne and Meggers, 1965], $Y_{kq}(\mathbf{r})$ are spherical harmonics for a given angular quantum number $k \leq 2l = 6$ and its orbital projection $q$. $L_k^q$ is the corresponding CF parameter (CFP). The number of $L_k^q$ is strongly reduced by the point-group symmetry; few parameters are sufficient to completely determine CF in relatively high-symmetry tetragonal and hexagonal compounds considered below.

The notation for CFPs are somewhat confusing, as several different conventions are used in the literature. In particular, the very popular Steven's operator formalism [Stevens, 1952] employs another notation of CFPs, $A_k^q\langle r^k\rangle$, which can be conveted to the Wyborne's notation by a set of positive prefactors $\lambda_{kq} = A_k^q\langle r^k\rangle / L_k^q$. The Steven's approach substantially reduces the computational effort in evaluating the matrix elements of $\hat{H}_{cf}$ within the ground-state multiplet

of a $4f$ ion. With modern computers diagonalizing full $H_{at}$ is rather easy task and the usefulness of Steven's approach is less obvious, however, $A_k^q\langle r^k\rangle$ convention remains very popular in the literature. The conversion factors between Steven's and Wybourne's CFPs can be found, for example, in [Newman and Ng, 1989].

The one-electron CF contribution is hence given by the matrix elements of one-electron Kohn-Sham (KS) potential in the basis $w_{i\alpha}(\mathbf{r})$. The actual CFPs can then be obtained by fitting an *ab initio* $\hat{H}_{\mathrm{1el}}$ in (4.3) to the sum of (4.4) for a given point-group symmetry and other one-electron terms ($E_0$, $\lambda$, $B_{\mathrm{ex}}$). For spin-polarized systems the CFPs can be assumed to be spin-dependent and extracted separately for each spin.

Therefore, first-principles calculations of CFPs essentially boil down to constructing "proper" $4f$ orbitals and evaluating a "proper" KS potential acting on them. In practice, such quantitatively accurate *ab initio* calculations of CF turn out to be a challenging task. The DFT description of $4f$ states as metallic bands pinned at the Fermi level generally leads to poor agreement with experimental CF ([Daalderop *et al.*, 1992], see also [Richter *et al.*, 1992, Hummler and Fähnle, 1996]). First, the KS states occupancy (and, hence, the charge density and KS potential) due to such partially-filled metallic bands is quite different from that due the lower Hubbard band in the correct physical picture of localized $4f$ states [Bhandary *et al.*, 2016], see Sec. 2.3. Second, an unphysical contribution due to the local-density-approximation (LDA) self-interaction error is always present in the KS potential. This self-interaction contribution differs between $4f$ orbitals due to a non-uniform occupancy of $4f$ orbitals thus directly impacting the CF potentials [Brooks *et al.*, 1997]. Both problems can be cured by treating $4f$ states as an open core and directly removing their self-interaction [Steinbeck *et al.*, 1994, Novak and Kuriplach, 1994]. However, the effect due to $4f$ states mixing with other bands is then neglected, resulting in poor agreement when such hybridization is important, e.g., for RE oxides [Novák, 2013]; the treatment of $4f$ orbital's tails extending beyond the core region also becomes rather ambiguous. A mixed scheme proposed by [Novák *et al.*, 2013a] first generates the KS potential using the "$4f$-in-core" self-consistent calculations; the $4f$ orbitals are then represented by Wannier functions to compute the matrix elements of $\hat{H}_{\mathrm{1el}}$, an additional parameter is employed to correct for the hybridization of $4f$s with a selected set of itinerant bands. This scheme was rather successfully employed for a number of RE systems [Novák *et al.*, 2013b, Novák *et al.*, 2014b, Novák *et al.*, 2014a]. Another approach by [Zhou and Ozoliņš, 2009, Zhou and Ozoliņš, 2011] is based on constrained DFT+U calculations: the CF splitting is evaluated from a set of DFT+U total energies with the density matrix of localized shell constrained to corresponding CF levels.

### 4.2.1 Self-interaction-suppressed DFT+Hubbard-I approach

The description of localized $4f$ states provided by DFT+HubI are expected to be quite suitable for capturing crystal-field effects. In the present implementation $4f$ orbitals are represented by projected Wannier functions (2.2) [Amadon *et al.*, 2008, Aichhorn *et al.*, 2009] naturally including the tails; the charge density is derived from an electronic structure with $4f$ states forming the Hubbard bands at high binding energies as described in Sec. 2.3. No artificial symmetry breaking is introduced and the paramagnetic state is correctly described, in contrast with the DFT+U approach. Calculations of CFPs thus amount to self-consistent in the charge density DFT+HubI calculations with subsequent fitting of the resulting *ab initio* level positions (4.1) to the form of $\hat{H}_{1\text{el}}$ in (4.3) with CF given by (4.4). However, such direct standard DFT+HubI calculations lead to rather poor agreement with experiment, as illustrated by Table 4.1, where the CFPs obtained by DFT+HubI for Sm $4f$ in the well-known hard-magnetic intermetallic $SmCo_5$ are compared to experiment. The direct DFT+HubI method predicts, in particular, the wrong positive sign for the key $A_2^0\langle r^2\rangle$ CFP. Such a positive value of $A_2^0\langle r^2\rangle$ would mean an in-plane anisotropy for Sm ion, in contradiction to a strong easy-axis anisotropy of $SmCo_5$ determining its hard-magnetic behavior. This is due to the DFT self-interaction problem described above, which is not corrected by the standard DFT+HubI framework.

In order to address this problem [Delange *et al.*, 2017] proposed to enforce an uniform occupancy of all states within the $4f$ ground state multiplet in self-consistent DFT+Hub-I calculations. Namely, the imaginary-frequency Hubbard-I Green's function (4.2) was redefined as follows:

$$G_{\text{at}}^{\alpha\beta}(i\omega_n) = \frac{1}{M}\sum_{\substack{\Gamma\in\text{GSM}\\ \Delta\notin\text{GSM}}}\left(\frac{\langle\Gamma|f_\alpha|\Delta\rangle\langle\Delta|f_\beta^\dagger|\Gamma\rangle}{i\omega_n + E_\Gamma - E_\Delta} + \frac{\langle\Delta|f_\alpha|\Gamma\rangle\langle\Gamma|f_\beta^\dagger|\Delta\rangle}{i\omega_n - E_\Gamma + E_\Delta}\right) \tag{4.5}$$

where the eigenstates $|\Gamma\rangle$ and $|\Delta\rangle$ with eigenenergies $E_\Gamma$ and $E_\Delta$ belong to the ground-state multiplet (GSM) and excited multiplets respectively, $M$ is the degeneracy of the GSM. In other words, to obtain Eq. 4.5 the standard Boltzmann weight in (4.2) is substituted with the uniform weight $\tilde{X}_\Gamma = 1/M$ for the GSM and $\tilde{X}_\Delta = 0$ for exited multiplets in the spectral representation of the Green's function[1].

This approach can be also seen as replacing eq. 4.1 by

$$\hat{\varepsilon} = -\mu + \langle\hat{H}_0\rangle^{ff} - \Sigma_{\text{DC}} - \langle V_{\text{KS}}\left[n_{spd}(\mathbf{r}) + n_{4f}(\mathbf{r})\right]\rangle^{ff} + \langle V_{\text{KS}}\left[n_{spd}(\mathbf{r}) + \bar{n}_{4f}(\mathbf{r})\right]\rangle^{ff} \tag{4.6}$$

where $V_{\text{KS}}[n]$ is the Kohn-Sham potential evaluated from the total electronic density $n(\mathbf{r})$. $n_{4f}(\mathbf{r})$ designates the projected electronic density belonging to the RE's $4f$ orbitals, $\bar{n}_{4f}(\mathbf{r})$ is the same

[1] In RE systems the range of temperatures of interest is generally much lower than the inter-multiplet splitting, hence, the contribution of excited multiplets into the partition function $Z$ can be neglected.

| | DFT+HubI PM | DFT+HubI FM | | DFT+HubI direct | |
|---|---|---|---|---|---|
| $A_2^0\langle r^2\rangle$ | -140 | -313 | -262 | 278 | 331 |
| $A_4^0\langle r^4\rangle$ | -40 | -40 | -55 | -30 | -37 |
| $A_6^0\langle r^6\rangle$ | 33 | 35 | 25 | 38 | 25 |
| $A_6^6\langle r^6\rangle$ | -684 | -731 | -593 | -945 | -806 |
| $B_{\text{ex}}$ $(T)$ | - | 227 | | 235 | |

| | [Tils *et al.*, 1999] | [Tie-Song *et al.*, 1991] | [Givord *et al.*, 1979] |
|---|---|---|---|
| $A_2^0\langle r^2\rangle$ | -326 | -330 | -200 |
| $A_4^0\langle r^4\rangle$ | - | -45 | 0 |
| $A_6^0\langle r^6\rangle$ | - | 0 | 50 |
| $A_6^6\langle r^6\rangle$ | - | 0 | 0 |
| $B_{\text{ex}}$ $(T)$ | 260 | 327.5 | 260.5 |

| | [Richter *et al.*, 1995] | [Hummler and Fähnle, 1996] | [Novak and Kuriplach, 1994] |
|---|---|---|---|
| $A_2^0\langle r^2\rangle$ | -760 | -509 | -160 |
| $A_4^0\langle r^4\rangle$ | -37 | -20 | -33 |
| $A_6^0\langle r^6\rangle$ | 11 | 2 | 40 |
| $A_6^6\langle r^6\rangle$ | 290 | -55 | 168 |
| $B_{\text{ex}}$ $(T)$ | - | 279 | - |

Table 4.1: Top table: CF parameters (in K) and exchange field (in Tesla) in ferromagnetic (FM) and paramagnetic (PM) $SmCo_5$ calculated by the self-interaction-suppressed DFT+HubI method by [Delange *et al.*, 2017]. The "DFT+HubI direct" column lists results of standard DFT+HubI approach employing (4.2) instead of (4.5) and (4.7) . For comparison, measured (middle table) and calculated (bottom table) values from several groups are also given.

density, spherically averaged, and $n_{spd}(\mathbf{r})$ designates all the remaining density, belonging to all atoms' $s, p$ and $d$ orbitals. Hence, one effectively tunes the double-counting correction to remove the unphysical contribution due to self-interaction of $4f$ orbitals into the splitting of $\hat{\varepsilon}$.

Another problem is specific to the case of rare-earth based hard magnetic intermetallics. These systems are well described by so-called "two-sublattice model" [Campbell, 1972, Buschow, 1991], where the RE spins are aligned by a strong exchange field generated by the ferromagnetic order on TM (Fe, Co or Ni) sublattice. This coupling is included through a (semi-)local exchange-correlation potential (e. g., LSDA), which is expected to be suitable for itinerant TM ferromagnetism. However, once $4f$ states become spin-polarized the $4f$ magnetic density will generate through LSDA an exchange field coupled to the RE spins themselves. The interaction term in (4.3) already contains the Hund's rule coupling $J_H$ between $4f$ orbitals, hence, the LSDA exchange field due to the $4f$ magnetization density acting on the these orbitals represents double counting. In the case when the LSDA exchange field is smaller than the $4f$ inter-multiplet

splitting it is effectively removed by employing (4.5). To remove this double counting in a general case [Delange *et al.*, 2017] directly suppressed the $4f$ contribution to the magnetization density from the DFT+DMFT density matrix at each $\mathbf{k}$-point:

$$\tilde{N}^{\mathbf{k}} = N^{\mathbf{k}} + \frac{1}{2} P^{\dagger}(\mathbf{k}) \left( \mathcal{T} n^{ff}(\mathbf{k}) \mathcal{T}^{\dagger} - n^{ff}(\mathbf{k}) \right) P(\mathbf{k}) \tag{4.7}$$

where $N^{\mathbf{k}}$ is the density matrix in the Bloch basis (2.12), $P(\mathbf{k})$ is the projector (2.2) between the Wannier and Bloch spaces, $n^{ff}(\mathbf{k}) = P(\mathbf{k}) N^{\mathbf{k}} P^{\dagger}(\mathbf{k})$ is the density matrix in the $4f$ orbitals basis, $\mathcal{T}$ is the time-reversal operator. The averaged density matrix $\tilde{N}^{\mathbf{k}}$ is then used to recalculate the electron density at the next DFT iteration, see Sec. 2.3. The resulting exchange field $B_{\text{ex}}$ in (4.3) is subsequently extracted from converged DFT+HubI level positions $\hat{\varepsilon}$ together with CFPs.

The CFPs and $B_{\text{ex}}$ for $SmCo_5$ evaluated using the sef-interaction-suppressed DFT+HubI scheme [Delange *et al.*, 2017] are listed in Table 4.1. The calculated lowest-order CFP $A_2^0\langle r^2 \rangle$ agrees well with experimental measurements in the ferromagnetic phase. These calculations also predict rather strong dependence of $A_2^0\langle r^2 \rangle$ on the magnetic state of $SmCo_5$; this is apparently stemming from a strong modification of the Co $3d$ density of states by its strong ferromagnetism. The fact that the electronic structure of Co $3d$ has a such significant impact on the CF on Sm points out to an important contribution to CFP due to the $4f$-$3d$ mixing. Another unexpected result is a large magnitude of the $A_6^6\langle r^6 \rangle$ CFP, which magnitude is rather difficult to extract from NIS experiments [Hummler and Fähnle, 1996]. The Sm $4f$ eigenstates and their splitting obtained by [Delange *et al.*, 2017] are also in good agreement with experimental values inferred from magnetic form factor measurements [Givord *et al.*, 1979, Laforest, 1981].

### 4.2.2 Crystal field and single-ion magnetic anisotropy in $R\text{Fe}_{12}X$ intermetallics

The approach described above was applied by [Delange *et al.*, 2017] to the "1−12" family of $R\text{Fe}_{12}X$ compounds that has recently attracted significant interest [Körner *et al.*, 2016, Suzuki *et al.*, 2016, Harashima *et al.*, 2015, Hirayama *et al.*, 2015, Miyake *et al.*, 2014]. These compounds crystallize in the $ThMn_{12}$-type tetragonal structure. Upon doping with light elements $X$ such as nitrogen they exhibit hard magnetic properties (large magnetization, Curie temperature, and strong anisotropy [Suzuki *et al.*, 2016, Harashima *et al.*, 2015, Hirayama *et al.*, 2015] ) comparable to those of the top high-perfomance hard magnet $Nd_2Fe_{14}B$, in spite of the reduced concentration of rare earth elements. [Delange *et al.*, 2017] evaluated the effect of N and Li interstitials on the CFPs, exchange field on RE sites (Nd or Sm) and the resulting RE single-ion anisotropy. The calculated lowest order CFP $A_2^0\langle r^2 \rangle$ and

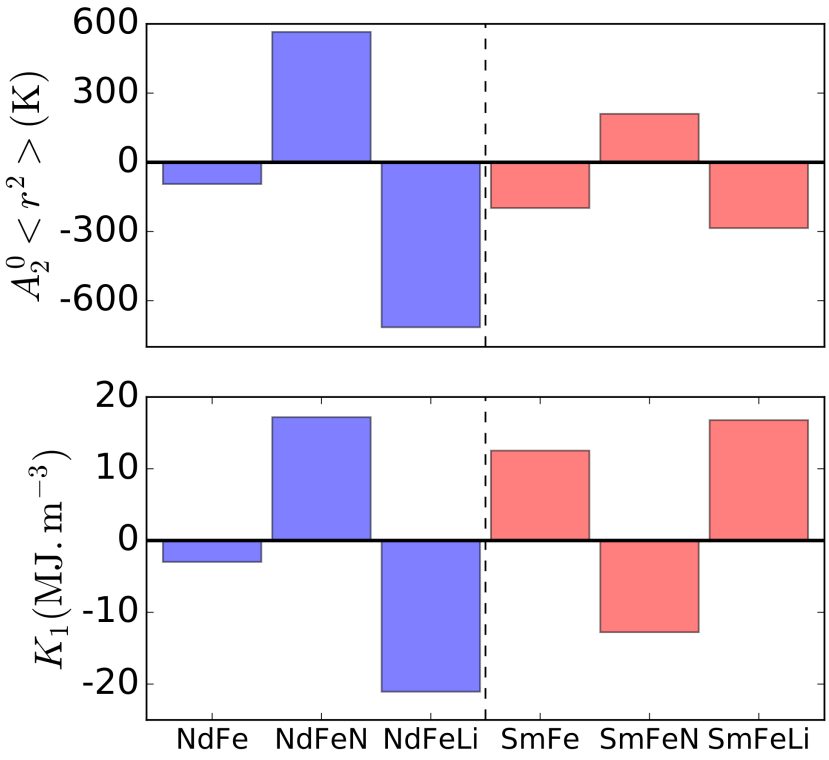


Figure 4.1: Crystal field parameters $A_2^0\langle r^2\rangle$ (average over up and down spins in the FM phase) and anisotropy coefficient $K_1$ for $R\mathrm{Fe}_{12}X$, with $R$=Nd, Sm and $X$ is either empty, N or Li. The proportional numbers in compounds formulas are omitted for brevity. Adapted from [Delange *et al.*, 2017].

corresponding anisotropy coefficient

$$K_1 = -3J(J - \frac{1}{2})\alpha_J A_2^0\langle r^2\rangle n_R, \tag{4.8}$$

where $J$ is the total angular momentum for the rare earth $4f$ shell, $n_R$ is the concentration of rare earth atoms, $\alpha_J$ is the corresponding Steven's factor, for all considered systems are shown in Fig. 4.1.

A strong effect of the interstitial on the CFP $A_2^0\langle r^2\rangle$, which is increased the N interstitial and decreased by the Li one, is clearly seen in Fig. 4.1 and is in agreement with experimental results finding a strong uniaxial magnetic anisotropy in $\mathrm{NdFe}_{12}\mathrm{N}$ [Hirayama *et al.*, 2015] and $\mathrm{SmFe}_{12}$ [Hirayama *et al.*, 2017], but an in-plane anisotropy in $\mathrm{SmFe}_{12}\mathrm{N}$ and $\mathrm{NdFe}_{12}$ ([Harashima *et al.*, 2015] and references therein). These "1−12" tetragonal compounds are not stable in their bulk stoichometric compositions, hence, the experimental results were obtained in thin films grown on a substrate and/or by substitutional doping of Fe sublattice by

Ti or Co. In order to understand the origin of the effect of interstitials [Delange *et al.*, 2017] analyzed the leakage of the $4f$ Wannier orbitals to nearest-neighbors sites and found it to be strongly orbital-dependent due to the anisotropic shape of $4f$ orbitals. In particular, the $4f$ orbital for the magnetic quantum number $m = 0$ leaks to the N(Li) interstitial ligand site resulting in an upward (downward) shift of its energy due to the ligand's electrostatic potential and hybridizational mixing with the ligands orbitals. The $m = 0$ level position is positively correlated with the value of $A_2^0\langle r^2\rangle$ as one may infer from the matrix form of $\hat{T}_2^0$ operator in the $f$ angular basis. Hence, its positive (negative) shift due to a N(Li) interstitial leads to the corresponding shift of $A_2^0\langle r^2\rangle$.

[Delange *et al.*, 2017] also calculated the temperature dependence of the single-ion anisotropy without resorting to the lowest-order approximation (4.8) and employing instead the direct diagonalization of *ab initio* Hamiltonian (4.3) obtained by DFT+HubI. Interestingly, the hypothetical $SmFe_{12}Li$ compound was found to be an excellent hard magnet, with its temperature stability of anisotropy being far superior to that of existing perspective hard magnet $NdFe_{12}N$. Unfortunately, alkali metals do not mix with iron [Kubaschewski, 1982], hence, stabilizing $SmFe_{12}Li$ in its bulk tetragonal phase might not be possible.

### 4.2.3 Localization of Wannier $4f$ orbitals and crystal-field parameters

In the DFT+HubI framework the hybridization function is neglected; the crystal-field splitting is fully contained in the single-site non-interacting level position matrix $\hat{\varepsilon}$ given by eq. 4.1. Yet, as described above, the hybridization with ligand orbitals of the N and Li interstitials is seen to strongly affect the calculated CFPs for the $R\mathrm{Fe}_{12}X$ compounds. This seemingly paradoxical result stems from the representation of RE $4f$ orbitals in solids by extended Wannier orbitals (WO). The degree of extension for the $4f$ WO $w_{i\alpha}(\mathbf{r})$ is determined by the range of bands $\mathcal{W}$ included into the projective construction of WO in (2.2). This extension is most significant in the case of a narrow range $\mathcal{W}$ including only bands of the target character (e.g., $3d$, $4f$). In this case an admixture of other characters (e.g., N $2p$ to $4f$-like bands in $R\mathrm{Fe}_{12}\mathrm{N}$) leads to extension of the resulting WOs to the corresponding sites (i.e., the N interstitial in the example above).

Two limits are useful to consider in the present case: the "small window" WO basis constructed from KS bands of mainly $4f$ character and the "large window" basis that includes all KS bands with some $4f$ contribution. In the case of $4f$ states entangled with other bands, as in the TM-RE intermetallics considered above, the former limit can (approximately) be defined by an energy range of few eV comprising mainly $4f$-like bands, which are pinned in the vicinity of $E_F$ within DFT. The "large window" limit will in addition include all TM $3d$, RE $5d$ and the interstitial ligand states.

The real-space Nd $4f$ WO $w_m(\mathbf{r})$ for the orbital quantum number $m = 0$ in paramagnetic

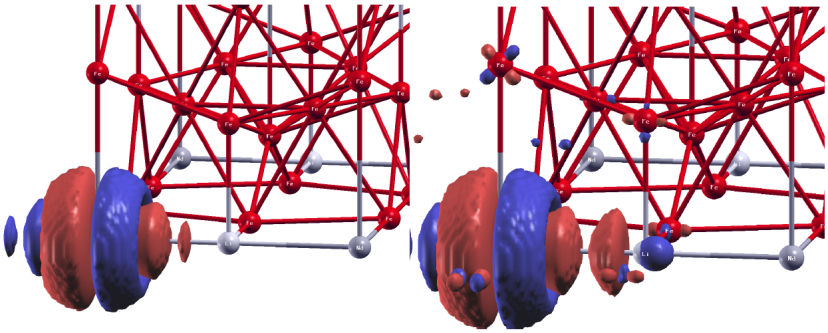

(a) $[-20, 20]$ eV window (b) $[-2, 2]$ eV window

Figure 4.2: Nd Wannier orbital $m = 0$ in $NdFe_{12}Li$ constructed with a large window $[-20, 20]$ eV (left) and a small window $[-2, 2]$ eV (right). Adapted from [Delange *et al.*, 2017].

$NdFe_{12}Li$ constructed for those two limits using $\mathcal{W}$ of $[-2 : 2]$ and $[-20 : 20]$ eV, respectively, is depicted in Fig 4.2. A noticeable leakage of the "small-window" extended WO to the Li site as well as smaller contributions due to Fe $3d$ are clearly seen; in contrast, the "large-window" WO is restricted at the Nd site. By expanding the small-window WO $w_m(\mathbf{r})$ in a basis of localized "large-window" ones constructed for all valence bands [Delange *et al.*, 2017] could quantify the contribution of different non-$4f$ characters into $w_m(\mathbf{r})$ as a function of $m$.

The admixture of states hybridizing with RE $4f$ into the corresponding extended WOs allows to effectively include the impact of hybridization on CFPs within the DFT+HubI approach. This impact is expected to be more important in RE oxides and similar compounds that features a significant mixing of RE $4f$ and ligand $p$ orbitals [Novák, 2013].

In order to assess it the self-interaction-corrected DFT+HubI method has been also applied to the $R$OCl rare earth oxychloride series. The tetragonal oxyclorides $R$OCl are wide-gap semiconductors; in contrast to the TM-RE intermetallics considered above, the CF splitting in $R$OCl is accessible to optical measurements probing weak $4f$-$4f$ transitions [Hölsä and Lamminmäki, 1996]. In these calculations both localized and extended WOs were employed for the sake of comparison. The extended ones were constructed including only the manifold of narrow RE $4f$ bands pinned at the $E_F$. A wide range, $\mathcal{W} \in [-6 : 11.5]$ eV, which includes also the O $2p$, Cl $3p$ and RE $5d$ bands (see Fig. B.1 in Appendix B), was employed to construct the localized WOs. Other relevant parameters of these calculations are detailed in Appendix B.

The CF (4.4) on the RE site in $R$OCl is specified by five parameters $L_k^q$ (designated as $B_k^q$ in [Hölsä and Lamminmäki, 1996]): $L_2^0$, $L_4^0$, $L_4^4$, $L_6^0$, and $L_6^4$. The calculated CFPs are compared to the measured ones in Fig. 4.3. One may notice a good agreement with experiment for DFT+HubI calculations employing extended WOs. This agreement is especially good for the

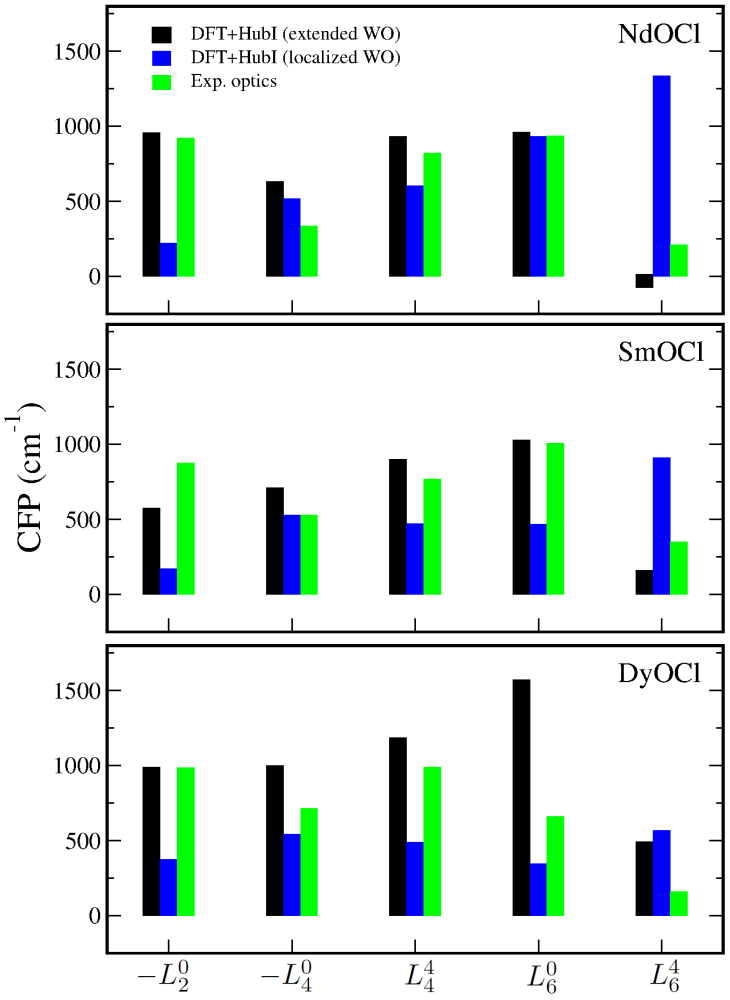


Figure 4.3: Crystal-field parameters (in $\mathrm{cm}^{-1}$) in $R$OCl oxychlorides (where $R$ =Nd, Sm, and Dy) calculated by the self-interaction-suppressed DFT+HubI method using extended and localized WOs. The experimental values are from optical measurements of [Hölsä and Lamminmäki, 1996].

lowest rank CFP $L_2^0$; some significant discrepancies are however observed for the rank-6 CFPs in the case of DyOCl. As noted above, high-rank CFPs are most difficult to measure precisely experimentally. In contrast, one observes a significant systematic underestimation of $L_2^0$ by the method with localized WOs, a less pronounced underestimation is also noticeable for the rank-4 CFPs. Overall, the difference between DFT+HubI results with localized and extended WOs is very significant pointing to a large contribution of hybridization effects to the CF effect in these compounds.

### 4.2.4 Crystal-field effects in the electronic structure of rare-earth compounds

A significant advantage of the DFT+HubI method with respect to less direct DFT/DFT+U approaches of [Novák *et al.*, 2013a, Zhou and Ozoliņš, 2011] is its ability to simultaneously evaluate the impact of CF splitting on the electronic structure of RE compounds as measured by photoemission (PES) experiments and Fermi-surface probes like the de Haas-van Alphen and Shubnikov-de Haas (SdH) effects. Once the one-electron level positions $\hat{\varepsilon}$ are obtained, e. g. by the self-interaction-suppressed DFT+HubI calculations described above, the atomic GF is evaluated from $\hat{\varepsilon}$ in accordance with eqs. 4.3 and 4.2. The resulting atomic self-energy is subsequently inserted back to the lattice, eq. 2.5, to evaluate the spectral function $A(\mathbf{k},\omega)$. At temperatures smaller than the magnitude of CF splitting atomic-like multiplet features of $4f$ typically seen in PES of RE compounds will be due to one-electron exitations from the CF ground state. Hence, the interplay of CF with exchange (or external magnetic) fields will have a direct impact on $A(\mathbf{k},\omega)$ obtained within DFT+HubI.

The impact of CF effects on the one-electron spectra in the RE semimetal ErAs was assessed by DFT+HubI calculations of [Pourovskii *et al.*, 2009]. The Er local moments in the rock-salt lattice structure of this compound spontaneously order antiferromagnetically at $T_N$ =4.5 K, but this antiferromagnetism was suppressed by a large external magnetic field of about 5 T employed in Shubnikov-de Haas (SdH) experiments of [Bogaerts *et al.*, 1996] thus resulting in a ferromagnetic alignment of Er moments. The DFT+HubI calculations for this compound under such applied field show, however, that the field is not sufficient to overcome the CF splitting

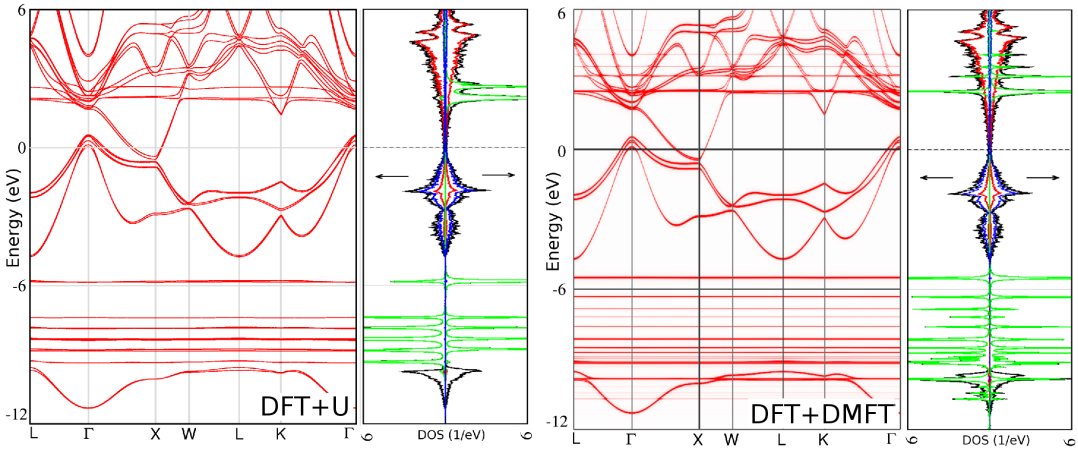


Figure 4.4: Band structure and density of states (DOS) of ErAs from DFT+U (left); DFT+DMFT **k**-resolved and integrated spectral functions at an applied field of 5 T (right). The total is black line, the partial Er $5d$, Er $4f$ and As $4p$ contributions are displayed by the red, green, and blue curves respectively. Adapted form [Pourovskii *et al.*, 2009].

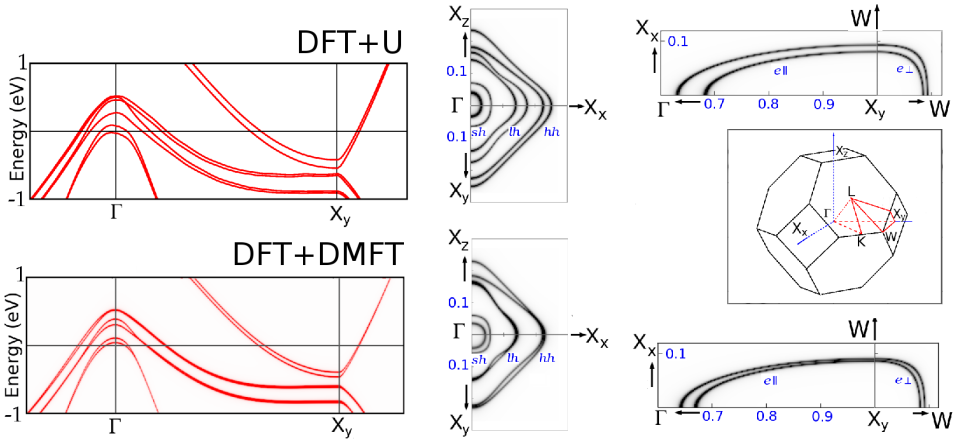


Figure 4.5: The low-energy electronic structure of ErAs within the DFT+U(top) and DFT+DMFT (bottom) approaches. The spin polarization is along the $z$ axis, thus the cubic symmetry is lifted, and the band structure along $x(y)$ and $z$ axis are not equivalent. The corresponding $X$ high-symmetry points of the fcc Brillouin zone are designated as $X_x$, $X_y$, and $X_z$, respectively (inset at the right-hand side). The overlapping semi-metallic As $4p$ and Er $5d$ bands near $E_F$ are shown on the left-hand side. They are followed to the right by the cross sections of the hole pockets at the Γ point in the $xy$ and $xz$ planes, and the longitudinal $e \parallel$ (in the $\Gamma X_y W$ plane) and transverse $e \perp$ (in the $X_y W W$ plane) cross sections of the electronic pocket. The exchange splittings of the pockets are clearly seen. Adapted form [Pourovskii *et al.*, 2009].

of Er $4f$ states, resulting in only partially-polarized Er $4f$ band[2]. The DFT+HubI spectra is compared in Fig. 4.4 to that obtained within the DFT+U method. The later is not only missing various multiplet peaks but also incorrectly predicts a fully-polarized Er $4f$ band.

A ferromagnetic order of RE spins $\hat{S}_f$ leads to a measurable exchange splitting of the Fermi surface due to a double-exchange term like $I_{fc}\hat{S}_f\hat{S}_c$, where $\hat{S}_c$ is the conduction electron spin on the same site (see, e. g. [Jensen and Mackintosh, 1991]). As described above, the CF effect freezes a partially-polarized state of the Er $4f$ shell in DFT+HubI, and, hence, the exchange field $2\mu_B I_{fc}\langle\hat{S}_f\rangle$ acting on the conduction-electron spin. In result, DFT+DMFT calculations of [Pourovskii *et al.*, 2009] predict a markedly smaller exchange splitting of the semimetalic Er $5d$ and As $3p$ bands compared to the Hund's rule state found by DFT+U (Fig. 4.5) and quasiparticle GW calculations of [Chantis *et al.*, 2007]; these DFT+DMFT predictions are in good quantitative agreement with the SdH experiment.

*Vice versa* the spin-polarization of itinerant bands generates an exchange field acting on $4f$

[2]DFT+HubI calculations of [Pourovskii *et al.*, 2009] employed the atomic-sphere approximation (ASA) for the crystalline potential. This approximation largely removes the self-interaction between $4f$ states, but in contrast to the more recent self-interaction-suppressed scheme (Sec. 4.2.1) it also neglects physical non-spherical contributions due to other states to the exchange-correlation potential. ErAs is a cubic compound in which the rank-2 CFPs are zero by symmetry, and the ASA treatment of [Pourovskii *et al.*, 2009] was found to be sufficient to reproduce its CF in a good agreement with experiment.

shells. In the case of hard-magnetic RE-iron intermetallics described in Sec. 4.2.2 the ferromagnetic order on Fe sublattice induces a spin polarization of conduction electrons (mainly RE $5d$) leading to an exchange field $\vec{B}_{eff} = 2\mu_B I_{fc}\langle\hat{S}_c\rangle$ acting on the RE spin, see eq. 4.3. This term can be described in the DFT framework e.g. within LSDA as in [Delange *et al.*, 2017]. Again, due to the crystal-field effect one obtains only partial polarization of the $4f$ Hubbard bands in the DFT+HubI spectral function. Correspondingly, for example, the ordered Nd spin magnetic moment in $NdFe_{12}N$ is reduced to 1.6 $\mu_B$ as compared to the Hund's rule value of 3 $\mu_B$.

## 4.3 Linear response to two-site fluctuations and inter-site exchange interactions

As briefly outlined in the introduction to this chapter, inter-site exchange (ISE) interactions represent a key energy scale in localized systems. In conjunction with the magneto-elastic coupling they are at the origin of ordering phenomena in these compounds. ISE interactions may couple not only spins, but also orbital [Kugel' and Khomskii, 1982] and higher rank multipole degrees of freedom [Santini *et al.*, 2009]. Experimental measurements of exchange interactions are particularly difficult in the case of such orbital or multipolar order parameters, as the conventional neutron-scattering spectroscopy is not sensitive to them, e. g., one cannot directly see multipolar excitations by inelastic neutron scattering measurements. Hence, transitions to multipole-ordered phases are first seen only in thermodynamical functions, while the actual order parameter remains "hidden", as in the prototypical examples of $CeB_6$ [Cameron *et al.*, 2016], $URh_2Si_2$ [Mydosh and Oppeneer, 2011], or $NpO_2$ [Santini *et al.*, 2009]. An orbital order in TM compounds usually manifests itself by a distortion of a high-symmetry paramagnetic lattice structure; it is generally not possible to experimentally disentangle the purely electronic contribution of superexchange and that due to the lattice Jan-Teller mechanism.

Direct *ab initio* evaluation of phase diagrams for such complex systems as a function of temperature and external parameters (pressure, applied field) is not generally feasible at present. In particular, while the DFT+DMFT method is able to treat local correlations at finite temperatures, typical low symmetries of ordered phases and low temperatures of interest as well as a vast space of possible order parameters render direct predictive DFT+DMFT calculations in this case rather difficult. Moreover, the single-site DMFT method suffers from the usual mean-field drawbacks overestimating ordering temperatures, especially for low-dimensional systems (see, for example, [Rohringer *et al.*, 2011, Hirschmeier *et al.*, 2015, Schäfer *et al.*, 2015, Ayral and Parcollet, 2015, Horvat *et al.*, 2017]).

A promising two-step approach for a first-principles description of orbital and multipolar ordering phenomena consists in using the DFT+DMFT method to evaluate an effective

low-energy Hamiltonian due to ISE interactions between localized shells. Those Hamiltonians can then be solved by a variety of methods developed for Heisenberg-like models in order to predict the ordered phase as a function of external parameters like pressure or temperature. This kind of techniques have been previously developped within the standard DFT framework [Prange and Korenman, 1979, Wang *et al.*, 1982, Oguchi *et al.*, 1983, Liechtenstein *et al.*, 1987, Bruno, 2003, Ruban *et al.*, 2004] mainly for evaluating effective spin Hamiltonians. Some DFT+DMFT generalizations of this approach have been also developed [Katsnelson and Trefilov, 2000, Secchi *et al.*, 2015].

The key idea of Lichtenstein *et al.* [Liechtenstein *et al.*, 1987, Katsnelson and Lichtenstein, 2000, Kvashnin *et al.*, 2015] is to evaluate the first order change of the DFT (or DFT+DMFT) grand potential $\Omega$ due ot simultaneous titling of spins on two neighboring sites $\mathbf{R}$ and $\mathbf{R}'$ in otherwise a completely ordered phase, $\Delta\Omega \approx V^{\mathbf{R}\mathbf{R}'}\delta\phi(\mathbf{R})\delta\phi(\mathbf{R}')$, where $\delta\phi(\mathbf{R})$ is the infinitesimal titling angle for the spin at the site $\mathbf{R}$. The ISE $V^{\mathbf{R}\mathbf{R}'}$ is then shown using the so-called "force theorem" [Mackintosh and Andersen, 1980] to be equal to $\int d\omega \,\mathrm{Tr}\left[\Delta_{\mathbf{R}}(\omega)G_{\mathbf{R}\mathbf{R}'}(\omega)\Delta_{\mathbf{R}'}(\omega)G_{\mathbf{R}'\mathbf{R}}(\omega)\right]$, where $\Delta_{\mathbf{R}}(\omega)$ is the on-site exchange splitting, $G_{\mathbf{R}\mathbf{R}'}(\omega)$ is the intersite GF describing the propagation of electron between the corresponding sites.

The approach of Lichtenstein *et al.* has been successfully applied to a wide range of materials using both the DFT and DFT+DMFT frameworks, the initial paper [Liechtenstein *et al.*, 1987] is cited about 800 times as of 2018. However, their use of an ordered state as a reference can be a disadvantage for applications to correlated materials. As noted above, symmetry-broken low-$T$ phases are generally less accessible within DFT+DMFT. The method is also not so easily extended to more complex order parameters like orbital or multipolar ones. The corresponding ordered phase should be first obtained by full self-consistent calculations to subsequently evaluate its response to "titling" of "generalized spins". Hence, while a rather heavy formalism for such generalization has been developped [Secchi *et al.*, 2015] it has not been so far applied to realistic materials. A DFT+U formalism based on flipping high-rank multipole moments in an ordered state was recently applied to magnetic and quadrupolar order in $UO_2$ [Pi *et al.*, 2014].

[Pourovskii, 2016] proposed an approach for evaluating ISE interactions directly from DFT+DMFT calculations of symmetry-unbroken paramagnetic phase. This method is based on evaluating the response of DFT+DMFT grand potential (**??**) to simultaneous fluctuations of the correlated shell density matrix on two neighboring sites. In the spirit of "force theorem" the effect of small fluctuations on $\Omega_r[n(\mathbf{r})]$ is neglected, then one may show that only the contribution of first term in (**??**) is nonzero for a two-site fluctuation as all other terms in (**??**) are

site-diagonal. The resulting expression for the grand-potential response reads:

$$\frac{\delta^2\Omega}{\delta\rho(\mathbf{R})\delta\rho(\mathbf{R}')} = \sum_n \mathrm{Tr}\left[G_{\mathbf{R}\mathbf{R}'}(i\omega_n)\frac{\delta\Sigma_{\mathbf{R}'}(i\omega_n)}{\delta\rho(\mathbf{R}')}G_{\mathbf{R}'\mathbf{R}}(i\omega_n)\frac{\delta\Sigma_{\mathbf{R}}(i\omega_n)}{\delta\rho(\mathbf{R})}\right], \tag{4.9}$$

where, analogously to the Lichtenstein interactions, $G_{\mathbf{R}\mathbf{R}'}$ is the inter-site GF describing the propagation of electron between the sites $\mathbf{R}$ and $\mathbf{R}'$, $\delta\rho(\mathbf{R})$ is the fluctuation of density matrix at the site $\mathbf{R}$ with respect to its value in the paramagnetic state.

The response of DMFT self-energy to the fluctuation of density matrix $\frac{\delta\Sigma_{\mathbf{R}}}{\delta\rho(\mathbf{R})}$ was evaluated by [Pourovskii, 2016] within the HIA. In the localized limit, where the charge fluctuations are neglected and the magnitude ISE is assumed to be small compared to the inter-multiplet splitting, the fluctuation $\delta\rho(\mathbf{R})$ was restricted in this approach to the ground-state multiplet (GSM) of a given shell. The GSM contribution in the quasi-atomic GF is first separated out, $G_{at} = \mathrm{Tr}\left[\hat{\rho}_{GSM}\hat{G}\right] + G^1_{at}$, where the Green's function matrix $\hat{G}$ describes the transition from/to GSM as $G^{\Gamma\Gamma'}_{\alpha\beta}(\tau) = -\left\langle\Gamma|\mathrm{T}[f_\alpha(\tau)f^\dagger_\beta(0)]|\Gamma'\right\rangle$, where the notation is as in eq. 4.5. The rest is collected in $G^1_{at}$. The GSM density matrix, $\hat{\rho}_{GSM}$, is diagonal within the HIA, its elements are the Boltzmann weights of quasi-atomic eigenstates in the symmetry-unbrocken paramagnetic state, see (4.2). Defining the fluctuations of diagonal $\delta\rho^{\Gamma\Gamma}$ and off-diagonal $\delta\rho^{\Gamma\Gamma'}$ elements in $\hat{\rho}_{GSM}$ such that its trace is conserving one derives for the variational derivative of $G_{at}$ with respect to such fluctuations the following equation:

$$\frac{\delta G_{at}}{\delta\hat{\rho}^{\Gamma\Gamma'}} = G^{\Gamma'\Gamma} - \delta_{\Gamma\Gamma'}\frac{Tr[\hat{G}]}{M}. \tag{4.10}$$

The corresponding response of the atomic self-energy, $\frac{\delta\Sigma^{at}}{\delta\hat{\rho}^{\Gamma\Gamma'}}$, is then obtained from (4.10) through the Dyson equation. Inserting resulting $\frac{\delta\Sigma_{at}}{\delta\hat{\rho}^{\Gamma\Gamma'}}$ into eq. 4.9 one thus obtains the response of $\Omega$ to fluctuations within the GSM on two sites, $\frac{\delta^2\Omega}{\delta\rho^{\Gamma_1\Gamma_2}(\mathbf{R})\delta\rho^{\Gamma_3\Gamma_4}(\mathbf{R}')}$. As discussed in [Pourovskii, 2016] one may then identify (suppressing the $\Gamma$ label for brevity):

$$\frac{\delta^2\Omega}{\delta\rho^{12}(\mathbf{R})\delta\rho^{34}(\mathbf{R}')} = \langle 13|V^{\mathbf{R}\mathbf{R}'}|24\rangle, \tag{4.11}$$

where the RHS is the corresponding matrix element of a low-energy interaction $V^{\mathbf{R}\mathbf{R}'}$ between the corresponding density-matrices of two sites.

One may transform these density-matrix ISE into a more conventional form of those between the corresponding on-site dipole and multipole operators (dipole, quadrupole etc.). The advantage of this form is that the expectation values and correlation functions of those operators are directly accessible to experimental probes (like the neutron scattering in the case of dipole magnetic moments). Moreover, the symmetries of the problem are often directly apparent

leading to a compact form of the low-energy Hamiltonian[3]. The density matrix of a given GSM with the quantum number $J$ can be equivalently represented by a set of $(2J+1)^2$ multipole moments [Blum, 1996, Santini *et al.*, 2009], $\hat{\rho}(J) = \sum_{K,Q} \langle O_{KQ}(J) \rangle \hat{O}_{KQ}$, where $\langle O_{KQ}(J) \rangle$ is the state multipoles with the rank $K = 0, 1, ..2J$ and component $Q = -K...K$, $\hat{O}_{KQ}$ is the corresponding self-adjoint spherical tensor. These state multipoles are in fact experimentally observable multipole moments, e.g. the vector ($K = 1$) moments $\langle O_{1\bar{1}}(J) \rangle$, $\langle O_{10}(J) \rangle$, and $\langle O_{11}(J) \rangle$ are the expectation values of $\hat{J}_y$, $\hat{J}_z$, and $\hat{J}_x$, respectively, divided by $\sqrt{2}$. One may introduce the corresponding ISE $V^{QQ'}_{KK'}(\mathbf{RR'})$ between such multipoles on two different sites as $\sum_{\substack{KK' \\ QQ'}} V^{QQ'}_{KK'}(\mathbf{RR'}) \hat{O}_{KQ}(\mathbf{R}) \hat{O}_{K'Q'}(\mathbf{R'})$. Using the orthogonality properties of the spherical tensors [Pourovskii, 2016] showed that ISE can be transformed from the density-matrix to multipole-multipole interaction form as follows:

$$\sum_{\substack{m_1 m_2 \\ m_3 m_4}} \langle m_1 m_3 | V^{\mathbf{RR'}} | m_2 m_4 \rangle O^{m_2 m_1}_{KQ}(J) O^{m_4 m_3}_{K'Q'}(J) = V^{QQ'}_{KK'}(\mathbf{RR'}). \tag{4.12}$$

where $m$ is the magnetic quantum number for a given $J$.

In the case of TM systems the spin and orbital degrees of freedom of the relevant TM shell are often encoded by spin $s$ and pseudospin $\tau$ quantum numbers, respectively [Kugel' and Khomskii, 1982]. One may then represent the density matrix by double tensors, which are direct products of the type $\hat{O}_{KQ}(s) \times \hat{O}_{K_1 Q_1}(\tau)$ of the corresponding spherical tensors for the $s$ and $\tau$ spaces. A mapping of the density-matrix ISE into spin/pseudospin ones is then derived analogously to (4.12) .

Overall, ISE calculations in the approach of [Pourovskii, 2016] consist in evaluating the variational derivatives of self-energy by (4.10) in conjunction with the Dyson equation and the inter-site GF $G_{\mathbf{RR'}}$ by a Fourier transform of the lattice GF. All possible interactions $\langle 12 | V^{\mathbf{RR'}} | 34 \rangle$ between two sites that are allowed within a given GSM are subsequently computed by (4.9) and mapped to the multipole form by (4.12). The method hence obtains all possible interactions between multipoles allowed within the GSM; one does not need to identify the relevant ones in advance.

This approach was benchmarked by applying it to 1-band and two-band $e_g$ Hubbard models on the simple-cubic 3d lattice. In the former case it was shown analytically to lead to $J = -4t^2/U$ for the Heisenberg nearest-neighbor interaction, which is a well known result for $t \ll U$. The obtained interactions, hence, exhibit the $\sim 1/U$ scaling expected for correlated insulators. The method is not applicable for metals, where the condition $t \ll U$ is obviously not satisfied. ISE for

[3] For example, in the case of spin $\hat{S}$ being the low-energy degree of freedom in a translational-invariant system without spin-orbit, the values of all $(2S+1)^4$ matrix elements (4.11) are determined by a single Heisenberg constant $J$ coupling the corresponding spin moments.

the two-band $e_g$ model map to a spin-orbital Kugel-Khomskii (KK) Hamiltonian; the values of resulting spin, orbital, and spin-orbital ISE as a function of the ratio $J_H/U$ are in close agreement with previous analytical calculations of [Oleś *et al.*, 2000].

### 4.3.1 *Ab initio* Kugel-Khomskii Hamiltonian and spin-orbital order in $KCrF_3$

The formalism presented above was applied by [Pourovskii, 2016] to evaluate an *ab initio* spin-orbital KK-type Hamiltonian for the chromium fluoride $KCrF_3$. This compound represents a typical example of a Mott insulator with spin and unquenched orbital degrees of freedom ordering at different temperature scales. Its paramagnetic high-temperature phase adopts the conventional cubic peroxide structure [Margadonna and Karotsis, 2007]. The $3d$ shell of the $Cr^{2+}$ ion is in the $t_{2g}^3 e_g^1$ configuration with the spin of single $e_g$ electron aligned to that of the half-filled $t_{2g}$ subshell by the Hund's rule coupling, similarly to the peroxide manganese $LaMnO_3$. The relevant low-energy degrees of freedom are thus the $S = 2$ spin and $e_g$ orbital. The later is encoded by the 1/2-pseudospin $\tau$, with its values $+1/2$ and $-1/2$ designating the $t_{2g}^3[x^2 - y^2]$ and $t_{2g}^3[3z^2 - r^2]$ orbital states of $Cr^{3+}$, respectively. Hence, in the paramagnetic phase the total degeneracy of the GSM of $Cr^{3+}$ is equal to $(2\tau + 1)(2S + 1) = 10$.

All the corresponding matrix elements (4.11) between those states on neighboring Cr ions were evaluated for several first coordination shells. The obtained ISE were subsequently converted to the tensor/operator formalism as outlined above. The ISE interactions obtained for next nearest and more distant neighbors are at least an order of magnitude smaller than the nearest-neighbor (NN) ones and were neglected. The calculated NN superexchange(SE) Hamiltonian between two nearest neighbors $i$ and $j$ along the [001] direction was found to be of the following form

$$\begin{aligned}\hat{H}_{eff}^{[001]} =& J_{ss}\sum_{\alpha}\hat{S}_{i\alpha}\hat{S}_{j\alpha} + J_{\tau\tau}\hat{\tau}_{iz}\hat{\tau}_{jz} + J_{sq}\sum_{\alpha}\left[\hat{S}_{i\alpha}(\hat{S}_{j\alpha}\hat{\tau}_{jz}) + (\hat{S}_{i\alpha}\hat{\tau}_{iz})\hat{S}_{j\alpha}\right] + \\ & J_{qq}\sum_{\alpha}(\hat{S}_{i\alpha}\hat{\tau}_{iz})(\hat{S}_{j\alpha}\hat{\tau}_{jz}) + ...,\end{aligned} \tag{4.13}$$

where $J_{ss}$, $J_{\tau\tau}$, $J_{sq}$, and $J_{qq}$ are the spin-spin, orbital-orbital, spin-(spin-orbital) and (spin-orbital)-(spin-orbital) interactions; some smaller terms are omitted for brevity [4]. The calculated SE interactions for two values of Hubbard $U$ at fixed Hund's rule coupling $J_H$ =0.75 eV [5] are listed in Table 4.2. One may see that the orbital-orbital interaction is the dominant one (notice,

[4] As expected, the calculated effective Hamiltonians for the [100] and [010] bonds are related by the cubic symmetry to $\hat{H}_{eff}^{[001]}$ and can be obtained from it by corresponding rotations in the $\tau$ space.

[5] The values of 3.75 eV and 0.75 eV were obtained for $U(= F^0)$ and $J_H$, respectively, by [Autieri *et al.*, 2014] using the cLDA approach.

Table 4.2: Calculated Cr-Cr nearest-neighbor interactions along the [001] direction, in meV .

| U (eV) | $J_{ss}$ | $J_{\tau\tau}$ | $J_{sq}$ | $J_{qq}$ |
|---|---|---|---|---|
| 3.75 | 0.94 | 37.3 | -1.77 | 7.12 |
| 5 | 0.96 | 24.7 | -1.43 | 4.93 |

however, that for a proper comparison of the magnitude of terms in (4.13) one needs to take into account the different lengths of spins $S = 2$ and pseudospins $\tau = 1/2$).

The calculated KK Hamiltonian (4.13) was subsequently solved within the mean-field approximation obtaining ordered phases of cubic $KCrF_3$ as a function of temperature. The resulting evolution of the specific heat vs. $T$ and identified ordered phases are depicted in Fig. 4.6. Two phase transitions are clearly identified: the high-temperature one at $T_{OO}$ of 340 K is due to ordering of the $e_g$ orbitals into the G-type antiferro-orbital (AFO) structure shown in 4.6b (all NN having opposite orbital states, i.e. the ordered vector $\mathbf{k} = [1/2, 1/2, 1/2]$ ). The low-

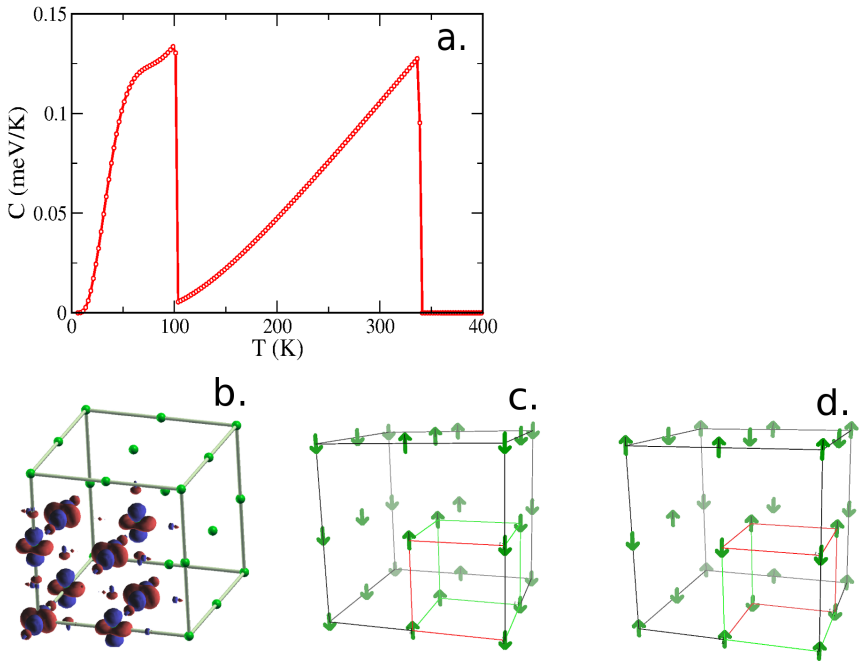


Figure 4.6: a. Specific heat (per formula unit of $KCrF_3$) as a function of temperature obtained by solving the Hamiltonian (4.13) using the mean-field approximation (implemented by MCPHASE package [Rotter, 2004]) with the values of superexchange interactions calculated at $U = 3.75$ eV. b. The G-type antiferro-orbital order obtained below $T_{OO} = 340$ K (plotted by XCrysDen [Kokalj, 2003], the real-space representation of the orbitals are generated with the help of the wplot [Kuneš *et al.*, 2010] program). c. The A-type antiferromagnetic phase, stable below $T_N = 102$ K, obtained with the interactions calculated with $U = 3.75$ eV d. The C-type antiferromagnetic phase obtained using the interactions calculated with $U = 5$ eV. Adapted from [Pourovskii, 2016].

temperature transition at $T_N$ of about 100 K is due to subsequent ordering of the $S = 2$ spins; the A-type antiferromagnetic (AFM) layered structure obtained for $U$ =3.75 eV is displayed in Fig. 4.6c. This structure consists of an AFM stacking of ferromagnetically-ordered [100] layers. Increasing the value of $U$ to 5 eV results in orbital ordering into the same AFO structure at lower $T_{OO}$ of 225 K. The AFM structure obtained in that case is however different; it is of C-type consisting of an anitferromagnetic stacking of ferromagnetically-ordered [110] layers (Fig. 4.6 d). One may analyze ordering energies for different magnetic structures for cubic $KCrF_3$ in the presence of fully-saturated G-type AFO. Such analysis shows that the stability of layered AFM structure with respect to the G-type AFM and ferromagnetic phases is controlled by the ratio of $J_{ss}/J_{\tau\tau}$. A more subtle mechanism is responsible for stabilization of the A-type AFM with respect to the C-type one; it is shown by [Pourovskii, 2016] to be due to the spin-orbital coupling $J_{sq}$ leading to canting of the G-type AFO once the A-type AFM structure sets in. The relative strength of $J_{ss}$, $J_{qq}$ and $J_{sq}$ SE interactions is determined by the $J_H/U$ ratio [Feinberg *et al.*, 1998, Oleś *et al.*, 2000], hence, increasing $U$ at fixed $J_H$ results in the observed change of AFM structure.

Experimentally the onset of G-type orbital order in $KCrF_3$ is accompanied by significant tetragonal distortions [Margadonna and Karotsis, 2007]; this Jahn-Teller contribution plays, apparently, the leading role as the experimental $T_{OO}$ = 973 K is much higher than the one obtained by [Pourovskii, 2016] by including only the superexchange contribution; the same conclusion was obtained by direct DFT+DMFT calculations of $KCrF_3$ with a CT-QMC impurity solver [Autieri *et al.*, 2014]. $KCrF_3$ subsequently undergoes a monoclinic distortion at 250 K [Margadonna and Karotsis, 2006] and orders into the A-type AFM structure shown in Fig. 4.6 at 80 K [Xiao *et al.*, 2010]. Hence, the magnetic order and $T_N$ are well reproduced by SE Hamiltonian (4.13) once the G-type orbital order sets in. Overall, this first application of the DFT+HubI based approach of [Pourovskii, 2016] for evaluating ISE in a realistic system demonstrates its ability to capture the hierarchy of complex spin-orbital SE interactions. It also allows to disentangle the lattice and purely electronic contribution to ordering phenomena in TM systems. This approach was also subsequently applied by [Horvat *et al.*, 2017] to evaluate purely spin-spin SE interactions in layered TM oxides and fluorides.

Chapter 5

# Conclusions and perspectives

In the previous two chapters we have reviewed recent studies employing a framework combining first-principles DFT approach with the single-site DMFT treatment of electronic correlations. In these works the impact of dynamical many-electron effects has been evaluated in two opposite limits: in correlated metallic systems exemplified by iron, and, on the other hand, in local-moment TM and lanthanide compounds.

Chap. 3 focused on correlation effects in various phases of iron at high-pressure conditions. In particular, a significant enhancement of dynamical correlations at the pressure-induced $\alpha \rightarrow \varepsilon$ phase transition is predicted by these calculations. This enhancement is explained by the fact that dynamical correlations are strongly suppressed by the static spin polarization in ferromagnetic $\alpha$-Fe; this polarization is absent in paramagnetic hcp $\varepsilon$-Fe. In result, our calculations predict large many-body corrections to the equation of state of the $\varepsilon$-phase and a significant electron-electron scattering contribution to its electrical resistivity for the moderate pressure range up to 50 GPa. We also predict an electronic topological transition to occur in this intermediate pressure range thus explaining observed peculiarities in the evolution of its hexagonal cell parameters, Debye velocity and Mössbauer central shift.

Applying the same framework to the geophysically-important regime of the Earth's inner core conditions we find a strong structural dependence of electronic correlations ranging from an almost ideally Fermi-liquid hcp $\varepsilon$-phase to strongly non-Fermi-liquid bcc $\alpha$-Fe. The many-body correction to the electronic total and free energies is consequently also strongly structurally dependent. The strength of correlations in iron is found to be sensitive to the local environment and significantly affected by the presence of Ni nearest neighbors. Finally and quite unexpectedly, the predicted "dull" Fermi-liquid state of $\varepsilon$-Fe leads to a significant suppression of the Lorenz number resulting in an enhanced contribution of the electron-electron scattering to the thermal resistivity. This enhancement of the thermal resistivity as compared to electrical one is directly related to a strong (quadratic) frequency dependence of the Fermi-liquid electron-electron scattering rate.

All these results have been obtained by the numerically-exact continuous-time quantum Monte Carlo (CT-QMC) method, which is equally reliable for all considered regimes of correlations (e. g., Fermi-liquid/non-Fermi-liquid, paramagnetic/ferromagnetic phases). However,

this approach is computationally heavy thus restricting its applicability to more difficult cases like highly-degenerate $f$ shells of rare-earth elements, strong spin-orbit coupling, low-symmetry systems and complex magnetic orders.

In Chap. 4 we focus on precisely such kind of systems - local-moment lanthanide and TM compounds. We demonstrate that DFT+DMFT, even in conjunction with the simplest quasi-atomic many-body approach, the Hubbard-I approximation, provides quite coherent and quantitative description of some magnetic and electronic properties of these systems. In particular, DFT+Hubbard-I is a reliable tool for evaluating the crystal-field splitting on localized $4f$ shells in lanthanides. The hybridization contribution to CF is effectively accounted for by representing the $4f$ states by extended Wannier orbitals, while the unphysical DFT self-interaction contribution to CF can be also efficiently suppressed within DFT+Hubbard-I . The calculated crystal-field splitting is in good quantitative agreement with experiment for $SmCo_5$ and rare-earth oxychlorides $R$OCl. Applying the same approach to perspective hard-magnetic intermetalics of the $R$Fe$_{12}X$ family we find a strong sensitivity of CF to the interstitial $X$ directly impacting the key single-ion rare-earth contribution to the magnetic anisotropy. The interplay of CF with exchange or external magnetic fields impacts both high and low-energy electronic structure of lanthanide compounds and is shown to be detectable in photoemission and Fermi-surface measurements.

Finally, inter-site exchange coupling in local-moment systems like superexchange and RKKY, though not captured by the standard DFT+Hubbard-I, can be extracted using a linear response technique presented in Sec. 4.3. This method is based on evaluating the response of DFT+DMFT grand potential to simultaneous fluctuations on two localized shells with respect to their symmetry-unbroken paramagnetic state. Using this approach one may calculate not only standard Heisenberg-like spin-spin interactions, but also couplings between orbital and multipolar local degrees of freedom as demonstrated by employing it to obtain an *ab initio* Kugel-Khomskii Hamiltonian for a realistic TM fluoride.

**Perspectives:**

Further development of the work presented in this review will be focused on more precise treatment of many-electron effects and their interplay with other degrees of freedom in these systems.

In particular, the present DFT+DMFT framework is still too simplified to fully account for the complex physics of iron under pressure. Some promising directions for further research on this exciting system are listed below:

- The use of full rotationally-invariant Coulomb interaction instead of its simplified density-density form may be important, e.g., in the case of iron and its alloys. Non-density-density spin-flip terms of the local vertex were found by [Pourovskii *et al.*, 2014b] to be

essential to account for the collapse of static antiferromagnetism in this phase. The effect of rotationally-invariant interaction in $\varepsilon$-Fe thus needs to be fully investigated [1].

- A very significant contribution of the electron-electron scattering to the electrical resistivity of $\varepsilon$-Fe and its non-Fermi-liquid behavior at low temperatures, as well as a non-conventional (spin-fluctuation-paring) superconductivity experimentally observed in this phase, hint at important inter-site correlations, which can be included only by approaches beyond the single-site approximation. Hopefully, the recent progress in development of extended-DMFT frameworks [Rohringer *et al.*, 2018] will eventually make accessible the most important two-particle quantities (e.g., the full $\mathbf{k}$ and $\omega$-dependent magnetic susceptibility or vertex corrections to the transport) for realistic multi-band systems with possibly significant intersite correlation, like $\varepsilon$-Fe in the moderate pressure range.

- The density-density approximation for the local vertex is not qualitatively important in the case of EIC conditions[2]. The non-local correlations are also expected to be less important away from magnetic instabilities and with a lower strength of correlations at the high-density of the EIC matter. In contrast, the fixed-lattice approximations is quite severe when one considers temperatures just below the melting. Correspondingly, future studies of the impact of lattice vibrations on electronic correlations and vice versa are in this case of high importance. Fully consistent DFT+DMFT *ab initio* molecular dynamics will remain prohibitively computationally expensive for some time, therefore, one still needs to make use of the usual approximation of evaluating the electronic structure at fixed ionic coordinates. In order to assess the effect of lattice distortions on many-electron effects one may thus employ a set of supercells representing characteristic deviations from the perfect atomic positions expected for a given phase at relevant temperatures. Conversely, the impact of electronic correlations on lattice vibrations, at least in the harmonic approximation, can be studied using the recently formulated DFT+DMFT schemes for calculation of forces and phonon dispersions [Leonov *et al.*, 2012, Leonov *et al.*, 2014a, Haule and Pascut, 2016]. Eventually, the impact of light elements inclusions needs to be also included in realistic simulations of the EIC matter.

In the case of localized compounds an obvious limitation of the framework presented in Chap. 4 is the Hubbard-I approximation. This approximation drastically restricts the range of applicability for the DFT+DMFT; a full solution of the quantum impurity problem is necessary

[1] Preliminary calculations with such local vertex were not successful due to a persistent sign problem [Seth, 2016]

[2] In particular, the inclusion of rotationally-invariant local interaction the study of $\varepsilon$-Fe by [Pourovskii *et al.*, 2017] led only to some quantitative changes compared to the previous study within the density-density approximation, see also Appendix A.

for more general systems deviating from strictly localized limit.

This concerns, of course, Ce and Yb systems, for which the Kondo phenomenon cannot be neglected. In particular, Ce-based hard-magnetic intermetallics have attracted a lot of attention recently [Zhou *et al.*, 2014, Goll *et al.*, 2014]; in order to predict theoretically their magnetic anisotropies one needs to fully include the effect of Kondo screening for the Ce $4f$ shell [Capehart *et al.*, 1993]. The magnetism and one-electron spectra of Ce-based heavy-fermion compounds at low temperatures has been recently evaluated by DFT+DMFT in conjunction with the CT-QMC method [Matsumoto *et al.*, 2009, Pourovskii *et al.*, 2014a, Goremychkin *et al.*, 2018]. However, the magnetic anisotropy is a sensitive quantity and it is not clear whether one will be able to quantitatively evaluate it using stochastic many-body techniques like the CT-QMC. Analytical strong-coupling approaches briefly described in Sec. 4.1 can thus be also employed for such systems. The impact of heavy-fermion phenomenon on the structural stability of Ce-based intermetallics has not been so far studied by advanced *ab initio* approaches; this question is certainly of high interest for technological applications. In general, the interplay of TM ordered magnetism and heavy-fermion physics is not restricted to Ce systems, among Yb compounds one may mention, e. g., the $YbMn_6Ge_{6-x}Sn_x$ system [Mazet *et al.*, 2013].

The approach for evaluating inter-site exchange interactions (ISE) presented in Sec. 4.3 has been to date formulated only in the framework of Hubbard-I approximation and applied to a very limited set of systems. There one may point out several perspective directions both for applications of the existing framework and for its generalization beyond the quasi-atomic approximation:

- The existing method can be applied to a number of classical multipolar-ordered systems, like actinide dioxides [Santini *et al.*, 2009], cerium hexaboride [Cameron *et al.*, 2016], Pr-based skutterudites [Shiina, 2004] etc. Such phenomena have so far been studied by a combination of experiment and simplified theoretical models; the input from *ab initio* methods has been rather limited [Pi *et al.*, 2014]. The present technique might be able to reliably extract inter-site multipolar exchange couplings in these systems, to asses their sensitivity to lattice distortions, pressure etc.

- There is no obvious theoretical limitation to extending the present technique beyond the Hubbard-I approximation. Such generalization should be based on evaluating the response $\frac{\delta\Sigma_{\mathbf{R}}}{\delta\rho(\mathbf{R})}$ of the DMFT self-energy to a fluctuation of the on-site density matrix (see eq. 4.9), which should be accessible as a two-particle correlation function, e. g., by CT-QMC and other exact techniques.

- The generalization described above should make the method applicable to a wide range

of compounds, where a magnetic (multipolar) order coexists/competes with the heavy-fermion behavior. Extracting the inter-site exchange experimentally is especially challenging in such cases as it is intertwined with the Kondo local-moment screening. As example of perspective systems to study with the generalized technique one may point out RKKY interactions in the "115" and "112" families of Ce/Yb compounds as well as the famous "hidden" order in $URu_2Si_2$.

In addition, to evaluate various physical properties of interest one needs eventually to solve the derived low-energy quantum Hamiltonian. It would be, of course, preferable to advance beyond the single-site mean-field approximation to include intersite and quantum effects, especially for low-dimensional or frustrated systems. For this task one may consider employing a rich range of techniques developed in the field of quantum magnetism, from non-linear spin-waves [Chernyshev and Zhitomirsky, 2009] and Swinger bosons [Auerbach, 1994] to different quantum Monte Carlo methods [Sandvik, 2010].

Appendix A

# The impact of density-density approximation: Fe at the inner core conditions

In this appendix we illustrate the impact of density-density approximation for the local Coulomb interaction by performing DFT+DMFT calculations with and without this approximation for the bcc $\alpha$ and hcp $\varepsilon$ iron phases at the Earth's core condition. Self-consistent in the charge density DFT+DMFT calculations (Sec. 2.3) were thus carried out for the perfect bcc and hcp lattices at the atomic volume of 7.05 Å/atom expected for the inner core of Earth and the temperature of 5800 K. The on-site Coulomb interaction was defined by the parameters $U$ =5.0 eV, $J_H$ =0.93 eV previously used in the study of $\varepsilon$-Fe by [Pourovskii *et al.*, 2017]; the same choice for the energy window ( [-10.8 eV, 4.0 eV] around the Fermi level) was also employed for the Kohn-Sham states used to construct Wannier orbitals representing Fe 3$d$ states. The DMFT impurity problem was solved by the hybridization-expansion quantum Monte Carlo impurity solver using its segment-picture version [Werner *et al.*, 2006, Gull *et al.*, 2011] in case of the density-density (Ising) vertex and the implementation of [Seth *et al.*, 2016] in the case of full rotationally-invariant

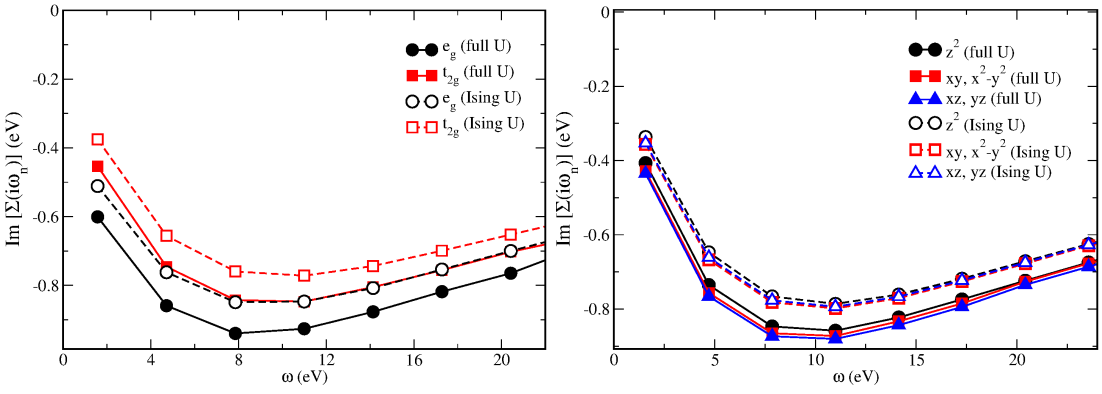


Figure A.1: Left panel: The imaginary part of DMFT self-energy on the Matusbara grid for the non-degenerate orbitals of the Fe 3$d$ shell in the bcc structure calculated with the rotationally-invariant (filled symbols) and density-density (empty symbols) local Coulomb interaction, respectively. Right panel: the same for the hcp structure.

one.

The resulting DMFT self-energies for both phases are compared in Fig. A.1. For both bcc and hcp-Fe the use of density-density approximation results in a systematic underestimation of the magnitude of scattering $|Im\Sigma(i\omega_n)|$, which is, however, more pronounced in the case of more correlated bcc. Qualitative features, like the $e_g$ orbitals markedly more correlated than the $t_{2g}$ ones in bcc-Fe as well as a uniform Fermi-liquid behavior of all orbitals in hcp, are well captured within the density-density approximation. We have also calculated the transport using the approach outlined in Sec. 3.3.2 and these self-energies analytically continued to the real-energy axis. The electrical and thermal conductivities for bcc are found to be overestimated by 40% and 29%, respectively, due to the density-density approximation. As expected, the impact of this approximation for the less-correlated hcp phase is smaller and amounts to 33% and 23%, respectively. Hence, though the use of full vertex does not lead to qualitative changes it is still found to be important for quantitative results.

Appendix B

# DFT+Hubbard-I calculations of rare-earth oxychlorides *R*OCl

The *R*OCl oxychlorides ($R$ =Nd, Sm, Dy) were calculated using their experimental lattice structures measured by [Hölsä *et al.*, 2002]. The tetragonal unit cell of these compounds (space group P4/nmm) exemplified by SmOCl is shown in Fig. B.1. The extended Wannier orbitals representing RE $4f$ states were constructed using only $4f$-like KS bands located in the vicinity of the Fermi level, as shown in Fig. B.1. The localized Wannier orbitals were constructed using a wide range of bands enclosed by the energy window $\mathcal{W} \in [-6 : 11.5]$ eV, i. e., using all the bands shown in Fig. B.1.

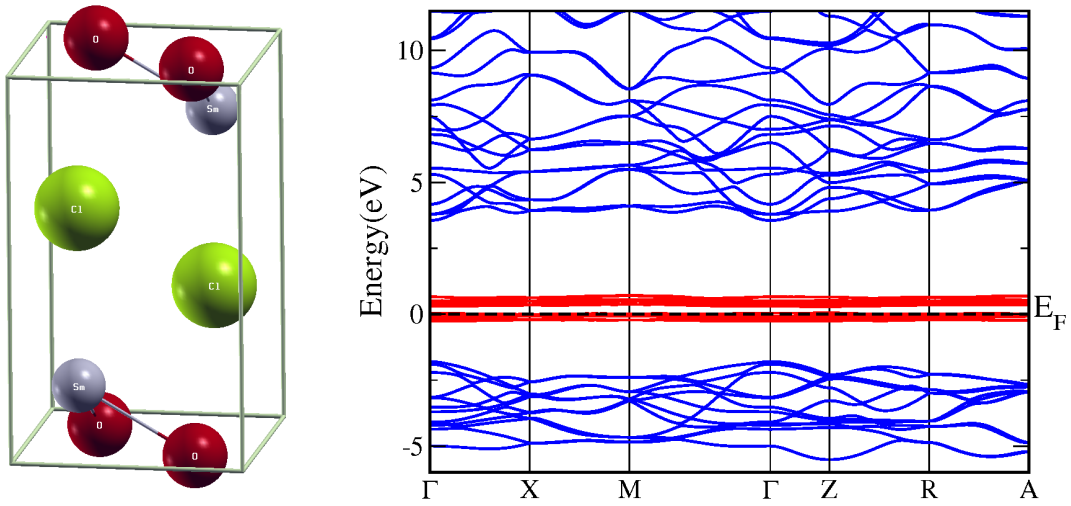


Figure B.1: Left panel: the unit cell of SmOCl. Right panel: the DFT band structure of SmOCl. The extended Wannier orbitals for Sm $4f$ are constructed only from the $4f$-like KS bands located in the vicinity of the Fermi level (in red). The splitting between two manifolds of those $4f$ bands is due to the spin-orbit coupling. All other bands displayed (in blue) are included (together with the $4f$ ones) in the construction of localized Wannier orbitals.

The local Coulomb interaction between RE $4f$ orbitals was specified by the Hund's rule coupling $J_H$ equal to 0.77, 0.85, and 0.99 eV for Nd, Sm, and Dy ions, respectively, the Slater

parameter $F^0 = U = 7.5$ eV was employed all ions. The chosen value of $U$ is in the middle of a typical range from 5 to 10 eV expected for RE compounds; the values of $J_H$, which are known to be almost completely independent of the crystalline environment, are taken from [Carnall *et al.*, 1989]. Crystal-field effects exhibit a weak dependence on $U$ and $J_H$ as long as these parameters remain larger than other relevant energy scales of the problem (i. e., the spin-orbit coupling and crystal field itself), as explicitly verified by [Delange *et al.*, 2017].

Self-consistent in the charge density DFT+HubI calculations were carried employing the self-interaction-suppressed scheme (eq. 4.5) with the corresponding degeneracies of 10, 6, and 16 of the ground-state multiplets for the Nd, Sm, and Dy ions, respectively. The LDA exchange correlations was employed and the spin-orbit included in the second variation procedure. The fully-localized-limit double counting correction [Czyżyk and Sawatzky, 1994] was used throughout and evaluated with the nominal $4f$ occupancies of RE ions [Pourovskii *et al.*, 2007].

# Bibliography


[Abrikosov *et al.*, 2016] Abrikosov, I., Ponomareva, A., Steneteg, P., Barannikova, S., and Alling, B. (2016). Recent progress in simulations of the paramagnetic state of magnetic materials, *Current Opinion in Solid State and Materials Science* **20**, 85 – 106.

[Aichhorn *et al.*, 2010] Aichhorn, M., Biermann, S., Miyake, T., Georges, A., and Imada, M. (2010). Theoretical evidence for strong correlations and incoherent metallic state in FeSe, *Phys. Rev. B* **82**, 064504.

[Aichhorn *et al.*, 2011] Aichhorn, M., Pourovskii, L., and Georges, A. (2011). Importance of electronic correlations for structural and magnetic properties of the iron pnictide superconductor LaFeAsO, *Phys. Rev. B* **84**, 054529.

[Aichhorn *et al.*, 2016] Aichhorn, M., Pourovskii, L., Seth, P., Vildosola, V., Zingl, M., Peil, O. E., Deng, X., Mravlje, J., Kraberger, G. J., Martins, C., Ferrero, M., and Parcollet, O. (2016). TRIQS/DFTTools: A TRIQS application for ab initio calculations of correlated materials, *Computer Physics Communications* **204**, 200 – 208.

[Aichhorn *et al.*, 2009] Aichhorn, M., Pourovskii, L., Vildosola, V., Ferrero, M., Parcollet, O., Miyake, T., Georges, A., and Biermann, S. (2009). Dynamical mean-field theory within an augmented plane-wave framework: Assessing electronic correlations in the iron pnictide LaFeAsO, *Phys. Rev. B* **80**, 085101.

[Alfé *et al.*, 1999] Alfé, D., Gillan, M. J., and Price, G. D. (1999). The melting curve of iron at the pressures of the Earth's core from ab initio calculations, *Nature* **401**, 462–464.

[Amadon, 2012] Amadon, B. (2012). A self-consistent DFT+DMFT scheme in the projector augmented wave method: applications to cerium, $Ce_2O_3$ and $Pu_2O_3$ with the Hubbard I solver and comparison to DFT+U, *Journal of Physics: Condensed Matter* **24**, 075604.

[Amadon *et al.*, 2006] Amadon, B., Biermann, S., Georges, A., and Aryasetiawan, F. (2006). The $\alpha-\gamma$ Transition of Cerium Is Entropy Driven, *Phys. Rev. Lett.* **96**, 066402.

[Amadon *et al.*, 2008] Amadon, B., Lechermann, F., Georges, A., Jollet, F., Wehling, T. O., and Lichtenstein, A. I. (2008). Plane-wave based electronic structure calculations for correlated materials using dynamical mean-field theory and projected local orbitals, *Phys. Rev. B* **77**, 205112.

[Amador *et al.*, 1992] Amador, C., Lambrecht, W. R. L., and Segall, B. (1992). Application of generalized gradient-corrected density functionals to iron, *Phys. Rev. B* **46**, 1870–1873.

[Ambrosch-Draxl and Sofo, 2006] Ambrosch-Draxl, C. and Sofo, J. O. (2006). Linear optical properties of solids within the full-potential linearized augmented planewave method, *Computer Physics Communications* **175**, 1 – 14.

[Andersen and Saha-Dasgupta, 2000] Andersen, O. K. and Saha-Dasgupta, T. (2000). Muffin-tin orbitals of arbitrary order, *Phys. Rev. B* **62**, R16219–R16222.

[Andersen *et al.*, 1980] Andersen, O. K., Skriver, H. L., Nohl, H., and Johansson, B. (1980). Electronic structure of transition metal compounds; ground-state properties of the $3d$-monoxides in the atomic sphere approximation, *Pure Appl. Chem.* **52**, 93–118.

[Anderson, 1950] Anderson, P. W. (1950). Antiferromagnetism. Theory of Superexchange Interaction, *Phys. Rev.* **79**, 350–356.

[Anisimov *et al.*, 1997a] Anisimov, V. I., Aryasetiawan, F., and Lichtenstein, A. I. (1997a). First-principles calculations of the electronic structure and spectra of strongly correlated systems: the LDA + U method, *Journal of Physics: Condensed Matter* **9**, 767.

[Anisimov *et al.*, 2005] Anisimov, V. I., Kondakov, D. E., Kozhevnikov, A. V., Nekrasov, I. A., Pchelkina, Z. V., Allen, J. W., Mo, S.-K., Kim, H.-D., Metcalf, P., Suga, S., Sekiyama, A., Keller, G., Leonov, I., Ren, X., and Vollhardt, D. (2005). Full orbital calculation scheme for materials with strongly correlated electrons, *Phys. Rev. B* **71**, 125119.

[Anisimov *et al.*, 1997b] Anisimov, V. I., Poteryaev, A. I., Korotin, M. A., Anokhin, A. O., and Kotliar, G. (1997b). First-principles calculations of the electronic structure and spectra of strongly correlated systems: dynamical mean-field theory, *Journal of Physics: Condensed Matter* **9**, 7359.

[Anisimov *et al.*, 1991] Anisimov, V. I., Zaanen, J., and Andersen, O. K. (1991). Band theory and Mott insulators: Hubbard U instead of Stoner I, *Phys. Rev. B* **44**, 943–954.

[Anzellini *et al.*, 2013] Anzellini, S., Dewaele, A., Mezouar, M., Loubeyre, P., and Morard, G. (2013). Melting of Iron at Earth's Inner Core Boundary Based on Fast X-ray Diffraction, *Science* **340**, 464–466.

[Aryasetiawan *et al.*, 2004] Aryasetiawan, F., Imada, M., Georges, A., Kotliar, G., Biermann, S., and Lichtenstein, A. I. (2004). Frequency-dependent local interactions and low-energy effective models from electronic structure calculations, *Phys. Rev. B* **70**, 195104.

[Ashcroft and Mermin, 1976] Ashcroft, N. W. and Mermin, N. D. (1976). *Solid state physics*, chapter 13. Brooks Cole.

[Auerbach, 1994] Auerbach, A. (1994). *Interacting Electrons and Quantum Magnetism*. Springer-Verlag.

[Autieri *et al.*, 2014] Autieri, C., Koch, E., and Pavarini, E. (2014). Mechanism of structural phase transitions in $KCrF_3$, *Phys. Rev. B* **89**, 155109.

[Ayral *et al.*, 2013] Ayral, T., Biermann, S., and Werner, P. (2013). Screening and nonlocal correlations in the extended Hubbard model from self-consistent combined *GW* and dynamical mean field theory, *Phys. Rev. B* **87**, 125149.

[Ayral and Parcollet, 2015] Ayral, T. and Parcollet, O. (2015). Mott physics and spin fluctuations: A unified framework, *Phys. Rev. B* **92**, 115109.

[Bancroft *et al.*, 1956] Bancroft, D., Peterson, E. L., and Minshall, S. (1956). Polymorphism of Iron at High Pressure, *Journal of Applied Physics* **27**, 291–298.

[Becke, 1993] Becke, A. D. (1993). A new mixing of Hartree-Fock and local density-functional theories, *The Journal of Chemical Physics* **98**, 1372–1377.

[Belonoshko *et al.*, 2000] Belonoshko, A. B., Ahuja, R., and Johansson, B. (2000). Quasi–Ab Initio Molecular Dynamic Study of Fe Melting, *Phys. Rev. Lett.* **84**, 3638–3641.

[Belonoshko *et al.*, 2017] Belonoshko, A. B., Lukinov, T., Fu, J., Zhao, J., Davis, S., and Simak, S. I. (2017). Stabilization of body-centred cubic iron under inner-core conditions, *Nature Geoscience* **10**, 312–316.

[Belozerov and Anisimov, 2014] Belozerov, A. and Anisimov, V. (2014). Coulomb interaction parameters in bcc iron: an LDA+ DMFT study, *Journal of Physics: Condensed Matter* **26**, 375601.

[Berthod *et al.*, 2013] Berthod, C., Mravlje, J., Deng, X., Žitko, R., van der Marel, D., and Georges, A. (2013). Non-Drude universal scaling laws for the optical response of local Fermi liquids, *Phys. Rev. B* **87**, 115109.

[Bhadeshia and Honeycombe, 2006] Bhadeshia, H. K. D. H. and Honeycombe, R. (2006). *Steels: Microstructure and Properties*. Butterworth-Heinemann, New York.

[Bhandary *et al.*, 2016] Bhandary, S., Assmann, E., Aichhorn, M., and Held, K. (2016). Charge self-consistency in density functional theory combined with dynamical mean field theory: $k$-space reoccupation and orbital order, *Phys. Rev. B* **94**, 155131.

[Bickers, 1987] Bickers, N. E. (1987). Review of techniques in the large-$N$ expansion for dilute magnetic alloys, *Rev. Mod. Phys.* **59**, 845–939.

[Bieder and Amadon, 2014] Bieder, J. and Amadon, B. (2014). Thermodynamics of the $\alpha$-$\gamma$ transition in cerium from first principles, *Phys. Rev. B* **89**, 195132.

[Biermann *et al.*, 2003] Biermann, S., Aryasetiawan, F., and Georges, A. (2003). First-Principles Approach to the Electronic Structure of Strongly Correlated Systems: Combining the *GW* Approximation and Dynamical Mean-Field Theory, *Phys. Rev. Lett.* **90**, 086402.

[Biermann *et al.*, 2005] Biermann, S., Poteryaev, A., Lichtenstein, A. I., and Georges, A. (2005). Dynamical Singlets and Correlation-Assisted Peierls Transition in $VO_2$, *Phys. Rev. Lett.* **94**, 026404.

[Birch, 1952] Birch, F. (1952). Elasticity and constitution of the Earth's interior, *Journal of Geophysical Research* **57**, 227–286.

[Blum, 1996] Blum, K. (1996). *Density matrix theory and applications.* Plenum Press, New York.

[Boehler, 1993] Boehler, R. (1993). Temperatures in the Earth's core from melting-point measurements of iron at high static pressures, *Nature* **363**, 534–536.

[Bogaerts *et al.*, 1996] Bogaerts, R., Herlach, F., De Keyser, A., Peeters, F. M., DeRosa, F., Palmstro/m, C. J., Brehmer, D., and Allen, S. J. (1996). Experimental determination of the Fermi surface of thin $Sc_{1-x}Er_xAs$ epitaxial layers in pulsed magnetic fields, *Phys. Rev. B* **53**, 15951–15963.

[Boucherle *et al.*, 1982] Boucherle, J. X., Givord, D., and Schweizer, J. (1982). Measurements of magnetization densities in rare-earth compounds, *J. Phys. Colloques* **43**, C7–199–C7–214.

[Brooks *et al.*, 1997] Brooks, M., Eriksson, O., Wills, J., and Johansson, B. (1997). Density functional theory of crystal field quasiparticle excitations and the ab initio calculation of spin Hamiltonian parameters, *Phys. Rev. Lett.* **79**, 2546.

[Bruno, 2003] Bruno, P. (2003). Exchange Interaction Parameters and Adiabatic Spin-Wave Spectra of Ferromagnets: A " *Renormalized* Magnetic Force Theorem", *Phys. Rev. Lett.* **90**, 087205.

[Buffett, 2012] Buffett, B. (2012). Geomagnetism under scrutiny, *Nature* **485**, 319–320.

[Buffett, 2009] Buffett, B. A. (2009). Onset and orientation of convection in the inner core, *Geophysical Journal International* **179**, 711–719.

[Bulla *et al.*, 2008] Bulla, R., Costi, T. A., and Pruschke, T. (2008). Numerical renormalization group method for quantum impurity systems, *Rev. Mod. Phys.* **80**, 395–450.

[Buschow, 1991] Buschow, K. H. J. (1991). New developments in hard magnetic materials, *Reports on Progress in Physics* **54**, 1123.

[Caffarel and Krauth, 1994] Caffarel, M. and Krauth, W. (1994). Exact diagonalization approach to correlated fermions in infinite dimensions: Mott transition and superconductivity, *Phys. Rev. Lett.* **72**, 1545–1548.

[Cameron *et al.*, 2016] Cameron, A. S., Friemel, G., and Inosov, D. S. (2016). Multipolar phases and magnetically hidden order: review of the heavy-fermion compound $Ce_{1-x}La_xB_6$, *Reports on Progress in Physics* **79**, 066502.

[Campbell, 1972] Campbell, I. A. (1972). Indirect exchange for rare earths in metals, *Journal of Physics F: Metal Physics* **2**, L47.

[Capehart *et al.*, 1993] Capehart, T. W., Mishra, R. K., Meisner, G. P., Fuerst, C. D., and Herbst, J. F. (1993). Steric variation of the cerium valence in $Ce_2Fe_{14}B$ and related compounds, *Applied Physics Letters* **63**, 3642–3644.

[Carnall *et al.*, 1989] Carnall, W. T., Goodman, G. L., Rajnak, K., and Rana, R. S. (1989). A systematic analysis of the spectra of the lanthanides doped into single crystal $LaF_3$, *The Journal of Chemical Physics* **90**, 3443–3457.

[Casula *et al.*, 2012a] Casula, M., Rubtsov, A., and Biermann, S. (2012a). Dynamical screening effects in correlated materials: Plasmon satellites and spectral weight transfers from a Green's function ansatz to extended dynamical mean field theory, *Phys. Rev. B* **85**, 035115.

[Casula *et al.*, 2012b] Casula, M., Werner, P., Vaugier, L., Aryasetiawan, F., Miyake, T., Millis, A. J., and Biermann, S. (2012b). Low-Energy Models for Correlated Materials: Bandwidth Renormalization from Coulombic Screening, *Phys. Rev. Lett.* **109**, 126408.

[Chantis *et al.*, 2007] Chantis, A. N., van Schilfgaarde, M., and Kotani, T. (2007). Quasiparticle self-consistent *GW* method applied to localized $4f$ electron systems, *Phys. Rev. B* **76**, 165126.

[Chernyshev and Zhitomirsky, 2009] Chernyshev, A. L. and Zhitomirsky, M. E. (2009). Spin waves in a triangular lattice antiferromagnet: Decays, spectrum renormalization, and singularities, *Phys. Rev. B* **79**, 144416.

[Chubukov and Maslov, 2012] Chubukov, A. V. and Maslov, D. L. (2012). First-Matsubara-frequency rule in a Fermi liquid. I. Fermionic self-energy, *Phys. Rev. B* **86**, 155136.

[Cococcioni and de Gironcoli, 2005] Cococcioni, M. and de Gironcoli, S. (2005). Linear response approach to the calculation of the effective interaction parameters in the LDA+U method, *Phys. Rev. B* **71**, 035105.

[Coleman, 2002] Coleman, P. (2002). Local moment physics in heavy electron systems. In Mancini, F., editor, *Lectures on the Physics of Highly Correlated Electron Systems VI*, pages 79 – 160. American Institute of Physics, New York. arXiv:cond-mat/0206003.

[Cort *et al.*, 1982] Cort, G., Taylor, R. D., and Willis, J. O. (1982). Search for magnetism in hcp epsilon-Fe, *Journal of Applied Physics* **53**, 2064–2065.

[Czyżyk and Sawatzky, 1994] Czyżyk, M. T. and Sawatzky, G. A. (1994). Local-density functional and on-site correlations: The electronic structure of $La_2CuO_4$ and $LaCuO_3$, *Phys. Rev. B* **49**, 14211–14228.

[Daalderop *et al.*, 1992] Daalderop, G., Kelly, P., and Schuurmans, M. (1992). Magnetocrystalline anisotropy of $RECo_5$ compounds, *Journal of Magnetism and Magnetic Materials* **104-107**, 737 – 738.

[Dai *et al.*, 2005] Dai, X., Haule, K., and Kotliar, G. (2005). Strong-coupling solver for the quantum impurity model, *Phys. Rev. B* **72**, 045111.

[Damascelli *et al.*, 2003] Damascelli, A., Hussain, Z., and Shen, Z.-X. (2003). Angle-resolved photoemission studies of the cuprate superconductors, *Rev. Mod. Phys.* **75**, 473–541.

[de Koker *et al.*, 2012] de Koker, N., Steinle-Neumann, G., and Vlček, V. (2012). Electrical resistivity and thermal conductivity of liquid Fe alloys at high P and T, and heat flux in Earth's core, *Proc. Natl. Acad. Sci. U. S. A.* **109**, 4070–3.

[de' Medici *et al.*, 2011] de' Medici, L., Mravlje, J., and Georges, A. (2011). Janus-Faced Influence of Hund's Rule Coupling in Strongly Correlated Materials, *Phys. Rev. Lett.* **107**, 256401.

[Dederichs *et al.*, 1984] Dederichs, P. H., Blügel, S., Zeller, R., and Akai, H. (1984). Ground States of Constrained Systems: Application to Cerium Impurities, *Phys. Rev. Lett.* **53**, 2512–2515.

[Delange *et al.*, 2017] Delange, P., Biermann, S., Miyake, T., and Pourovskii, L. (2017). Crystal-field splittings in rare-earth-based hard magnets: An ab initio approach, *Phys. Rev. B* **96**, 155132.

[Delin *et al.*, 1998] Delin, A., Fast, L., Johansson, B., Eriksson, O., and Wills, J. M. (1998). Cohesive properties of the lanthanides: Effect of generalized gradient corrections and crystal structure, *Phys. Rev. B* **58**, 4345–4351.

[de'Medici *et al.*, 2005] de'Medici, L., Georges, A., and Biermann, S. (2005). Orbital-selective Mott transition in multiband systems: Slave-spin representation and dynamical mean-field theory, *Phys. Rev. B* **72**, 205124.

[Dewaele and Garbarino, 2017] Dewaele, A. and Garbarino, G. (2017). Low temperature equation of state of iron, *Applied Physics Letters* **111**, 021903.

[Dewaele *et al.*, 2006] Dewaele, A., Loubeyre, P., Occelli, F., Mezouar, M., Dorogokupets, P. I., and Torrent, M. (2006). Quasihydrostatic Equation of State of Iron above 2 Mbar, *Phys. Rev. Lett.* **97**, 215504.

[Doniach, 1977] Doniach, S. (1977). The Kondo lattice and weak antiferromagnetism, *Physica B+C* **91**, 231 – 234.

[Drchal *et al.*, 2005] Drchal, V., Janiš, V., Kudrnovský, J., Oudovenko, V. S., Dai, X., Haule, K., and Kotliar, G. (2005). Dynamical correlations in multiorbital Hubbard models: fluctuation exchange approximations, *Journal of Physics: Condensed Matter* **17**, 61.

[Dubrovinsky *et al.*, 2007] Dubrovinsky, L., Dubrovinskaia, N., Narygina, O., Kantor, I., Kuznetzov, A., Prakapenka, V. B., Vitos, L., Johansson, B., Mikhaylushkin, A. S., Simak, S. I., and Abrikosov, I. A. (2007). Body-Centered Cubic Iron-Nickel Alloy in Earth's Core, *Science* **316**, 1880–1883.

[Dubrovinsky *et al.*, 2011] Dubrovinsky, L., Dubrovinskaia, N., and Prakapenka, V. B. (2011). Is iron at the Earth's core conditions hcp-structured?, *Física de la Tierra* **23**, 73–82.

[Dunlap *et al.*, 1984] Dunlap, B. D., Hall, L. N., Behroozi, F., Crabtree, G. W., and Niarchos, D. G. (1984). Crystal-field effects and the magnetic properties of rare-earth rhodium borides, *Phys. Rev. B* **29**, 6244–6251.

[Dziewonski and Anderson, 1981] Dziewonski, A. M. and Anderson, D. L. (1981). Preliminary reference Earth model, *Physics of the Earth and Planetary Interiors* **25**, 297 – 356.

[Feinberg *et al.*, 1998] Feinberg, D., Germain, P., Grilli, M., and Seibold, G. (1998). Joint superexchange–Jahn-Teller mechanism for layered antiferromagnetism in $LaMnO_3$, *Phys. Rev. B* **57**, R5583–R5586.

[Feng *et al.*, 2017] Feng, Q., Ekholm, M., Tasnádi, F., Jönsson, H. J. M., and Abrikosov, I. A. (2017). Topological transitions of the Fermi surface of osmium under pressure: an LDA+DMFT study, *New Journal of Physics* **19**, 033020.

[Ferrero *et al.*, 2009] Ferrero, M., Cornaglia, P. S., De Leo, L., Parcollet, O., Kotliar, G., and Georges, A. (2009). Pseudogap opening and formation of Fermi arcs as an orbital-selective Mott transition in momentum space, *Phys. Rev. B* **80**, 064501.

[Frésard and Kotliar, 1997] Frésard, R. and Kotliar, G. (1997). Interplay of Mott transition and ferromagnetism in the orbitally degenerate Hubbard model, *Phys. Rev. B* **56**, 12909–12915.

[Fujimori *et al.*, 1992] Fujimori, A., Hase, I., Namatame, H., Fujishima, Y., Tokura, Y., Eisaki, H., Uchida, S., Takegahara, K., and de Groot, F. M. F. (1992). Evolution of the spectral function in Mott-Hubbard systems with $d^1$ configuration, *Phys. Rev. Lett.* **69**, 1796–1799.

[Fulde and Loewenhaupt, 1985] Fulde, P. and Loewenhaupt, M. (1985). Magnetic excitations in crystal-field split 4f systems, *Advances in Physics* **34**, 589–661.

[Georges, 2004] Georges, A. (2004). Strongly Correlated Electron Materials: Dynamical Mean-Field Theory and Electronic Structure, *AIP Conference Proceedings* **715**, 3–74.

[Georges *et al.*, 2013] Georges, A., de' Medici, L., and Mravlje, J. (2013). Strong Correlations from Hund's Coupling, *Annual Review of Condensed Matter Physics* **4**, 137–178.

[Georges and Kotliar, 1992] Georges, A. and Kotliar, G. (1992). Hubbard model in infinite dimensions, *Phys. Rev. B* **45**, 6479–6483.

[Georges *et al.*, 1996] Georges, A., Kotliar, G., Krauth, W., and Rozenberg, M. J. (1996). Dynamical mean-field theory of strongly correlated fermion systems and the limit of infinite dimensions, *Rev. Mod. Phys.* **68**, 13–125.

[Givord *et al.*, 1979] Givord, D., Laforest, J., Schweizer, J., and Tasset, F. (1979). Temperature dependence of the samarium magnetic form factor in SmCo5, *Journal of Applied Physics* **50**, 2008–2010.

[Glazyrin *et al.*, 2013] Glazyrin, K., Pourovskii, L. V., Dubrovinsky, L., Narygina, O., McCammon, C., Hewener, B., Schünemann, V., Wolny, J., Muffler, K., Chumakov, A. I., Crichton, W., Hanfland, M., Prakapenka, V. B., Tasnádi, F., Ekholm, M., Aichhorn, M., Vildosola, V., Ruban, A. V., Katsnelson, M. I., and Abrikosov, I. A. (2013). Importance of Correlation Effects in hcp Iron Revealed by a Pressure-Induced Electronic Topological Transition, *Phys. Rev. Lett.* **110**, 117206.

[Go and Millis, 2017] Go, A. and Millis, A. J. (2017). Adaptively truncated Hilbert space based impurity solver for dynamical mean-field theory, *Phys. Rev. B* **96**, 085139.

[Godwal *et al.*, 2015] Godwal, B. K., González-Cataldo, F., Verma, A., Stixrude, L., and Jeanloz, R. (2015). Stability of iron crystal structures at 0.3-1.5 TPa, *Earth and Planetary Science Letters* **409**, 299 – 306.

[Goll *et al.*, 2014] Goll, D., Loeffler, R., Stein, R., Pflanz, U., Goeb, S., Karimi, R., and Schneider, G. (2014). Temperature dependent magnetic properties and application potential of intermetallic $Fe_{11-x}Co_xTiCe$, *Physica Status Solidi (RRL) - Rapid Research Letters* **8**, 862–865.

[Goodenough, 1955] Goodenough, J. B. (1955). Theory of the Role of Covalence in the Perovskite-Type Manganites [La, $M$(II)]$MnO_3$, *Phys. Rev.* **100**, 564–573.

[Goremychkin *et al.*, 2018] Goremychkin, E. A., Park, H., Osborn, R., Rosenkranz, S., Castellan, J.-P., Fanelli, V. R., Christianson, A. D., Stone, M. B., Bauer, E. D., McClellan, K. J., Byler, D. D., and Lawrence, J. M. (2018). Coherent band excitations in CePd3: A comparison of neutron scattering and ab initio theory, *Science* **359**, 186–191.

[Gråsäs *et al.*, 2012] Gråsäs, O., Marco, I. D., Thunström, P., Nordström, L., Eriksson, O., Björkman, T., and Wills, J. (2012). Charge self-consistent dynamical mean-field theory based on the full-potential linear muffin-tin orbital method: Methodology and applications, *Computational Materials Science* **55**, 295 – 302.

[Grechnev *et al.*, 2007] Grechnev, A., Di Marco, I., Katsnelson, M. I., Lichtenstein, A. I., Wills, J., and Eriksson, O. (2007). Theory of bulk and surface quasiparticle spectra for Fe, Co, and Ni, *Phys. Rev. B* **76**, 035107.

[Gull, 2008] Gull, E. (2008). *Continuous-time quantum Monte Carlo algorithms for fermions.* PhD thesis, ETH Zürich, Zürich.

[Gull *et al.*, 2011] Gull, E., Millis, A. J., Lichtenstein, A. I., Rubtsov, A. N., Troyer, M., and Werner, P. (2011). Continuous-time Monte Carlo methods for quantum impurity models, *Rev. Mod. Phys.* **83**, 349–404.

[Gyorffy *et al.*, 1985] Gyorffy, B. L., Pindor, A. J., Staunton, J., Stocks, G. M., and Winter, H. (1985). A first-principles theory of ferromagnetic phase transitions in metals, *Journal of Physics F: Metal Physics* **15**, 1337.

[Hallberg, 2006] Hallberg, K. A. (2006). New trends in density matrix renormalization, *Advances in Physics* **55**, 477–526.

[Han *et al.*, 1998] Han, J. E., Jarrell, M., and Cox, D. L. (1998). Multiorbital Hubbard model in infinite dimensions: Quantum Monte Carlo calculation, *Phys. Rev. B* **58**, R4199–R4202.

[Han *et al.*, 2018] Han, Q., Birol, T., and Haule, K. (2018). Phonon Softening due to Melting of the Ferromagnetic Order in Elemental Iron, *Phys. Rev. Lett.* **120**, 187203.

[Hansmann *et al.*, 2010] Hansmann, P., Arita, R., Toschi, A., Sakai, S., Sangiovanni, G., and Held, K. (2010). Dichotomy between Large Local and Small Ordered Magnetic Moments in Iron-Based Superconductors, *Phys. Rev. Lett.* **104**, 197002.

[Hansmann *et al.*, 2013] Hansmann, P., Ayral, T., Vaugier, L., Werner, P., and Biermann, S. (2013). Long-Range Coulomb Interactions in Surface Systems: A First-Principles Description within Self-Consistently Combined *GW* and Dynamical Mean-Field Theory, *Phys. Rev. Lett.* **110**, 166401.

[Hansmann *et al.*, 2008] Hansmann, P., Severing, A., Hu, Z., Haverkort, M. W., Chang, C. F., Klein, S., Tanaka, A., Hsieh, H. H., Lin, H.-J., Chen, C. T., Fåk, B., Lejay, P., and Tjeng, L. H. (2008). Determining the Crystal-Field Ground State in Rare Earth Heavy Fermion Materials Using Soft-X-Ray Absorption Spectroscopy, *Phys. Rev. Lett.* **100**, 066405.

[Harashima *et al.*, 2015] Harashima, Y., Terakura, K., Kino, H., Ishibashi, S., and Miyake, T. (2015). Nitrogen as the best interstitial dopant among $X$ =B, C, N, O, and F for strong permanent magnet $NdFe_{11}TiX$: First-principles study, *Phys. Rev. B* **92**, 184426.

[Haule, 2015] Haule, K. (2015). Exact Double Counting in Combining the Dynamical Mean Field Theory and the Density Functional Theory, *Phys. Rev. Lett.* **115**, 196403.

[Haule and Birol, 2015] Haule, K. and Birol, T. (2015). Free Energy from Stationary Implementation of the DFT + DMFT Functional, *Phys. Rev. Lett.* **115**, 256402.

[Haule *et al.*, 2001] Haule, K., Kirchner, S., Kroha, J., and Wölfle, P. (2001). Anderson impurity model at finite Coulomb interaction U: Generalized noncrossing approximation, *Phys. Rev. B* **64**, 155111.

[Haule and Kotliar, 2009] Haule, K. and Kotliar, G. (2009). Coherence-incoherence crossover in the normal state of iron oxypnictides and importance of Hund's rule coupling, *New Journal of Physics* **11**, 025021.

[Haule and Pascut, 2016] Haule, K. and Pascut, G. L. (2016). Forces for structural optimizations in correlated materials within a DFT+embedded DMFT functional approach, *Phys. Rev. B* **94**, 195146.

[Haule *et al.*, 2010] Haule, K., Yee, C.-H., and Kim, K. (2010). Dynamical mean-field theory within the full-potential methods: Electronic structure of $CeIrIn_5$, $CeCoIn_5$, and $CeRhIn_5$, *Phys. Rev. B* **81**, 195107.

[Hausoel *et al.*, 2017] Hausoel, A., Karolak, M., Şaşıoğlu, E., Lichtenstein, A., Held, K., Katanin, A., Toschi, A., and Sangiovanni, G. (2017). Local magnetic moments in iron and nickel at ambient and Earth's core conditions, *Nature Communications* **8**, 16062.

[Haverkort *et al.*, 2012] Haverkort, M. W., Zwierzycki, M., and Andersen, O. K. (2012). Multiplet ligand-field theory using Wannier orbitals, *Phys. Rev. B* **85**, 165113.

[Held, 2007] Held, K. (2007). Electronic structure calculations using dynamical mean field theory, *Advances in Physics* **56**, 829–926.

[Held *et al.*, 2008] Held, K., Katanin, A. A., and Toschi, A. (2008). Dynamical Vertex ApproximationAn Introduction, *Progress of Theoretical Physics Supplement* **176**, 117.

[Held *et al.*, 2001a] Held, K., Keller, G., Eyert, V., Vollhardt, D., and Anisimov, V. I. (2001a). Mott-Hubbard Metal-Insulator Transition in Paramagnetic $V_2O_3$: An $LDA + DMFT$(QMC) Study, *Phys. Rev. Lett.* **86**, 5345–5348.

[Held *et al.*, 2001b] Held, K., McMahan, A. K., and Scalettar, R. T. (2001b). Cerium Volume Collapse: Results from the Merger of Dynamical Mean-Field Theory and Local Density Approximation, *Phys. Rev. Lett.* **87**, 276404.

[Herring, 1967] Herring, C. (1967). Simple Property of Electron-Electron Collisions in Transition Metals, *Phys. Rev. Lett.* **19**, 167–168.

[Hewson, 1993] Hewson, A. C. (1993). *The Kondo Problem to Heavy Fermions.* Cambridge University Press.

[Hirayama *et al.*, 2015] Hirayama, Y., Takahashi, Y., Hirosawa, S., and Hono, K. (2015). $NdFe_{12}N_x$ hard-magnetic compound with high magnetization and anisotropy field, *Scripta Materialia* **95**, 70–72.

[Hirayama *et al.*, 2017] Hirayama, Y., Takahashi, Y., Hirosawa, S., and Hono, K. (2017). Intrinsic hard magnetic properties of $Sm(Fe_{1-x}Co_x)_{12}$ compound with the $ThMn_{12}$ structure, *Scripta Materialia* **138**, 62 – 65.

[Hirose *et al.*, 2017] Hirose, K., Morard, G., Sinmyo, R., Umemoto, K., Hernlund, J., Helffrich, G., and Labrosse, S. (2017). Crystallization of silicon dioxide and compositional evolution of the Earth's core, *Nature* **543**, 99–102.

[Hirsch and Fye, 1986] Hirsch, J. E. and Fye, R. M. (1986). Monte Carlo Method for Magnetic Impurities in Metals, *Phys. Rev. Lett.* **56**, 2521–2524.

[Hirschmeier *et al.*, 2015] Hirschmeier, D., Hafermann, H., Gull, E., Lichtenstein, A. I., and Antipov, A. E. (2015). Mechanisms of finite-temperature magnetism in the three-dimensional Hubbard model, *Phys. Rev. B* **92**, 144409.

[Hohenberg and Kohn, 1964] Hohenberg, P. and Kohn, W. (1964). Inhomogeneous Electron Gas, *Phys. Rev.* **136**, B864–B871.

[Holmes *et al.*, 2004] Holmes, A. T., Jaccard, D., Behr, G., Inada, Y., and Onuki, Y. (2004). Unconventional superconductivity and non-Fermi liquid behaviour of $\varepsilon$-iron at high pressure, *Journal of Physics: Condensed Matter* **16**, S1121.

[Hölsä *et al.*, 2002] Hölsä, J., Lahtinen, M., Lastusaari, M., Valkonen, J., and Viljanen, J. (2002). Stability of Rare-Earth Oxychloride Phases: Bond Valence Study, *Journal of Solid State Chemistry* **165**, 48 – 55.

[Hölsä and Lamminmäki, 1996] Hölsä, J. and Lamminmäki, R. (1996). Analysis of the $4F^N$ energy-level structure of the $RE^{3+}$ ions in REOCl, *Journal of Luminescence* **69**, 311 – 317.

[Horvat *et al.*, 2017] Horvat, A., Pourovskii, L., Aichhorn, M., and Mravlje, J. (2017). Theoretical prediction of antiferromagnetism in layered perovskite $Sr_2TcO_4$, *Phys. Rev. B* **95**, 205115.

[Hrubiak *et al.*, 2018] Hrubiak, R., Meng, Y., and Shen, G. (2018). Experimental evidence of a body centered cubic iron at the Earth's core condition. arXiv:1804.05109.

[Hsueh *et al.*, 2002] Hsueh, H. C., Crain, J., Guo, G. Y., Chen, H. Y., Lee, C. C., Chang, K. P., and Shih, H. L. (2002). Magnetism and mechanical stability of $\alpha$-iron, *Phys. Rev. B* **66**, 052420.

[Hubbard, 1963] Hubbard, J. (1963). Electron correlations in narrow energy bands, *Proc. Roy. Soc. (London)* **A 276**, 238.

[Hummler and Fähnle, 1996] Hummler, K. and Fähnle, M. (1996). Full-potential linear-muffin-tin-orbital calculations of the magnetic properties of rare-earth–transition-metal intermetallics. I. Description of the formalism and application to the series $R\mathrm{Co}_5$ ( $R$ =rare-earth atom), *Phys. Rev. B* **53**, 3272–3289.

[Hybertsen *et al.*, 1989] Hybertsen, M. S., Schlüter, M., and Christensen, N. E. (1989). Calculation of Coulomb-interaction parameters for $\mathrm{La_2CuO_4}$ using a constrained-density-functional approach, *Phys. Rev. B* **39**, 9028–9041.

[Igoshev *et al.*, 2013] Igoshev, P. A., Efremov, A. V., Poteryaev, A. I., Katanin, A. A., and Anisimov, V. I. (2013). Magnetic fluctuations and effective magnetic moments in $\gamma$-iron due to electronic structure peculiarities, *Phys. Rev. B* **88**, 155120.

[Imada *et al.*, 1998] Imada, M., Fujimori, A., and Tokura, Y. (1998). Metal-insulator transitions, *Rev. Mod. Phys.* **70**, 1039–1263.

[Irkhin *et al.*, 1993] Irkhin, V. Y., Katsnelson, M. I., and Trefilov, A. V. (1993). On the microscopic model of Fe and Ni: the possible breakdown of the ferromagnetic fermi-liquid picture, *Journal of Physics: Condensed Matter* **5**, 8763.

[Jackeli and Khaliullin, 2009] Jackeli, G. and Khaliullin, G. (2009). Mott Insulators in the Strong Spin-Orbit Coupling Limit: From Heisenberg to a Quantum Compass and Kitaev Models, *Phys. Rev. Lett.* **102**, 017205.

[Jamieson and Lawson, 1962] Jamieson, J. C. and Lawson, A. W. (1962). X-Ray Diffraction Studies in the 100 Kilobar Pressure Range, *Journal of Applied Physics* **33**, 776–780.

[Jensen and Mackintosh, 1991] Jensen, J. and Mackintosh, A. R. (1991). *Rare Earth Magnetism: Structures and Excitations*, chapter 5.7. Clarendon Press, Oxford.

[Jia-Ning *et al.*, 2010] Jia-Ning, Z., Qing-Mei, L., Zhong, F., and Xi, D. (2010). Fast impurity solver for dynamical mean field theory based on second order perturbation around the atomic limit, *Chinese Physics B* **19**, 087104.

[Kanamori, 1959] Kanamori, J. (1959). Superexchange interaction and symmetry properties of electron orbitals, *Journal of Physics and Chemistry of Solids* **10**, 87 – 98.

[Kasuya, 1956] Kasuya, T. (1956). A Theory of Metallic Ferro- and Antiferromagnetism on Zener's Model, *Progress of Theoretical Physics* **16**, 45–57.

[Katanin *et al.*, 2010] Katanin, A. A., Poteryaev, A. I., Efremov, A. V., Shorikov, A. O., Skornyakov, S. L., Korotin, M. A., and Anisimov, V. I. (2010). Orbital-selective formation of local moments in $\alpha$-iron: First-principles route to an effective model, *Phys. Rev. B* , 045117.

[Katsnelson and Lichtenstein, 1999] Katsnelson, M. I. and Lichtenstein, A. I. (1999). LDA++ approach to the electronic structure of magnets: correlation effects in iron, *Journal of Physics: Condensed Matter* **11**, 1037.

[Katsnelson and Lichtenstein, 2000] Katsnelson, M. I. and Lichtenstein, A. I. (2000). First-principles calculations of magnetic interactions in correlated systems, *Phys. Rev. B* **61**, 8906–8912.

[Katsnelson and Trefilov, 2000] Katsnelson, M. I. and Trefilov, A. V. (2000). Fermi-liquid theory of electronic topological transitions and screening anomalies in metals, *Phys. Rev. B* **61**, 1643–1645.

[Kohn and Sham, 1965] Kohn, W. and Sham, L. J. (1965). Self-Consistent Equations Including Exchange and Correlation Effects, *Phys. Rev.* **140**, A1133–A1138.

[Kokalj, 2003] Kokalj, A. (2003). Computer graphics and graphical user interfaces as tools in simulations of matter at the atomic scale, *Computational Materials Science* **28**, 155 – 168.

[Körmann *et al.*, 2008] Körmann, F., Dick, A., Grabowski, B., Hallstedt, B., Hickel, T., and Neugebauer, J. (2008). Free energy of bcc iron: Integrated ab initio derivation of vibrational, electronic, and magnetic contributions, *Phys. Rev. B* **78**, 033102.

[Körner *et al.*, 2016] Körner, W., Krugel, G., and Elsässer, C. (2016). Theoretical screening of intermetallic $ThMn_{12}$-type phases for new hard-magnetic compounds with low rare earth content, *Scientific reports* **6**.

[Kotliar and Ruckenstein, 1986] Kotliar, G. and Ruckenstein, A. E. (1986). New Functional Integral Approach to Strongly Correlated Fermi Systems: The Gutzwiller Approximation as a Saddle Point, *Phys. Rev. Lett.* **57**, 1362–1365.

[Kotliar *et al.*, 2006] Kotliar, G., Savrasov, S. Y., Haule, K., Oudovenko, V. S., Parcollet, O., and Marianetti, C. A. (2006). Electronic structure calculations with dynamical mean-field theory, *Rev. Mod. Phys.* **78**, 865–951.

[Kubaschewski, 1982] Kubaschewski, O. (1982). *IRON - Binary Phase Diagrams*. Springer-Verlag, Berlin.

[Kugel' and Khomskii, 1982] Kugel', K. I. and Khomskii, D. I. (1982). The Jahn-Teller effect and magnetism: transition metal compounds, *Sov. Phys. Uspekhi* **25**, 231–256.

[Kuneš *et al.*, 2010] Kuneš, J., Arita, R., Wissgott, P., Toschi, A., Ikeda, H., and Held, K. (2010). Wien2wannier: From linearized augmented plane waves to maximally localized Wannier functions, *Computer Physics Communications* **181**, 1888 – 1895.

[Kvashnin *et al.*, 2015] Kvashnin, Y. O., Gråsäs, O., Di Marco, I., Katsnelson, M. I., Lichtenstein, A. I., and Eriksson, O. (2015). Exchange parameters of strongly correlated materials: Extraction from spin-polarized density functional theory plus dynamical mean-field theory, *Phys. Rev. B* **91**, 125133.

[Laforest, 1981] Laforest, J. (1981). *Magnétismes 3d et 4f dans les composés $RCo_5$: $ThCo_5$ et $SmCo_5$*. PhD thesis, USM-INP, Grenoble.

[Lang *et al.*, 1981] Lang, J. K., Baer, Y., and Cox, P. A. (1981). Study of the 4f and valence band density of states in rare-earth metals. II. Experiment and results, *Journal of Physics F: Metal Physics* **11**, 121.

[Läuchli and Werner, 2009] Läuchli, A. M. and Werner, P. (2009). Krylov implementation of the hybridization expansion impurity solver and application to 5-orbital models, *Phys. Rev. B* **80**, 235117.

[Lay *et al.*, 2008] Lay, T., Hernlund, J., and Buffett, B. (2008). Core-mantle boundary heat flow, *Nature Geoscience* **1**, 25–32.

[Lebègue *et al.*, 2005] Lebègue, S., Santi, G., Svane, A., Bengone, O., Katsnelson, M. I., Lichtenstein, A. I., and Eriksson, O. (2005). Electronic structure and spectroscopic properties of thulium monochalcogenides, *Phys. Rev. B* **72**, 245102.

[Lebègue *et al.*, 2006] Lebègue, S., Svane, A., Katsnelson, M. I., Lichtenstein, A. I., and Eriksson, O. (2006). Multiplet effects in the electronic structure of heavy rare-earth metals, *Journal of Physics: Condensed Matter* **18**, 6329.

[Lechermann *et al.*, 2007] Lechermann, F., Georges, A., Kotliar, G., and Parcollet, O. (2007). Rotationally invariant slave-boson formalism and momentum dependence of the quasiparticle weight, *Phys. Rev. B* **76**, 155102.

[Lechermann *et al.*, 2006] Lechermann, F., Georges, A., Poteryaev, A., Biermann, S., Posternak, M., Yamasaki, A., and Andersen, O. K. (2006). Dynamical mean-field theory using Wannier functions: A flexible route to electronic structure calculations of strongly correlated materials, *Phys. Rev. B* **74**, 125120.

[Leonov *et al.*, 2014a] Leonov, I., Anisimov, V. I., and Vollhardt, D. (2014a). First-Principles Calculation of Atomic Forces and Structural Distortions in Strongly Correlated Materials, *Phys. Rev. Lett.* **112**, 146401.

[Leonov *et al.*, 2015] Leonov, I., Anisimov, V. I., and Vollhardt, D. (2015). Metal-insulator transition and lattice instability of paramagnetic $V_2O_3$, *Phys. Rev. B* **91**, 195115.

[Leonov *et al.*, 2011] Leonov, I., Poteryaev, A. I., Anisimov, V. I., and Vollhardt, D. (2011). Electronic Correlations at the $\alpha$-$\gamma$ Structural Phase Transition in Paramagnetic Iron, *Phys. Rev. Lett.* **106**, 106405.

[Leonov *et al.*, 2012] Leonov, I., Poteryaev, A. I., Anisimov, V. I., and Vollhardt, D. (2012). Calculated phonon spectra of paramagnetic iron at the $\alpha$-$\gamma$ phase transition, *Phys. Rev. B* **85**, 020401.

[Leonov *et al.*, 2014b] Leonov, I., Poteryaev, A. I., Gornostyrev, Y. N., Lichtenstein, A. I., Katsnelson, M. I., Anisimov, V. I., and Vollhardt, D. (2014b). Electronic correlations determine the phase stability of iron up to the melting temperature, *Scientific Reports* **4**, 5585.

[Lichtenstein and Katsnelson, 1998] Lichtenstein, A. I. and Katsnelson, M. I. (1998). Ab initio calculations of quasiparticle band structure in correlated systems: LDA++ approach, *Phys. Rev. B* **57**, 6884–6895.

[Lichtenstein *et al.*, 2001] Lichtenstein, A. I., Katsnelson, M. I., and Kotliar, G. (2001). Finite-Temperature Magnetism of Transition Metals: An *ab initio* Dynamical Mean-Field Theory, *Phys. Rev. Lett.* **87**, 067205.

[Liechtenstein *et al.*, 1987] Liechtenstein, A., Katsnelson, M., Antropov, V., and Gubanov, V. (1987). Local spin density functional approach to the theory of exchange interactions in ferromagnetic metals and alloys, *Journal of Magnetism and Magnetic Materials* **67**, 65 – 74.

[Lin *et al.*, 2002] Lin, J.-F., Heinz, D. L., Campbell, A. J., Devine, J. M., and Shen, G. (2002). Iron-Silicon Alloy in Earth's Core?, *Science* **295**, 313.

[Locht *et al.*, 2016] Locht, I. L. M., Kvashnin, Y. O., Rodrigues, D. C. M., Pereiro, M., Bergman, A., Bergqvist, L., Lichtenstein, A. I., Katsnelson, M. I., Delin, A., Klautau, A. B., Johansson, B., Di Marco, I., and Eriksson, O. (2016). Standard model of the rare earths analyzed from the Hubbard I approximation, *Phys. Rev. B* **94**, 085137.

[Lowrie, 2007] Lowrie, W. (2007). *Fundamentals of Geophysics*. Cambridge University Press, 2 edition.

[Lu *et al.*, 2014] Lu, Y., Höppner, M., Gunnarsson, O., and Haverkort, M. W. (2014). Efficient real-frequency solver for dynamical mean-field theory, *Phys. Rev. B* **90**, 085102.

[Mackintosh and Andersen, 1980] Mackintosh, A. R. and Andersen, O. K. (1980). The electronic structure of transition metals. In Springford, M., editor, *Electrons at the Fermi Surface*, page 145. Cambridge University Press, Cambridge, England.

[Madsen and Singh, 2006] Madsen, G. K. and Singh, D. J. (2006). BoltzTraP. A code for calculating band-structure dependent quantities, *Computer Physics Communications* **175**, 67 – 71.

[Maglic, 1973] Maglic, R. (1973). Van Hove Singularity in the Iron Density of States, *Phys. Rev. Lett.* **31**, 546–548.

[Maier *et al.*, 2005] Maier, T., Jarrell, M., Pruschke, T., and Hettler, M. H. (2005). Quantum cluster theories, *Rev. Mod. Phys.* **77**, 1027–1080.

[Mao *et al.*, 1990] Mao, H. K., Wu, Y., Chen, L. C., Shu, J. F., and Jephcoat, A. P. (1990). Static compression of iron to 300 GPa and $Fe_{0.8}Ni_{0.2}$ alloy to 260 GPa: Implications for composition of the core, *Journal of Geophysical Research: Solid Earth* **95**, 21737–21742.

[Margadonna and Karotsis, 2006] Margadonna, S. and Karotsis, G. (2006). Cooperative Jahn-Teller Distortion, Phase Transitions, and Weak Ferromagnetism in the $KCrF_3$ Perovskite, *Journal of the American Chemical Society* **128**, 16436–16437.

[Margadonna and Karotsis, 2007] Margadonna, S. and Karotsis, G. (2007). High temperature orbital order melting in $KCrF_3$ perovskite, *J. Mater. Chem.* **17**, 2013–2020.

[Marzari *et al.*, 2012] Marzari, N., Mostofi, A. A., Yates, J. R., Souza, I., and Vanderbilt, D. (2012). Maximally localized Wannier functions: Theory and applications, *Rev. Mod. Phys.* **84**, 1419–1475.

[Marzari and Vanderbilt, 1997] Marzari, N. and Vanderbilt, D. (1997). Maximally localized generalized Wannier functions for composite energy bands, *Phys. Rev. B* **56**, 12847–12865.

[Matsumoto *et al.*, 2009] Matsumoto, M., Han, M. J., Otsuki, J., and Savrasov, S. Y. (2009). First-Principles Simulations of Heavy Fermion Cerium Compounds Based on the Kondo Lattice, *Phys. Rev. Lett.* **103**, 096403.

[Mazet *et al.*, 2013] Mazet, T., Malterre, D., François, M., Dallera, C., Grioni, M., and Monaco, G. (2013). Nonpareil Yb Behavior in $YbMn_6Ge_{6-x}Sn_x$, *Phys. Rev. Lett.* **111**, 096402.

[Mazin *et al.*, 2002] Mazin, I. I., Papaconstantopoulos, D. A., and Mehl, M. J. (2002). Superconductivity in compressed iron: Role of spin fluctuations, *Phys. Rev. B* **65**, 100511.

[McDonough and s. Sun, 1995] McDonough, W. and s. Sun, S. (1995). The composition of the Earth, *Chemical Geology* **120**, 223 – 253.

[McMahan *et al.*, 1998] McMahan, A., Huscroft, C., Scalettar, R., and Pollock, E. (1998). Volume-collapse transitions in the rare earth metals, *Journal of Computer-Aided Materials Design* **5**, 131–162.

[Metzner and Vollhardt, 1989] Metzner, W. and Vollhardt, D. (1989). Correlated Lattice Fermions in $d = \infty$ Dimensions, *Phys. Rev. Lett.* **62**, 324–327.

[Mikhaylushkin *et al.*, 2007] Mikhaylushkin, A. S., Simak, S. I., Dubrovinsky, L., Dubrovinskaia, N., Johansson, B., and Abrikosov, I. A. (2007). Pure Iron Compressed and Heated to Extreme Conditions, *Phys. Rev. Lett.* **99**, 165505.

[Minár *et al.*, 2005] Minár, J., Chioncel, L., Perlov, A., Ebert, H., Katsnelson, M. I., and Lichtenstein, A. I. (2005). Multiple-scattering formalism for correlated systems: A KKR-DMFT approach, *Phys. Rev. B* **72**, 045125.

[Miyake and Aryasetiawan, 2008] Miyake, T. and Aryasetiawan, F. (2008). Screened Coulomb interaction in the maximally localized Wannier basis, *Phys. Rev. B* **77**, 085122.

[Miyake *et al.*, 2009] Miyake, T., Aryasetiawan, F., and Imada, M. (2009). *Ab initio* procedure for constructing effective models of correlated materials with entangled band structure, *Phys. Rev. B* **80**, 155134.

[Miyake *et al.*, 2014] Miyake, T., Terakura, K., Harashima, Y., Kino, H., and Ishibashi, S. (2014). First-Principles Study of Magnetocrystalline Anisotropy and Magnetization in $NdFe_{12}$, $NdFe_{11}Ti$, and $NdFe_{11}TiN$, *Journal of the Physical Society of Japan* **83**, 043702.

[Monnereau *et al.*, 2010] Monnereau, M., Calvet, M., Margerin, L., and Souriau, A. (2010). Lopsided Growth of Earth's Inner Core, *Science* **328**, 1014–1017.

[Monza *et al.*, 2011] Monza, A., Meffre, A., Baudelet, F., Rueff, J.-P., d'Astuto, M., Munsch, P., Huotari, S., Lachaize, S., Chaudret, B., and Shukla, A. (2011). Iron Under Pressure: "Kohn Tweezers" and Remnant Magnetism, *Phys. Rev. Lett.* **106**, 247201.

[Mott, 1949] Mott, N. F. (1949). The Basis of the Electron Theory of Metals, with Special Reference to the Transition Metals, *Proceedings of the Physical Society. Section A* **62**, 416.

[Mravlje *et al.*, 2011] Mravlje, J., Aichhorn, M., Miyake, T., Haule, K., Kotliar, G., and Georges, A. (2011). Coherence-Incoherence Crossover and the Mass-Renormalization Puzzles in $Sr_2RuO_4$, *Phys. Rev. Lett.* **106**, 096401.

[Mydosh and Oppeneer, 2011] Mydosh, J. A. and Oppeneer, P. M. (2011). *Colloquium* : Hidden order, superconductivity, and magnetism: The unsolved case of $URu_2Si_2$, *Rev. Mod. Phys.* **83**, 1301–1322.

[Negele and Orland, 1988] Negele, J. and Orland, H. (1988). *Quantum many-particle systems*. Frontiers in physics. Addison-Wesley Pub. Co.

[Neuhaus *et al.*, 2014] Neuhaus, J., Leitner, M., Nicolaus, K., Petry, W., Hennion, B., and Hiess, A. (2014). Role of vibrational entropy in the stabilization of the high-temperature phases of iron, *Phys. Rev. B* **89**, 184302.

[Newman and Ng, 1989] Newman, D. J. and Ng, B. (1989). The superposition model of crystal fields, *Reports on Progress in Physics* **52**, 699.

[Novák, 2013] Novák, P. (2013). Calculation of crystal field parameters. In Liu, Z., editor, *Rare Earths: New Research*, pages 145–161. Nova Science Publishers, New York.

[Novák *et al.*, 2013a] Novák, P., Knížek, K., and Kuneš, J. (2013a). Crystal field parameters with Wannier functions: Application to rare-earth aluminates, *Phys. Rev. B* **87**, 205139.

[Novák *et al.*, 2014a] Novák, P., Knížek, K., and Kuneš, J. (2014a). Crystal field of rare earth impurities in LaF3, *Optical Materials* **37**, 414 – 418.

[Novák *et al.*, 2013b] Novák, P., Knížek, K., Maryško, M., Jirák, Z., and Kuneš, J. (2013b). Crystal field and magnetism of $Pr^{3+}$ and $Nd^{3+}$ ions in orthorhombic perovskites, *Journal of Physics: Condensed Matter* **25**, 446001.

[Novak and Kuriplach, 1994] Novak, P. and Kuriplach, J. (1994). Ab initio calculation of crystal field parameters in several RT5 (R=rare earth; T=Co, Ni) compounds, *IEEE Transactions on Magnetics* **30**, 1036–1038.

[Novák *et al.*, 2014b] Novák, P., Nekvasil, V., and Knížek, K. (2014b). Crystal field and magnetism with Wannier functions: Orthorhombic rare-earth manganites, *Journal of Magnetism and Magnetic Materials* **358-359**, 228 – 232.

[Novikov *et al.*, 1999] Novikov, D. L., Katsnelson, M. I., Trefilov, A. V., Freeman, A. J., Christensen, N. E., Svane, A., and Rodriguez, C. O. (1999). Anisotropy of thermal expansion and electronic topological transitions in Zn and Cd under pressure, *Phys. Rev. B* **59**, 4557–4560.

[Oguchi *et al.*, 1983] Oguchi, T., Terakura, K., and Williams, A. R. (1983). Band theory of the magnetic interaction in MnO, MnS, and NiO, *Phys. Rev. B* **28**, 6443–6452.

[Okatov *et al.*, 2009] Okatov, S. V., Kuznetsov, A. R., Gornostyrev, Y. N., Urtsev, V. N., and Katsnelson, M. I. (2009). Effect of magnetic state on the $\gamma-\alpha$ transition in iron: First-principles calculations of the Bain transformation path, *Phys. Rev. B* **79**, 094111.

[Oleś *et al.*, 2000] Oleś, A. M., Feiner, L. F., and Zaanen, J. (2000). Quantum melting of magnetic long-range order near orbital degeneracy: Classical phases and Gaussian fluctuations, *Phys. Rev. B* **61**, 6257–6287.

[Olson, 2013] Olson, P. (2013). The New Core Paradox, *Science* **342**, 431–432.

[O'Rourke and Stevenson, 2016] O'Rourke, J. G. and Stevenson, D. J. (2016). Powering Earth's dynamo with magnesium precipitation from the core, *Nature* **529**, 387–389.

[Papandrew *et al.*, 2006] Papandrew, A. B., Lucas, M. S., Stevens, R., Halevy, I., Fultz, B., Hu, M. Y., Chow, P., Cohen, R. E., and Somayazulu, M. (2006). Absence of Magnetism in Hcp Iron-Nickel at 11 K, *Phys. Rev. Lett.* **97**, 087202.

[Park *et al.*, 2014a] Park, H., Millis, A. J., and Marianetti, C. A. (2014a). Computing total energies in complex materials using charge self-consistent DFT + DMFT, *Phys. Rev. B* **90**, 235103.

[Park *et al.*, 2014b] Park, H., Millis, A. J., and Marianetti, C. A. (2014b). Total energy calculations using DFT+DMFT: Computing the pressure phase diagram of the rare earth nickelates, *Phys. Rev. B* **89**, 245133.

[Pavarini *et al.*, 2004] Pavarini, E., Biermann, S., Poteryaev, A., Lichtenstein, A. I., Georges, A., and Andersen, O. K. (2004). Mott Transition and Suppression of Orbital Fluctuations in Orthorhombic $3d^1$ Perovskites, *Phys. Rev. Lett.* **92**, 176403.

[Perdew *et al.*, 1996a] Perdew, J. P., Burke, K., and Ernzerhof, M. (1996a). Generalized Gradient Approximation Made Simple, *Phys. Rev. Lett.* **77**, 3865–3868.

[Perdew *et al.*, 1996b] Perdew, J. P., Ernzerhof, M., and Burke, K. (1996b). Rationale for mixing exact exchange with density functional approximations, *The Journal of Chemical Physics* **105**, 9982–9985.

[Perdew and Wang, 1992] Perdew, J. P. and Wang, Y. (1992). Accurate and simple analytic representation of the electron-gas correlation energy, *Phys. Rev. B* **45**, 13244–13249.

[Perdew and Zunger, 1981] Perdew, J. P. and Zunger, A. (1981). Self-interaction correction to density-functional approximations for many-electron systems, *Phys. Rev. B* **23**, 5048–5079.

[Pi *et al.*, 2014] Pi, S.-T., Nanguneri, R., and Savrasov, S. (2014). Calculation of Multipolar Exchange Interactions in Spin-Orbital Coupled Systems, *Phys. Rev. Lett.* **112**, 077203.

[Poteryaev *et al.*, 2008] Poteryaev, A. I., Ferrero, M., Georges, A., and Parcollet, O. (2008). Effect of crystal-field splitting and interband hybridization on the metal-insulator transitions of strongly correlated systems, *Phys. Rev. B* **78**, 045115.

[Potthoff *et al.*, 2003] Potthoff, M., Aichhorn, M., and Dahnken, C. (2003). Variational Cluster Approach to Correlated Electron Systems in Low Dimensions, *Phys. Rev. Lett.* **91**, 206402.

[Pourovskii, 2016] Pourovskii, L. V. (2016). Two-site fluctuations and multipolar intersite exchange interactions in strongly correlated systems, *Phys. Rev. B* **94**, 115117.

[Pourovskii *et al.*, 2007] Pourovskii, L. V., Amadon, B., Biermann, S., and Georges, A. (2007). Self-consistency over the charge density in dynamical mean-field theory: A linear muffin-tin implementation and some physical implications, *Phys. Rev. B* **76**, 235101.

[Pourovskii *et al.*, 2009] Pourovskii, L. V., Delaney, K. T., Van de Walle, C. G., Spaldin, N. A., and Georges, A. (2009). Role of Atomic Multiplets in the Electronic Structure of Rare-Earth Semiconductors and Semimetals, *Phys. Rev. Lett.* **102**, 096401.

[Pourovskii *et al.*, 2014a] Pourovskii, L. V., Hansmann, P., Ferrero, M., and Georges, A. (2014a). Theoretical Prediction and Spectroscopic Fingerprints of an Orbital Transition in $CeCu_2Si_2$, *Phys. Rev. Lett.* **112**, 106407.

[Pourovskii *et al.*, 2005] Pourovskii, L. V., Katsnelson, M. I., and Lichtenstein, A. I. (2005). Correlation effects in electronic structure of actinide monochalcogenides, *Phys. Rev. B* **72**, 115106.

[Pourovskii *et al.*, 2013] Pourovskii, L. V., Miyake, T., Simak, S. I., Ruban, A. V., Dubrovinsky, L., and Abrikosov, I. A. (2013). Electronic properties and magnetism of iron at the Earth's inner core conditions, *Phys. Rev. B* **87**, 115130.

[Pourovskii *et al.*, 2014b] Pourovskii, L. V., Mravlje, J., Ferrero, M., Parcollet, O., and Abrikosov, I. A. (2014b). Impact of electronic correlations on the equation of state and transport in $\varepsilon$-Fe, *Phys. Rev. B* **90**, 155120.

[Pourovskii *et al.*, 2017] Pourovskii, L. V., Mravlje, J., Georges, A., Simak, S. I., and Abrikosov, I. A. (2017). Electron-electron scattering and thermal conductivity of $\varepsilon$-iron at Earth's core conditions, *New Journal of Physics* **19**, 073022.

[Pozzo *et al.*, 2012] Pozzo, M., Davies, C., Gubbins, D., and Alfè, D. (2012). Thermal and electrical conductivity of iron at Earth's core conditions, *Nature* **485**, 355–358.

[Pozzo *et al.*, 2014] Pozzo, M., Davies, C., Gubbins, D., and Alfè, D. (2014). Thermal and electrical conductivity of solid iron and ironsilicon mixtures at Earth's core conditions, *Earth and Planetary Science Letters* **393**, 159 – 164.

[Prange and Korenman, 1979] Prange, R. E. and Korenman, V. (1979). Local-band theory of itinerant ferromagnetism. IV. Equivalent Heisenberg model, *Phys. Rev. B* **19**, 4691–4697.

[Prokof'ev and Svistunov, 1998] Prokof'ev, N. V. and Svistunov, B. V. (1998). Polaron Problem by Diagrammatic Quantum Monte Carlo, *Phys. Rev. Lett.* **81**, 2514–2517.

[Pruschke and Grewe, 1989] Pruschke, T. and Grewe, N. (1989). The Anderson model with finite Coulomb repulsion, *Zeitschrift für Physik B Condensed Matter* **74**, 439–449.

[Radousky *et al.*, 1983] Radousky, H. B., Dunlap, B. D., Knapp, G. S., and Niarchos, D. G. (1983). Heat-capacity studies of crystal-field effects in dilute $R\mathrm{Rh}_4\mathrm{B}_4$ compounds, *Phys. Rev. B* **27**, 5526–5529.

[Reinert and Hüfner, 2005] Reinert, F. and Hüfner, S. (2005). Photoemission spectroscopy-from early days to recent applications, *New Journal of Physics* **7**, 97.

[Richter *et al.*, 1992] Richter, M., Oppeneer, P. M., Eschrig, H., and Johansson, B. (1992). Calculated crystal-field parameters of $SmCo_5$, *Phys. Rev. B* **46**, 13919–13927.

[Richter *et al.*, 1995] Richter, M., Steinbeck, L., Nitzsche, U., Oppeneer, P. M., and Eschrig, H. (1995). On the spatial origin of crystal electric fields in $SmCo_5$, *Journal of Alloys and Compounds* **225**, 469–473.

[Rohringer *et al.*, 2018] Rohringer, G., Hafermann, H., Toschi, A., Katanin, A. A., Antipov, A. E., Katsnelson, M. I., Lichtenstein, A. I., Rubtsov, A. N., and Held, K. (2018). Diagrammatic routes to nonlocal correlations beyond dynamical mean field theory, *Rev. Mod. Phys.* **90**, 025003.

[Rohringer *et al.*, 2011] Rohringer, G., Toschi, A., Katanin, A., and Held, K. (2011). Critical Properties of the Half-Filled Hubbard Model in Three Dimensions, *Phys. Rev. Lett.* **107**, 256402.

[Romanowicz *et al.*, 1996] Romanowicz, B., Li, X.-D., and Durek, J. (1996). Anisotropy in the Inner Core: Could It Be Due To Low-Order Convection?, *Science* **274**, 963–966.

[Rotter, 2004] Rotter, M. (2004). Using McPhase to calculate magnetic phase diagrams of rare earth compounds, *Journal of Magnetism and Magnetic Materials* **272-276, Supplement**, E481 – E482.

[Ruban and Razumovskiy, 2012] Ruban, A. V. and Razumovskiy, V. I. (2012). Spin-wave method for the total energy of paramagnetic state, *Phys. Rev. B* **85**, 174407.

[Ruban *et al.*, 2004] Ruban, A. V., Shallcross, S., Simak, S. I., and Skriver, H. L. (2004). Atomic and magnetic configurational energetics by the generalized perturbation method, *Phys. Rev. B* **70**, 125115.

[Rubtsov *et al.*, 2008] Rubtsov, A. N., Katsnelson, M. I., and Lichtenstein, A. I. (2008). Dual fermion approach to nonlocal correlations in the Hubbard model, *Phys. Rev. B* **77**, 033101.

[Rubtsov *et al.*, 2005] Rubtsov, A. N., Savkin, V. V., and Lichtenstein, A. I. (2005). Continuous-time quantum Monte Carlo method for fermions, *Phys. Rev. B* **72**, 035122.

[Ruderman and Kittel, 1954] Ruderman, M. A. and Kittel, C. (1954). Indirect Exchange Coupling of Nuclear Magnetic Moments by Conduction Electrons, *Phys. Rev.* **96**, 99–102.

[Sakuma and Aryasetiawan, 2013] Sakuma, R. and Aryasetiawan, F. (2013). First-principles calculations of dynamical screened interactions for the transition metal oxides $MO$ ($M$=Mn, Fe, Co, Ni), *Phys. Rev. B* **87**, 165118.

[Sánchez-Barriga *et al.*, 2009] Sánchez-Barriga, J., Fink, J., Boni, V., Di Marco, I., Braun, J., Minár, J., Varykhalov, A., Rader, O., Bellini, V., Manghi, F., Ebert, H., Katsnelson, M. I., Lichtenstein, A. I., Eriksson, O., Eberhardt, W., and Dürr, H. A. (2009). Strength of Correlation Effects in the Electronic Structure of Iron, *Phys. Rev. Lett.* **103**, 267203.

[Sandvik, 2010] Sandvik, A. W. (2010). Computational Studies of Quantum Spin Systems, *AIP Conference Proceedings* **1297**, 135–338.

[Santini *et al.*, 2009] Santini, P., Carretta, S., Amoretti, G., Caciuffo, R., Magnani, N., and Lander, G. H. (2009). Multipolar interactions in $f$-electron systems: The paradigm of actinide dioxides, *Rev. Mod. Phys.* **81**, 807–863.

[Savrasov and Kotliar, 2004] Savrasov, S. Y. and Kotliar, G. (2004). Spectral density functionals for electronic structure calculations, *Phys. Rev. B* **69**, 245101.

[Savrasov *et al.*, 2001] Savrasov, S. Y., Kotliar, G., and Abrahams, E. (2001). Correlated electrons in $\delta$-plutonium within a dynamical mean-field picture, *Nature* **410**, 793–795.

[Sawatzky and Allen, 1984] Sawatzky, G. A. and Allen, J. W. (1984). Magnitude and Origin of the Band Gap in NiO, *Phys. Rev. Lett.* **53**, 2339–2342.

[Schäfer *et al.*, 2005] Schäfer, J., Hoinkis, M., Rotenberg, E., Blaha, P., and Claessen, R. (2005). Fermi surface and electron correlation effects of ferromagnetic iron, *Phys. Rev. B* **72**, 155115.

[Schäfer *et al.*, 2015] Schäfer, T., Geles, F., Rost, D., Rohringer, G., Arrigoni, E., Held, K., Blümer, N., Aichhorn, M., and Toschi, A. (2015). Fate of the false Mott-Hubbard transition in two dimensions, *Phys. Rev. B* **91**, 125109.

[Secchi *et al.*, 2015] Secchi, A., Lichtenstein, A., and Katsnelson, M. (2015). Magnetic interactions in strongly correlated systems: Spin and orbital contributions, *Annals of Physics* **360**, 61 – 97.

[Seth, 2016] Seth, P. (2016). private communication.

[Seth *et al.*, 2017] Seth, P., Hansmann, P., van Roekeghem, A., Vaugier, L., and Biermann, S. (2017). Towards a First-Principles Determination of Effective Coulomb Interactions in Correlated Electron Materials: Role of Intershell Interactions, *Phys. Rev. Lett.* **119**, 056401.

[Seth *et al.*, 2016] Seth, P., Krivenko, I., Ferrero, M., and Parcollet, O. (2016). TRIQS/CTHYB: A continuous-time quantum Monte Carlo hybridisation expansion solver for quantum impurity problems, *Computer Physics Communications* **200**, 274 – 284.

[Sha and Cohen, 2011] Sha, X. and Cohen, R. E. (2011). First-principles studies of electrical resistivity of iron under pressure, *Journal of Physics: Condensed Matter* **23**, 075401.

[Shick *et al.*, 2009] Shick, A. B., Kolorenč, J., Lichtenstein, A. I., and Havela, L. (2009). Electronic structure and spectral properties of Am, Cm, and Bk: Charge-density self-consistent LDA + HIA calculations in the FP-LAPW basis, *Phys. Rev. B* **80**, 085106.

[Shiina, 2004] Shiina, R. (2004). Multipolar Moments in Pr-based Filled-Skutterudite Compounds with Singlet-Triplet Crystal-Field Levels, *Journal of the Physical Society of Japan* **73**, 2257–2265.

[Shim *et al.*, 2007] Shim, J. H., Haule, K., and Kotliar, G. (2007). Modeling the Localized-to-Itinerant Electronic Transition in the Heavy Fermion System CeIrIn5, *Science* **318**, 1615–1617.

[Shimizu *et al.*, 2000] Shimizu, K., Kimura, T., Furomoto, S., Takeda, K., Kontani, K., Onuki, Y., and Amaya, K. (2000). Superconductivity in the non-magnetic state of iron under pressure, *Nature* **412**, 316–318.

[Singh *et al.*, 1991] Singh, D. J., Pickett, W. E., and Krakauer, H. (1991). Gradient-corrected density functionals: Full-potential calculations for iron, *Phys. Rev. B* **43**, 11628–11634.

[Sponza *et al.*, 2017] Sponza, L., Pisanti, P., Vishina, A., Pashov, D., Weber, C., van Schilfgaarde, M., Acharya, S., Vidal, J., and Kotliar, G. (2017). Self-energies in itinerant magnets: A focus on Fe and Ni, *Phys. Rev. B* **95**, 041112.

[Stacey and Loper, 2007] Stacey, F. and Loper, D. (2007). A revised estimate of the conductivity of iron alloy at high pressure and implications for the core energy balance, *Physics of the Earth and Planetary Interiors* **161**, 13–18.

[Steinbeck *et al.*, 1994] Steinbeck, L., Richter, M., Eschrig, H., and Nitzsche, U. (1994). Calculated crystal-field parameters for rare-earth impurities in noble metals, *Phys. Rev. B* **49**, 16289–16292.

[Steinle-Neumann *et al.*, 1999] Steinle-Neumann, G., Stixrude, L., and Cohen, R. E. (1999). First-principles elastic constants for the hcp transition metals Fe, Co, and Re at high pressure, *Phys. Rev. B* **60**, 791–799.

[Steinle-Neumann *et al.*, 2004] Steinle-Neumann, G., Stixrude, L., and Cohen, R. E. (2004). Magnetism in dense hexagonal iron, *Proceedings of the National Academy of Sciences* **101**, 33–36.

[Stevens, 1952] Stevens, K. (1952). Matrix elements and operator equivalents connected with the magnetic properties of rare earth ions, *Proceedings of the Physical Society. Section A* **65**, 209.

[Stixrude, 2012] Stixrude, L. (2012). Structure of Iron to 1 Gbar and 40 000 K, *Phys. Rev. Lett.* **108**, 055505.

[Suzuki *et al.*, 2016] Suzuki, S., Kuno, T., Urushibata, K., Kobayashi, K., Sakuma, N., Washio, K., Yano, M., Kato, A., and Manabe, A. (2016). A new magnet material with $ThMn_{12}$ structure:$(Nd_{1-x}Zr_x)(Fe_{1-y}Co_y)_{11+z}Ti_{1-z}N_\alpha$ ($\alpha$= 0.6–1.3), *Journal of Magnetism and Magnetic Materials* **401**, 259–268.

[Tateno *et al.*, 2012] Tateno, S., Hirose, K., Komabayashi, T., Ozawa, H., and Ohishi, Y. (2012). The structure of Fe-Ni alloy in Earth's inner core, *Geophysical Research Letters* **39**, L12305.

[Tateno *et al.*, 2010] Tateno, S., Hirose, K., Ohishi, Y., and Tatsumi, Y. (2010). The Structure of Iron in Earth's Inner Core, *Science* **330**, 359.

[Tie-Song *et al.*, 1991] Tie-Song, Z., Han-Min, J., Guang-Hua, G., Xiu-Feng, H., and Hong, C. (1991). Magnetic properties of R ions in R Co 5 compounds (R= Pr, Nd, Sm, Gd, Tb, Dy, Ho, and Er), *Phys. Rev. B* **43**, 8593.

[Tils *et al.*, 1999] Tils, P., Loewenhaupt, M., Buschow, K., and Eccleston, R. (1999). Crystal and exchange fields in SmCo 5 studied by inelastic neutron scattering, *Journal of alloys and compounds* **289**, 28–31.

[Tkalčić, 2015] Tkalčić, H. (2015). Complex inner core of the Earth: The last frontier of global seismology, *Reviews of Geophysics* **53**, 59–94.

[Tomczak *et al.*, 2017] Tomczak, J. M., Liu, P., Toschi, A., Kresse, G., and Held, K. (2017). Merging GW with DMFT and non-local correlations beyond, *The European Physical Journal Special Topics* **226**, 2565–2590.

[Tomczak *et al.*, 2013] Tomczak, J. M., Pourovskii, L. V., Vaugier, L., Georges, A., and Biermann, S. (2013). Rare-earth vs. heavy metal pigments and their colors from first principles, *Proceedings of the National Academy of Sciences* **110**, 904–907.

[Tsunoda, 1989] Tsunoda, Y. (1989). Spin-density wave in cubic $\gamma$-Fe and $\gamma$-$Fe_{100-x}Co_x$ precipitates in Cu, *Journal of Physics: Condensed Matter* **1**, 10427.

[Vaks and Trefilov, 1991] Vaks, V. G. and Trefilov, A. V. (1991). Anomalies of phonon spectra and anharmonic effects in metals and alloys due to proximity of the Fermi level to singular points of band structure, *Journal of Physics: Condensed Matter* **3**, 1389.

[Vekilova *et al.*, 2015] Vekilova, O. Y., Pourovskii, L. V., Abrikosov, I. A., and Simak, S. I. (2015). Electronic correlations in Fe at Earth's inner core conditions: Effects of alloying with Ni, *Phys. Rev. B* **91**, 245116.

[Vočaldo *et al.*, 2003] Vočaldo, L., Alfè, D., Gillan, M. J., Wood, I. G., Brodholt, J. P., and Price, G. D. (2003). Possible thermal and chemical stabilization of body-centred-cubic iron in the Earth's core, *Nature* **424**, 536–539.

[Wang *et al.*, 1985] Wang, C. S., Klein, B. M., and Krakauer, H. (1985). Theory of Magnetic and Structural Ordering in Iron, *Phys. Rev. Lett.* **54**, 1852–1855.

[Wang *et al.*, 1982] Wang, C. S., Prange, R. E., and Korenman, V. (1982). Magnetism in iron and nickel, *Phys. Rev. B* **25**, 5766–5777.

[Werner *et al.*, 2006] Werner, P., Comanac, A., de' Medici, L., Troyer, M., and Millis, A. J. (2006). Continuous-Time Solver for Quantum Impurity Models, *Phys. Rev. Lett.* **97**, 076405.

[Willers *et al.*, 2012] Willers, T., Strigari, F., Hiraoka, N., Cai, Y. Q., Haverkort, M. W., Tsuei, K.-D., Liao, Y. F., Seiro, S., Geibel, C., Steglich, F., Tjeng, L. H., and Severing, A. (2012). Determining the In-Plane Orientation of the Ground-State Orbital of $CeCu_2Si_2$, *Phys. Rev. Lett.* **109**, 046401.

[Wybourne and Meggers, 1965] Wybourne, B. G. and Meggers, W. F. (1965). Spectroscopic properties of rare earths.

[Xiao *et al.*, 2010] Xiao, Y., Su, Y., Li, H.-F., Kumar, C. M. N., Mittal, R., Persson, J., Senyshyn, A., Gross, K., and Brueckel, T. (2010). Neutron diffraction investigation of the crystal and magnetic structures in $KCrF_3$ perovskite, *Phys. Rev. B* **82**, 094437.

[Yadav *et al.*, 2013] Yadav, C. S., Seyfarth, G., Pedrazzini, P., Wilhelm, H., Černý, R., and Jaccard, D. (2013). Effect of pressure cycling on iron: Signatures of an electronic instability and unconventional superconductivity, *Phys. Rev. B* **88**, 054110.

[Yosida, 1957] Yosida, K. (1957). Magnetic Properties of Cu-Mn Alloys, *Phys. Rev.* **106**, 893–898.

[Zener, 1955] Zener, C. (1955). Impact of Magnetism Upon Metallurgy, *Trans. A.I.M.M.E* **203**, 619.

[Zhang *et al.*, 2011] Zhang, H., Johansson, B., and Vitos, L. (2011). Density-functional study of paramagnetic iron, *Phys. Rev. B* **84**, 140411.

[Zhang *et al.*, 2015] Zhang, P., Cohen, R., and Haule, K. (2015). Effects of electron correlations on transport properties of iron at Earth's core conditions, *Nature* **517**, 605–607.

[Zhang *et al.*, 2016] Zhang, P., Cohen, R., and Haule, K. (2016). Retraction: Effects of electron correlations on transport properties of iron at Earth's core conditions, *Nature* **536**, 112.

[Zhou *et al.*, 2014] Zhou, C., Pinkerton, F. E., and Herbst, J. F. (2014). Magnetic properties of $CeFe_{11-x}Co_xTi$ with $ThMn_{12}$ structure, *Journal of Applied Physics* **115**, 17C716.

[Zhou and Ozoliņš, 2009] Zhou, F. and Ozoliņš, V. (2009). Obtaining correct orbital ground states in $f$-electron systems using a nonspherical self-interaction-corrected LDA $+U$ method, *Phys. Rev. B* **80**, 125127.

[Zhou and Ozoliņš, 2011] Zhou, F. and Ozoliņš, V. (2011). Crystal field and magnetic structure of $UO_2$, *Phys. Rev. B* **83**, 085106.

# Glossary

**AFM** : Antiferromagnetic
**AIM** : Anderson Impurity Model
**ARPES** : Angular-Resolved Photoemission Spectroscopy
**CF** : Crystal Field
**CFP** : Crystal-Field Parameter
**cLDA** : constrained Local Density Approximation
**cRPA** : constrained Random Phase Approximation
**CT-QMC** : Continuous-Time Quantum Monte Carlo
**DC** : Double Counting
**DFT** : Density Functional Theory
**DMFT** : Dynamical Mean-Field Theory
**EIC**: Earth's Inner Core
**EF**: Exchange Field
**ETT** : Electronic Topological Transition
**FL** : Fermi Liquid
**GF** : Green's Function
**GGA** : Generalized Gradient Approximation
**GSM** : Ground-State Multiplet
**HIA** : Hubbard-I Approximation
**HubI** : Hubbard-I
**ISE** : Inter-Site Exchange
**KS** : Kohn-Sham
**LDA** : Local Density Approximation
**LSDA** : Local Spin-Density Approximation
**PDOS** : Partial Density of States
**PES** : Photoemission Spectroscopy
**QIP** : Quantum Impurity Problem
**RE** : Rare Earth
**SE** : Superexchange
**SIC** : Self-Interaction Correction
**SO** : Spin-Orbit
**TM** : Transition Metal
**TMO** : Transition-Metal Oxide
**WO** : Wannier Orbital
**XC** : Exchange and Correlation